# Limb Imaging Fourier Transform Spectrometer Experiment (LIFE)

A Thesis Submitted to the
College of Graduate and Postdoctoral Studies
in Partial Fulfillment of the Requirements
for the degree of Master of Science
in the Department of Physics and Engineering Physics
University of Saskatchewan
Saskatoon

By
Ethan E. Runge

# Permission to Use

In presenting this thesis in partial fulfilment of the requirements for a Postgraduate degree from the University of Saskatchewan, I agree that the Libraries of this University may make it freely available for inspection. I further agree that permission for copying of this thesis in any manner, in whole or in part, for scholarly purposes may be granted by the professor or professors who supervised my thesis work or, in their absence, by the Head of the Department or the Dean of the College in which my thesis work was done. It is understood that any copying or publication or use of this thesis or parts thereof for financial gain shall not be allowed without my written permission. It is also understood that due recognition shall be given to me and to the University of Saskatchewan in any scholarly use which may be made of any material in my thesis.

Requests for permission to copy or to make other use of material in this thesis in whole or part should be addressed to:

Head of the Department of Physics and Engineering Physics
163 Physics Building, 116 Science Place
University of Saskatchewan
Saskatoon, Saskatchewan S7N 5E2 Canada

OR

Dean
College of Graduate and Postdoctoral Studies
University of Saskatchewan
116 Thorvaldson Building, 110 Science Place
Saskatoon, Saskatchewan S7N 5C9 Canada

# Disclaimer

The ABB Inc, BMV Optical, and Infrared Associates products were exclusively created to meet the thesis and/or exhibition requirements for the degree of Master of Science at the University of Saskatchewan. Reference in this thesis/dissertation to any specific commercial products, process, or service by trade name, trademark, manufacturer, or otherwise, does not constitute or imply its endorsement, recommendation, or favoring by the University of Saskatchewan. The views and opinions of the author expressed herein do not state or reflect those of the University of Saskatchewan, and shall not be used for advertising or product endorsement purposes.

# Abstract

The Limb Imaging Fourier Transform Spectrometer Experiment (LIFE) project is a collaborative effort between the University of Saskatchewan, Canadian Space Agency (CSA), and ABB Canada funded through the CSA Flights and Fieldwork for the Advancement of Science and Technology (FAST) initiative. The intent of the LIFE project is to prototype a satellite instrument capable of determining the vertical distribution of water vapor, ozone, methane and nitrous oxide, which are radiatively and chemically important trace species in the Earths atmosphere. From eventual deployment into low Earth orbit, LIFE will provide high spatial and temporal resolution measurements of the upper troposphere and lower stratosphere, which will fill a key observational need for atmospheric trend and process studies. LIFE builds on the success of the Gimballed Limb Observer for Radiance Imaging in the Atmosphere (GLORIA) instrument and aims to reduce the costs involved with implementing a successful infrared imaging Fourier Transform spectrometer (IFTS).

This thesis is concerned with the design of a balloon borne prototype version of the LIFE instrument. This requires an understanding of relevant background and the development of a model capable of creating an end-to-end simulator that is used to evaluate the performance of design alternatives. As an imager, LIFE has the benefit of taking simultaneous measurements at different altitudes, avoiding temporal degradation present in other instruments. This introduces several non-idealities due to off-axis effects, which need careful consideration and analysis. Through noise equivalent spectral radiance (NESR), the performance of the instrument under the influence of noise is determined.

The design created for the first prototype of the LIFE project meets an NESR that allows the completion of scientific goals, building a foundation upon which further study and instrument refinement continues at the University of Saskatchewan. Additionally, this design has a low cost when compared to the instruments which inspired the project, creating a compelling opportunity for further development as a space mission. The proliferation of such instruments would further increase the amount of data from the observational gap, allowing a more detailed understanding of the atmosphere to be developed.

# Acknowledgements

I would like to thank the Canadian Space Agency, University of Saskatchewan, and ABB Inc for creating the LIFE project through collaboration and the FAST initiative, providing funding for such an amazing project. I am thankful for the opportunity to work as a member of the Institute of Space and Atmospheric Studies research team, and to work on the unique LIFE project.

A massive amount of gratitude goes to Jeff Langille, for all of the work and expertise imparted onto me and the LIFE project. His help was critical in my learning and the development of the instrument.

Additional thanks go to the many office mates and fellow members of ISAS, who have always been a joy to work with. For their willingness to share their expertise and insight, answer questions, and general office banter, they have been the best.

My deep gratitude goes to my supervisors, Doug Degenstein and Adam Bourassa, for the opportunity to work on this project and for introducing me to a field of study which I find stimulating. I am humbled by the amount of trust they place in my abilities and appreciative for all the help and support they have offered throughout this Master's thesis.

Finally, I would like to thank my family and friends, for their unwavering support and willingness to listen to me ramble on about LIFE.

# Contents

# List of Tables

# List of Figures

# List of Abbreviations

| | |
|---|---|
| FAST | Flights and Fieldwork for the Advancement of Science and Technology |
| CSA | Canadian Space Agency |
| FTS | Fourier Transform Spectrometer |
| IFTS | Imaging Fourier Transform Spectrometer |
| KIT | Karlsruhe Institute of Technology |
| GLORIA | Gimballed Limb Observer for Radiance Imaging in the Atmosphere |
| LIFE | Limb Imaging FTS Experiment |
| FOV | Field of View |
| UTLS | Upper troposphere/lower stratosphere |
| STE | Stratosphere-troposphere exchange |
| LOS | Line of Sight |
| EM | Electromagnetic |
| OPD | Optical Path Difference |
| ZPD | Zero Path Difference |
| MPD | Maximum Path Difference |
| ILS | Instrument Line Shape |
| DFT | Discrete Fourier Transform |
| g-r | Generation-Recombination |
| UTS | Uniform Time Sampling |
| QWIP | Quantum Well Infrared Photodetectors |
| MCT | Mercury Cadmium Telluride |
| HITRAN | High-Resolution Transmission |
| NEP | Noise Equivalent Power |
| NESR | Noise Equivalent Spectral Radiance |
| SNR | Signal-to-noise Ratio |
| BGR | Blue-Green-Red |
| RMS | Root-mean-square |

# Chapter 1

# Introduction

## 1.1 Overview

The focus for this thesis is the design of an instrument prototype that is to be launched on a balloon platform. The Limb Imaging Fourier Transform Spectrometer Experiment (LIFE) design motivation is to observe the atmosphere and obtain information about greenhouse gases in the region of the atmosphere containing the boundary between the troposphere and stratosphere. The instrument provides high spacial and temporal measurements in this region, filling a noted observational gap in the information provided by other atmospheric solutions. This design requires creation of new radiative transfer and instrument models, as thermal instrumentation is a new direction for the University of Saskatchewan Institute of Space and Atmospheric Studies (ISAS) Atmospheric Research Group. Other instruments, such as the Gimballed Limb Observer for Radiance Imaging in the Atmosphere (GLORIA), have been developed to provide insight into the processes in this observational gap. LIFE is meant to be a cost-effective solution allowing corroboration and confirmation of measurements and insights made by such instruments. These are the specific instrument motivations nested within the extended context of gaining a better understanding of the atmosphere.

The atmosphere is one of the major governors of phenomena experienced and observed on the Earth. The atmosphere is one of the factors contributing to the existence of liquid water on the planet surface and manages the water cycle and weather patterns. It also acts as a shield against radiation from external cosmic sources, such as the sun, preventing potentially harmful radiation from penetrating to the planet surface. Additionally, it acts as a "blanket" that warms the planet through the absorption and emission of thermal radiation,

maintaining a balance that ensures life continues unabated. Look at Earth's neighbours, and the importance of atmospheric balance becomes clear. Mars, with very thin atmosphere is lifeless and cold, and Venus with a thick atmosphere is extremely hot and toxic to life. Considering the atmosphere is the primary reason for the existence of life on our planet, gathering knowledge of the functions it performs and how it changes over time is extremely important. It is only with an understanding of the atmosphere that the processes driving and resulting from climate change can be analyzed and mitigated.

For many decades, scientists have been striving to create instruments that allow more knowledge of the atmosphere to be gleaned. Many of the instruments are implemented on satellites, launched into orbit around the Earth and taking measurements with detectors. These detectors view an area, considered as the scene, and collect measurements from constituents in that scene. To use detectors in this manner, signal must come from the scene constituents by either passive or active means. Passive methods depend on the scene providing all illumination, while active means apply a source of illumination to the scene and measure the response. These types of devices are known as remote sensors, as they do not directly measure the content of the atmosphere, but rather observe the effects of atmospheric composition on electromagnetic radiation. From these measurements, inferences about the state of the atmosphere are made. The process of using these measurements to determine the state of the atmosphere is known as the inverse problem [1].

Two primary viewing geometry alternatives are available for atmospheric remote sensing instruments: nadir and limb. The basic geometry of these options is depicted in figure 1.1.

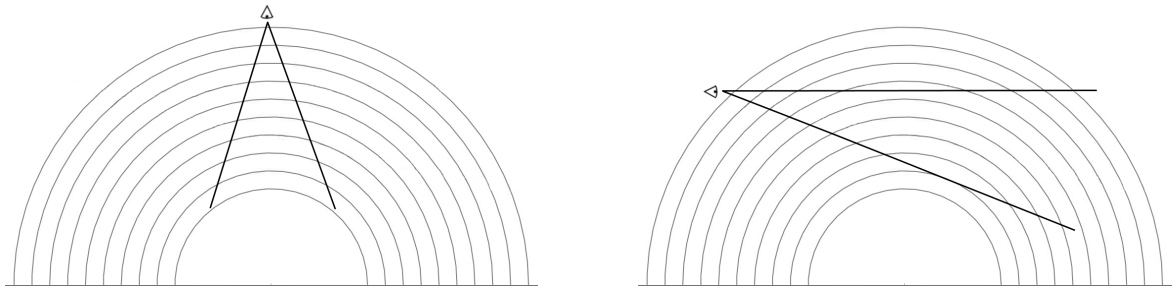

**(a)** Viewing geometry for nadir, downwards toward the earth

**(b)** Viewing geometry limb, sideways through the atmosphere into space

**Figure 1.1:** Nadir and limb viewing geometries

Each method has advantages and drawbacks, but limb sounding methods are being used more and more, as it provides increased global coverage, higher spatial resolution, and allows the determination of vertical distributions of pressure, temperature, and particle density of trace gases or aerosols, depending on the instrument used. Different instruments excel at determining different atmospheric aspects, requiring a variety of instruments to build a complete picture.

A remote sensing instrument utilizing limb sounding geometry makes use of one of two options; it either tracks the sun or other bright stellar object and makes occultated measurements or looks through the atmosphere toward empty space on the other side, viewing the radiation emitted and scattered through the atmosphere. In the case of occultation, higher signals are obtained by the instrument, but measurements can only be taken when the sun or stellar object is in the correct position in relation to the device. This results in an absorption spectrum, as the atmosphere absorbs some of the radiation from the source at wavelengths depending on the species present. This is discussed more in-depth in section 2.1.2. Aiming the instrument toward empty space means that signal received is a result of limb-scattered sunlight or direct thermal emissions. In the case of thermal emissions, no source is incident to the atmosphere, so the emissions measured are from the atmospheric constituents themselves. This generally results in lower signal levels, requiring more sensitive detectors, but can be taken at any time as there is no dependence on a source. As technology advances and more sensitive detectors are developed, the measurement frequency and coverage provided by an instrument viewing limb-scattered sunlight and thermal emissions in the limb geometry becomes more attractive.

One such remote sensing device is the Fourier Transform Spectrometer (FTS). These devices combine high throughput with high resolving power, providing increased sensitivity when compared to other spectroscopic devices like grating or Fabry Perot spectrometers [2]. The core of the FTS is a Michelson interferometer, which uses light interference to encode information regarding the source spectrum into an interferogram. The source spectrum is recovered by decoding the interferogram with a Fourier transform. In the limb viewing configuration, a set of vertically resolved measurements from the atmosphere are obtained. When combined with an inversion algorithm and forward model of the relevant physics, the

vertical distribution of atmospheric species of interest are extracted. Additionally, when operating in infrared (IR, or thermal regime), an IR-FTS obtains temperature information of the scene.

IR-FTS instruments using a single pixel detector have been produced previously, such as the Thermal and Near Infrared Sensor for Carbon Observation Fourier-Transform Spectrometer (TANSO-FTS) which measures thermal emissions, and the Atmospheric Chemistry Experiment Fourier Transform Spectrometer (ACE-FTS) which uses solar occultation techniques [3] [4]. Another instrument, most relevant to the creation of the LIFE instrument, is the forerunner to GLORIA, the thermal emission measuring Michelson Interferometer for Passive Atmospheric Sounding (MIPAS) series of instruments, which also use a single detector in their configurations [5] [6]. The intent behind the MIPAS instrument was to use thermal emission measurements to increase flexibility and coverage of observations [6]. The MIPAS instrument series includes models developed for ground-, aircraft-, and stratospheric balloon-based observations, as well as a satellite variant [5] [7]. The MIPAS instruments make use of a Silicon-Gallium (Si:Ga) detector and had stringent pointing requirements [7]. The MIPAS series of instruments have allowed the determination of the distribution of odd reactive nitrogen family as well as the distributions of temperature, $H_2O$, $O_3$, $HNO_3$, $CH_4$, $N_2O$, $ClONO_2$ and ClO [8] [9]. The satellite version of MIPAS on board ENVISAT has also provided unique insight into the evolution of the summer stratosphere in the northern hemisphere [10]. Data taken by the satellite variant have also been used to determine volcanic aerosol and chlorofluorocarbon content in the atmosphere [11] [12].

While the diverse application of data obtained by MIPAS indicates the strength of thermal limb emissions, MIPAS, TANSO-FTS and ACE-FTS are all limited by the use of a single pixel. This provides only a single viewing path through the atmosphere and leads to specialized requirements for obtaining vertical distributions. For a solitary pixel to provide information on a vertical scale, a rocking motion whereby the entire satellite tilts up and down to cover the full field of view is employed. This technique is called "limb-scanning" and results in each measurement in a vertical distribution being made from a different orbital position as the satellite moves great distances between these measurements. This limits the amount of horizontal information obtained by the instrument.

The past few decades have also seen improvements in data storage and transfer techniques, opening the way for measurement techniques that were not feasible in the past due to the large quantity of data produced. One such measurement technique, detailed in this thesis, is the imaging Fourier transform spectrometer (IFTS). The use of an FTS with imaging capabilities is a recent advancement; the ability to develop cheaper detectors with more appropriate characteristics have made it possible to investigate imaging capabilities for the FTS method. The imaging technique has the advantages of allowing a larger throughput, since the field of view is extended without sacrificing the resolving power of a sample at a single bin. Each sample is processed separately with post-processing, averaging when necessary to increase the signal-to-noise ratio of measurements. An imager also views the full vertical distribution at the same time, enhancing horizontal information and allowing a more rapid analysis of the scene than the limb-scanning methods. The result is an imager provides a higher spatial and temporal resolution than legacy FTS instruments. It has been shown by a team from the Karlsruhe Institute of Technology (KIT) that the IFTS methodology is valid and contributes unique data to the atmospheric community. With the Gimballed Limb Observer for Radiance Imaging in the Atmosphere (GLORIA) instrument, a thermal IFTS that takes images of the vertical profile of the atmosphere is introduced [13][14][15][16][17][18][19][20][21].

LIFE is a prototype satellite concept being developed in collaboration between the University of Saskatchewan, Canadian Space Agency(CSA), and ABB. The instrument takes inspiration form the success of the GLORIA imager and aims to condense the size, complexity, and cost of an FTS instrument for eventual use on a satellite platform. The project is funded through the Flights and Fieldwork for the Advancement of Science and Technology (FAST) project, a program facilitated by the CSA to promote expertise among graduate students at Canadian universities. Research projects supported by this initiative are those that involve the building or modification of instruments or technologies that are flown on sub-orbital platforms or used in simulated space environments and perform data analysis to address objectives [22]. The project is additionally funded through the MITACS Accelerate program, where the industry expertise of ABB is shared through an internship period.

This thesis details the development, design, and model creation for the first version of LIFE to be flown in 2019 upon a balloon platform.

## 1.2 GLORIA Heritage and LIFE Goals

LIFE project requirements are set by the need to obtain high spatial and temporal measurements of the UTLS region of the atmosphere. The viability and quality of data that an infrared spectral imaging device is capable of producing has been demonstrated by the GLORIA instrument. The design of the LIFE prototype builds on the success of the GLORIA project. This section details the design parameters of the GLORIA mission, and those of the LIFE prototype.

One of the primary limitations sought to be overcome with the GLORIA imaging system is the irregular sampling of the atmosphere exhibited by other limb emission sounders, such as MIPAS-STR and CRISTA-NF, resulting from the use of a single detector and scanning through the atmosphere [14]. The solution to this issue was to use a two-dimensional detector array and take images of the limb instead [14]. This type of detector also allows tomographic techniques to be used to obtain three-dimensional data when measurements are taken from an aircraft [14].

GLORIA makes use of a two-dimensional array and aims to capture an image of the atmosphere from 4 km up to the altitude of the aircraft. The detector is sensitive over the range 780 to 1400 $cm^{-1}$ and measures $H_2O$, $O_3$, $CH_4$, and $N_2O$, as well as HDO, CFC-11, CFC-12, $SF_6$, $HNO_3$, $N_2O_5$, $ClONO_2$, $HO_2NO_2$, PAN, $C_2H_6$, $H_2CO$, $NH_3$ and cirrus cloud quantities [14].

There are two modes that GLORIA can operate in: dynamics mode and chemistry mode [14]. Chemistry mode is meant to provide high spectral sampling of 0.065 $cm^{-1}$ with a trade-off of medium spatial sampling [14]. Dynamics mode offers a higher spatial sampling but has a medium spectral sampling of 0.65 $cm^{-1}$ [14]. The main difference between these two modes is the range of optical path differences covered by the interferometer. The smaller optical path difference range offered in dynamics mode takes less time to obtain an image, and thus allows GLORIA to pan through different lines of sight with respect to the flight direction and allows tomographic retrievals. Meanwhile, the higher spectral resolution of chemistry mode allows the retrieval of vertical number density for many trace species that are otherwise unable to be detected in dynamics mode but takes more time to obtain images [14].

The LIFE prototype is being designed to meet or exceed the capabilities of GLORIA operating in dynamics mode configuration. LIFE will target several of the most important trace species in the upper troposphere/lower stratosphere (UTLS) region. This includes $H_2O$ (water vapor), $N_2O$ (nitrous oxide), $O_3$ (ozone) and $CH_4$ (methane). The instrument is configured to observe thermally emitted radiation from the limb within a spectral range of 700 $cm^{-1}$ to 1400 $cm^{-1}$. This window contains strong spectral signatures for the species targeted.

The prototype is designed to fly on a balloon that has a resting altitude of 40km; LIFE views outward from that altitude down to about 8km, giving the instrument a field of view (FOV) of 5.72°.

## 1.3 Outline

This thesis details the design for the first balloon-borne prototype of the LIFE instrument. In Chapter 2, the generalized background relevant to the rest of the work is discussed. This includes information pertaining to the atmosphere and its functions, the limb viewing geometry and the ways and reasons that scientists make measurements of the atmosphere, followed by an overview of how a Michelson interferometer operates, and ends with an overview of the typical modelling process used by atmospheric scientists in using measurements to gain insights into atmospheric processes. This chapter contains the information that an individual must be familiar and comfortable with before the design process begins.

Chapter 3 takes the next step to develop the tools required to design an instrument. This includes the development of statistical models that are used to simulate the measurement process. A radiative transfer model is developed to simulate thermal emissions in a layered atmosphere and a robust instrument model is developed to simulate the impact of the instrument on the atmospheric signals. Evaluation and characterization requirements are developed, and the noise considerations are discussed. In this chapter, the application of the background information into a useable model is the focus.

This framework is applied to design the prototype LIFE instrument in Chapter 4. Practical considerations and design choices are described, using the framework of previous chapters

to make informed decisions.

An end-to-end simulation on theoretical system performance of the current design is detailed in Chapter 5. This is where important parameters like noise and acceptable error are examined and inform the final design of the LIFE instrument.

In Chapter 6, a lab version of the LIFE instrument is developed based on the design requirements of previous sections. Components are procured and the bread board version is installed in the lab. This chapter identifies the areas of further testing required to make the instrument flight ready for 2019.

# Chapter 2

# Background

## 2.1 The Atmosphere in the Thermal Regime

This section introduces and discusses the basic structure of the atmosphere. An overview of the vertical distribution of temperature and pressure levels will be briefly discussed, as will the concept of number density for trace gases. After fundamentals are discussed, the concept of thermal radiative transfer in the atmosphere is examined, along with the effects of greenhouse gases.

### 2.1.1 Overview of the Upper Troposphere/Lower Stratosphere Region

The atmosphere of the earth is divided into several layers, defined by distinct changes in temperature trends as a function of altitude. Of particular interest to this thesis is the upper troposphere lower stratosphere (UTLS) region, where the first inversion occurs. In the troposphere, the lowest layer of the atmosphere, temperature decreases with increasing altitude. Around 15 to 20 km the temperature begins increasing with altitude. This marks the second lowest layer of the atmosphere, the stratosphere. Figure 2.1 shows a diagram illustrating this behaviour, as well as the pressure profile.

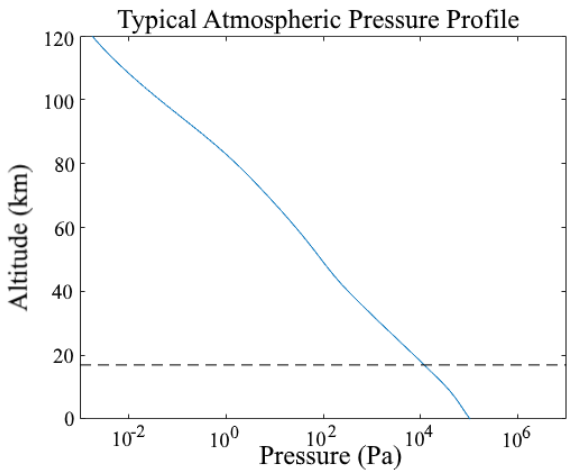


**Figure 2.1:** Typical atmospheric temperature profile using MSIS90 atmospheric state.

The dashed line in the figure is indicative of the boundary between these layers, known as the tropopause. The tropopause is dependent upon the season and geographic location, occurring as low as 10 km in the extratropic regions or 17 km in the tropics [23]. The physics governing the behaviour in these two layers is very different, with the troposphere exhibiting turbulence and the stratosphere contrasting with generally static and stable behaviour. The upper troposphere lower stratosphere (UTLS) region is broadly defined as the region 5 km above and 5 km below the tropopause where the transition between the layers occurs. In this region the layers are coupled to one another, and changes to this region can alter both stratospheric and tropospheric processes [23].

In this region, there is a bidirectional process called stratosphere-troposphere exchange (STE) which affects the chemistry of both layers [24]. In addition to STE, the local temperature minimum makes radiative transfer in this region critical to the radiative balance of the Earth. This makes the region both sensitive to and a driver of change in climate [25]. This increased radiative efficiency in this region means that changes to greenhouse gas concentrations found here have a greater impact on the greenhouse effect and the delicate balance incumbent for life on Earth. The temporal and spatial scales of chemical, dynamic, and radiative processes in the UTLS are small and vary rapidly; the current observational record of atmospheric composition developed with existing instruments do not fully resolve these processes [25]. Models must therefore make assumptions and generalizations, introduc-

ing large uncertainty. It is for this reason that the LIFE instrument is focused on obtaining accurate, high resolution measurements of this region.

Discussed in *Physics of the Atmosphere and Climate*, another major contributor to atmospheric processes in this region is the Brewer-Dobson circulation, an observed circulation between the tropics and extratropics [24]. It is characterized by upwelling of tropospheric air into the stratosphere in tropical areas, which results in downwelling in mid- and high latitudes, bringing stratospheric air into the troposphere. The source of this upwelling is generally attributed to ageostrophic circulations resulting from forces exerted by planetary waves or friction drag. Atmospheric geostrophic motion is in equilibrium, so these secondary circulations displace air parcels into different latitudes, and thus out of radiative equilibrium. The upwelling and downwelling phenomena is a reaction to this shift in equilibrium. Through this circulation, the stratosphere and troposphere are coupled to one another.

The following subsections give more detail on the interactions that occur in the stratosphere and troposphere, and the behaviours and processes of ozone ($O_3$), methane ($CH_4$), nitrous oxide ($N_2O$), and water vapor ($H_2O$) which are four of the most important greenhouse gases in the stratosphere and the targets of the LIFE instrument. The atmospheric processes governing the creation of these species are covered in the following sections, and the corresponding climate effects are covered in section 2.1.2.

The discussion in each of these subsections follows the form of information presented in *Physics of the Atmosphere and Climate* [24].

### Ozone

Considering a pure oxygen atmosphere, a relatively simple set of governing reactions allow insight into the behaviour of ozone [26]. These relations are

$$O_2 + h\nu \rightarrow O + O \qquad (J_2) \tag{2.1}$$

$$O + O_2 + M \rightarrow O_3 + M \qquad (k_2) \tag{2.2}$$

$$O + O_3 \rightarrow 2O_2 \qquad (k_3) \tag{2.3}$$

$$O_3 + h\nu \rightarrow O_2 + O \qquad (J_3) \tag{2.4}$$

where parenthetical values are rate coefficients which characterize the speed of individual reactions. The $J$ values have dimensions time$^{-1}$ and implicitly contain the wavelengths for which the reactions occur. The rate coefficient $k_2$ has dimensions $\left(\frac{\text{molecules}}{\text{volume}}\right)^{-2}$ time$^{-1}$ and $k_3$ has dimensions $\left(\frac{\text{molecules}}{\text{volume}}\right)^{-1}$ time$^{-1}$. The values of these coefficients are determined experimentally.

Equations 2.1 and 2.4 describe the photodissociation of $O_2$ and $O_3$ by UV radiation, while 2.2 and 2.3 describe the recombination $O_2$ and $O_3$ with $O$ atoms. The $M$ molecule is any air molecule, included as a third body to conserve energy and momentum in the reaction. The processes of 2.2 and 2.4 indicate that photodissociation of ozone results in atomic and molecular oxygen, which recombine to form ozone, creating a closed cycle that does not change the amount of $O_3$ or $O$ but does effectively absorb UV radiation.

The lifetime of each of the species involved in the ozone processes are related to the reaction rates. $O_2$ has a much larger lifetime than either $O$ or $O_3$, which are coupled together as the odd oxygen family:

$$O_x = O + O_3 \tag{2.5}$$

This is convenient as the fast reactions discussed previously mean that although $O_3$ and $O$ have lifetimes that differ by orders of magnitude, the lifetime of the combination $O_x$ is much longer than either of the constituents. Then, odd oxygen is considered as being in photochemical equilibrium and reaction 2.2 and 2.4 describe a redistribution of $O_x$ between the members of the family.

The destruction rate of ozone, from 2.4, is $-J_3[O_3]$ and the production rate, from 2.2 is $k_2[O_2][O][M]$, where $[X]$ is the number density of molecule $X$. Since there is photochemical equilibrium, these production and destruction rates must be equivalent, leading to:

$$J_3[O_3] = k_2[O_2][O][M] \tag{2.6}$$

The remaining reactions, 2.1 and 2.3 describe the rates at which the totality of the odd oxygen family changes as it interacts with molecular oxygen. These reactions are also governed by photochemical equilibrium, leading to a production rate of $2J_2[O_2]$ from 2.1 and a destruction rate of $-2k_3[O][O_3]$ from 2.3. This leads to an equilibrium equation:

$$J_2[O_2] = k_3[O][O_3] \tag{2.7}$$

Ozone number density is then found by using equations 2.6 and 2.7 to eliminate $[O]$ to obtain

$$[O_3] = [O_2]\left(\frac{k_2 J_2}{k_3 J_3}[M]\right)^{(1/2)} \tag{2.8}$$

This equation predicts that from the top of the atmosphere moving downwards, ozone density increases as $O_2$ increases, then reaches a peak around 30 km, and below this peak ozone number density drops sharply due to attenuation by photodissociation at the peak.

While the trend generally agrees with observations, differences in the form of overprediction of number density in tropical regions and a higher peak than observed in extratropical regions are significant. There are two primary reasons that this simple model does not match observational records. The first is the exclusion of other atmospheric species which interact with ozone. Cycles involving hydrogen, nitrogen and chlorine act as catalysts in the depletion of odd oxygen, accounting for the lower number density compared to equation 2.8. The second simplification made is ignoring the effects of atmospheric motion. Ozone lifetime is long enough below 30 km that stratospheric circulation can transport ozone through different environments, and this transport changes several important factors, discussed later in this section.

Provided in Figure 2.2 is an ozone profile derived from the MIPAS database, averaged over a month of observations in a tropical region. This profile is from real observations made by MIPAS, and is not a representation of the pure ozone discussion.

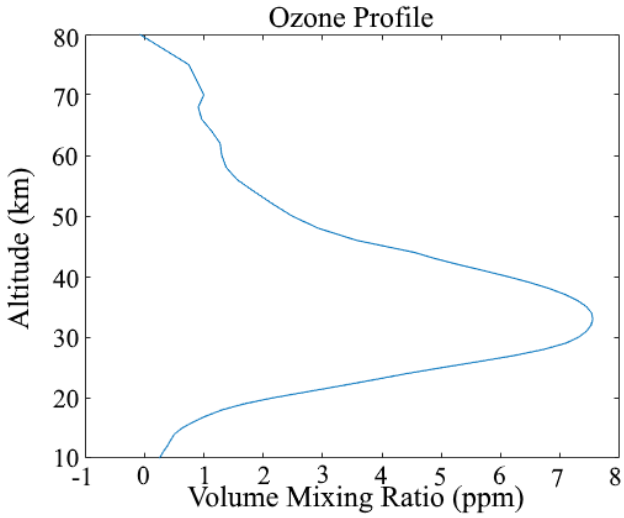


**Figure 2.2:** Typical ozone profile in a tropical region, from MIPAS observations.

### Nitrous Oxide

Nitrous oxide ($N_2O$) is created in the troposphere by natural and anthropogenic sources. It has a photochemical lifetime on the order of 100 years and is not water soluble allowing it to become well-mixed in the troposphere as it is not broken down as part of the precipitation cycle. Upwelling in tropical regions carries $N_2O$ from the troposphere into the stratosphere, where two primary reactions occur:

$$N_2O + O \rightarrow 2NO \tag{2.9}$$

$$N_2O + h\nu \rightarrow N_2 + O \tag{2.10}$$

Reaction 2.10 is the primary destruction mechanism for nitrous oxide, but 2.9 shows a method by which the free radical NO is created. Once produced, a catalytic cycle resulting in the efficient destruction of ozone occurs through

$$NO + O_3 \rightarrow NO_2 + O_2 \tag{2.11}$$

$$NO_2 + O \rightarrow NO + O_2 \tag{2.12}$$

which leaves $NO + NO_2$ unchanged and yields a net effect of $O_3 + O \rightarrow 2O_2$, allowing one molecule of $NO$ to destroy many ozone molecules.

The well-mixed nature of $N_2O$ in the troposphere makes it a valuable tracer of air motion upon entrance to the stratosphere, allowing the observation of dynamical processes [24]. When coupled with the ability to cause widespread destruction of ozone, knowledge of this species in the UTLS region is paramount to continued study.

Figure 2.3 shows a typical profile for nitrous oxide, made from a monthly average as determined from measurements made by MIPAS. This profile is made from real observational data gathered by the MIPAS instrument, provided courtesy of KIT.

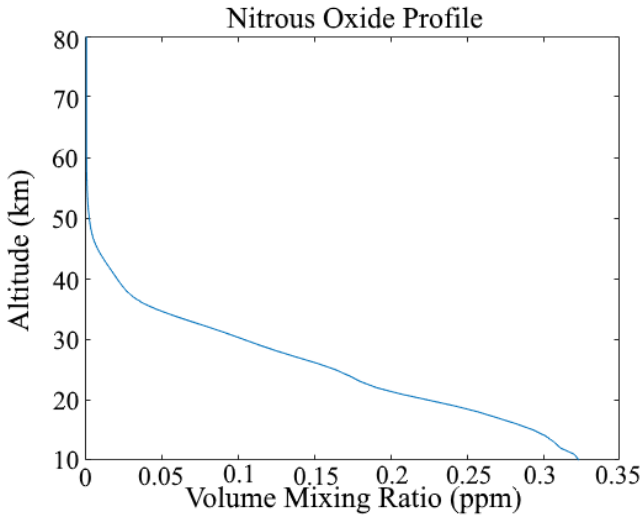


**Figure 2.3:** Typical nitrous oxide profile in a tropical region, from MIPAS observations

Additionally, $NO$ depends on several other species due to reactions with other nitrogen compounds. These reactions are fast, and so considering the odd nitrogen family is convenient,

$$NO_x = N + NO + NO_2 + NO_3 + 2N_2O_5 + HNO_3 \tag{2.13}$$

for which the members are in photochemical equilibrium with one another.

### Methane

Methane reacts with the odd oxygen and odd nitrogen families defined by 2.5 and 2.13 and thus influences ozone concentrations. Additionally, it is an important greenhouse gas that contributes to the radiative balance of the Earth. Like $N_2O$, $CH_4$ has a long photochemical

lifetime and is water insoluble, making it another well-mixed species in the troposphere. Methane also acts as an important link between the constituents of the stratosphere and water vapor.

Once introduced in the stratosphere, methane is destroyed by the hydroxyl radical ($OH$), atomic oxygen, and chlorine through the reactions

$$CH_4 + OH \rightarrow CH_3 + H_2O \tag{2.14}$$

$$CH_4 + O \rightarrow CH_3 + OH \tag{2.15}$$

$$CH_4 + Cl \rightarrow CH_3 + HCl \tag{2.16}$$

The $CH_3$ produced combines with oxygen immediately, forming $CH_3O_2$. This leads to the closed cycle

$$CH_3O_2 + NO \rightarrow CH_3O + NO_2 \tag{2.17}$$

$$NO_2 + h\nu \rightarrow NO + O \tag{2.18}$$

with net effect

$$CH_3 + h\nu \rightarrow CH_3O + O \tag{2.19}$$

Recalling that $O$ and $O_3$ balance each other as part of the $O_x$ family, reaction 2.19 provides a source of ozone in the lower stratosphere.

A typical methane profile, a monthly average from the MIPAS database, is given in Figure 2.4. This profile is made from real observational data gathered by the MIPAS instrument, provided courtesy of KIT.

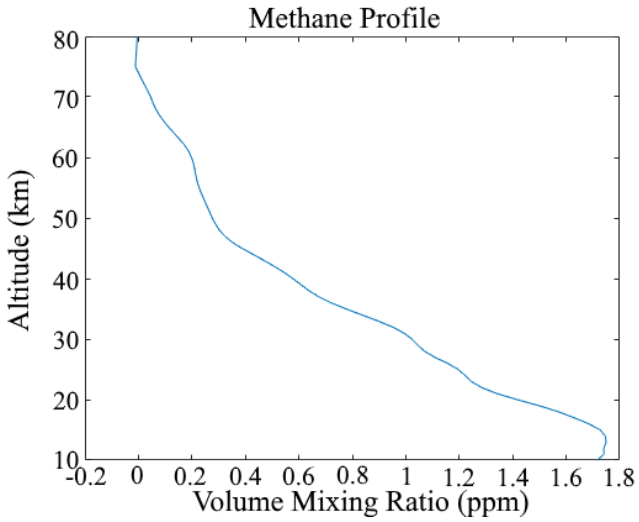


**Figure 2.4:** Typical methane profile for a tropical region, from MIPAS observations

### Water Vapor

Water vapor in the atmosphere is highly dependent upon temperature. This dependence is given in the Clausius-Clapeyron equation

$$\frac{de_s}{dT} = \frac{L_v(T)e_s}{R_v T^2} \tag{2.20}$$

with $L_v$ as the specific latent heat of evaporation, $e_s$ is the saturation water vapor pressure and $R_v$ is the water vapor gas constant. The saturation water vapor pressure is an indication of the amount of water that can be contained in an air parcel without condensation occurring. Higher temperatures result in a higher $e_s$, and so hot air has greater capacity than cold air.

It is for this reason that water vapor is primarily found in the troposphere; as altitude increases, temperature decreases and the amount of water vapor that is contained is likewise reduced. This leads to a natural barrier, known as the hygropause, occurring near the temperature inversion that characterizes the tropopause. This natural barrier prevents the majority of water vapor from entering the stratosphere.

Water vapor that enters the stratosphere dissociates via

$$H_2O + O \rightarrow 2OH \tag{2.21}$$

creating the free radical $OH$ which starts the chain of processes starting with 2.14. Water vapor has a long lifetime in the stratosphere, and acts as another tracer species.

A typical water vapor profile, using a monthly average from the MIPAS database for a tropical region, is given in Figure 2.5. This profile is made from real observational data gathered by the MIPAS instrument, provided courtesy of KIT.

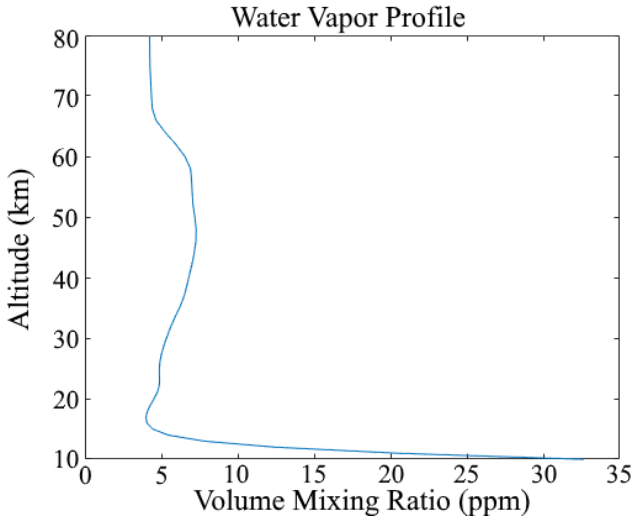


**Figure 2.5:** Typical water vapor profile for a tropical region, from MIPAS observations

### 2.1.2 Atmospheric Thermal Emission and the Greenhouse Effect

Radiative transfer in the atmosphere occurs primarily in two different regimes, which behave very differently: longwave, in the approximate wavelength range of 4 to 40 $\mu$m and shortwave, in the approximate wavelength range of 0.1 to 4 $\mu$m. Shortwave radiation is primarily generated by the sun and is efficiently scattered by atmospheric constituents. Longwave radiation however, originates mostly from the emissions of the Earth and atmosphere. Thermal radiative transfer belongs to the longwave regime, and so the focus is on the absorption and emission at these wavelengths, rather than scattering effects which are negligible at these wavelengths.

The general approach to understanding the thermal radiative processes is to consider the sun as an emitting blackbody that emits in both the solar and thermal infrared regimes, where the solar regime is ultraviolet and visible wavelength ranges and the thermal regime is infrared wavelengths. A portion of the energy released by the sun is incident upon the Earth and is absorbed or reflected by the atmosphere. The Earth is also considered as a blackbody

that emits thermal radiation, though at a much lower temperature. A portion of the energy released by the Earth is absorbed by the atmosphere as well. Figure 2.6 shows the energy budget of the Earth for both shortwave and longwave regimes.

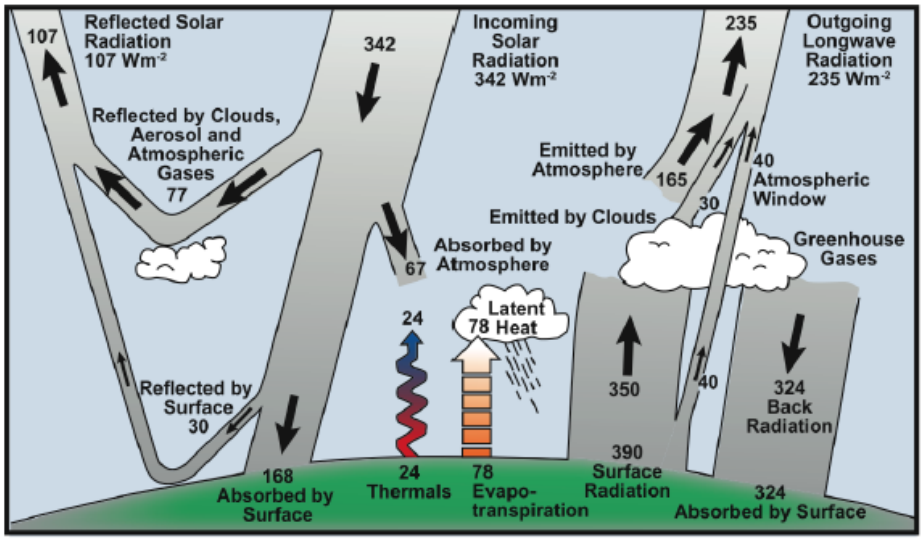


**Figure 2.6:** Earth energy budget with all major contributors [27].

First, consider the sun as a blackbody emitter at temperature $T_s$. According to the Stefan-Boltzmann law, the energy emitted per unit area is $F = \sigma T_{sun}^4$, where $\sigma$ is the Stefan-Boltzmann constant. Then consider the total power output of the sun, $P_{sun} = F * (4\pi R_s^2)$, where $R_s$ is the radius of the sun. Considering a sphere with a radius $d_E$, the distance between Earth and the sun, power per unit area at such a distance is found as shown in equation 2.22.

$$F_{d_E} = \frac{P_{sun}}{4\pi d_E^2} = \frac{(\sigma T_{sun}^4)(4\pi R_s^2)}{4\pi d_E^2} = \sigma T_{sun}^4 \frac{R_s^2}{d_E^2} \tag{2.22}$$

Knowing the power per unit area at the location of the Earth, the amount of energy captured by the surface is the Earth is determined. At this distance, the absorbing surface area behaves like a cross-section of the Earth; a circle of radius $R_E$. A portion of this radiation is also reflected by the albedo effect, represented by the variable $A$. The total energy input to the Earth is then given by equation 2.23.

$$E_{in} = \sigma T_{sun}^4 \pi R_E^2 (1 - A) \frac{R_s^2}{d_E^2} \tag{2.23}$$

In equilibrium, incoming energy must be balanced by emitted energy, so $E_{in} = E_{out}$. Assuming again that Earth acts as a perfect blackbody and emits according to the Stefan-Boltzmann equation, the temperature at the top of the Earth's atmosphere is:

$$\begin{aligned} E_{in} &= E_{out}, \\ \sigma T_{sun}^4 \pi R_E^2 (1 - A) \frac{R_s^2}{d_E^2} &= \sigma T_{Earth}^4 4\pi R_E^2, \\ T_{Earth} &= T_{sun} \left[ \frac{1}{4} \frac{R_s^2}{d_E^2} (1 - A) \right]^{\frac{1}{4}} \end{aligned} \tag{2.24}$$

Taking the temperature of the sun to be 6000 K and an Earth albedo of 0.32, equation 2.24 gives Earth a temperature of about 263 K. This is colder than the actual average temperature for Earth, which is around 288 K.

This derivation ignores the effect of the atmosphere on the temperature of the Earth. Infrared radiation is strongly absorbed by greenhouse gasses in the atmosphere, and so a more rigorous model is required to account for the atmosphere. An understanding of the radiative transfer equation in the thermal regime is necessary.

In the introduction, a brief explanation was given as to the differences between nadir and limb geometry regarding remote sensing. The goal of this remote sensing device is to determine trace gas concentrations as a function of altitude. The method most suited to this application is limb viewing geometry. An analysis of the transmission of thermal radiation through the atmosphere is indicative of this geometry being most appropriate for trace gases with substantial absorption cross sections in this spectral range.

The first step is to consider how radiation passes through a "cell" of the atmosphere. This atmospheric cell is considered as a layer of some thickness $\Delta x$, with some temperature $T$, and a gas species within the cell has some thermal emission/absorption cross-section $\sigma$ and number density $n$. A provision is also applied for incident radiation to the layer, $I_0$, with a result of output radiation $I_f$ exiting the layer. A representation of this structure is given in Figure 2.7.

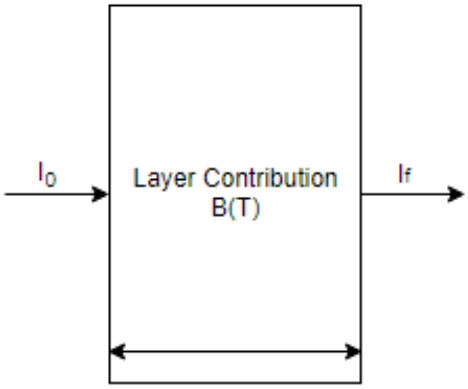


**Figure 2.7:** Diagram of radiative transfer through a single atmospheric cell.

Consider this cell as having an infinitesimal distance $ds$ instead of $\Delta x$; a change in radiation $dI$ is given by the Beer-Lambert law:

$$dI = -I\sigma n ds + B\sigma n ds \tag{2.25}$$

where B represents thermal emission according to Planck's function. From this equation, the general form for a single cell is determined:

$$\int_{I_0}^{I_f} \frac{dI}{I - B} = -\int_{x_1}^{x_2} \sigma n ds \tag{2.26}$$

$$\ln\left(\frac{I_f - B}{I_0 - B}\right) = -\sigma n(x_1 - x_2) = -\sigma n \Delta x = -\tau \tag{2.27}$$

$$I_f = I_0 e^{-\tau} + (1 - e^{-\tau})B \tag{2.28}$$

The output of the cell shown in figure 2.7 is given by equation 2.28, and the optical thickness $\tau$ is also defined in the intermediate step 2.27. The optical thickness describes how EM radiation is attenuated when incident upon a cross-section $\sigma$ with particle density $n$ and depth $\delta x$.

Equation 2.28 defines the relationship for both thermal emission and absorption; depending on the temperature of the layer, either one can occur. If the $B$ term is greater than the

input $I_0$, then $I_f$ is always larger than the input which indicates emission. Absorption occurs when $B$ is less than $I_0$, leading to an $I_f$ less than the input.

With knowledge of how this equation works for a small atmospheric cell, the effects of the atmosphere on the temperature of the Earth can also be examined. Using the definition of optical depth $\tau = \sigma n ds$ and taking the derivative of equation 2.25 with respect to optical depth leads to equation 2.29.

$$\mu \frac{dI}{d\tau} = I - B \tag{2.29}$$

In this equation, radiation is absorbed by a certain area, and re-emitted by that same area, but in a random direction. The value $\mu$ is defined as $\cos(\chi)$, where $\chi$ is the zenith angle, but is simplified such that $\mu = -1$ for radiation propagating toward Earth and $\mu = 1$ for radiation propagating toward empty space. The derivative describes how radiation incoming to the region is attenuated as a function of optical thickness, $I$ represents the outgoing radiation along a single path. $I$ is called $I^-$ when $\mu$ is negative and $I^+$ when positive. The value $B$ represents radiation that is emitted in all directions:

$$B = \sigma T^4 \tag{2.30}$$

From here, consider the integral of equation 2.29 over the solid angle of the atmosphere, $d\Omega$:

$$\begin{aligned} \int \mu \frac{dI}{d\tau} d\Omega &= \int I d\Omega - \int B d\Omega \\ 2\pi \frac{d}{d\tau} \int_{-1}^{1} \mu I d\mu &= 2\pi \int_{-1}^{1} I d\mu - 4\pi B \\ \pi \frac{d}{d\tau} \left( I^+ - I^- \right) &= 2\pi \left( I^+ + I^- \right) - 4\pi B \end{aligned} \tag{2.31}$$

If flux is defined as $f = I^+ - I^-$, and flux is the measurement of total change through the layer and does not change as a function of $\tau$ then the left side of equation 2.31 is zero, leaving

$$B = \left( \frac{I^+ + I^-}{2} \right) \tag{2.32}$$

Now consider equation 2.29 multiplied by $\mu$ and integrated over the solid angle. This gives

$$\begin{aligned}
\frac{d}{d\tau}\int \mu^2 I d\Omega &= \int \mu I d\Omega - \int \mu B d\Omega \\
\frac{d}{d\tau}\left(2\pi \int \mu^2 I d\mu\right) &= \pi(I^+ - I^-) - 0 \\
\frac{d}{d\tau}\left(\frac{4}{3}\pi\left[\frac{I^+ + I^-}{2}\right]\right) &= \pi f \\
\frac{d}{d\tau}\left(\frac{4}{3}\pi B\right) &= \pi f
\end{aligned} \tag{2.33}$$

Inserting equation 2.30 into 2.33 and integrating from 0 to an optical thickness $\tau$ leads to

$$\begin{aligned}
\int_0^\tau \frac{d}{d\tau}\frac{4}{3}\pi T^4 d\tau &= \int_0^\tau \pi f d\tau \\
\sigma T^4(\tau) &= \frac{3}{4} f\tau + \sigma T_0^4
\end{aligned} \tag{2.34}$$

where $T_0$ is the temperature at the top of the atmosphere, when $\tau = 0$. Examining this boundary at the top of the atmosphere, the $I^-$ term is equal to 0. This means the flux $f$ only has contributions from $I^+$, and this must balance with the emittance of the Earth, leading to $f = \sigma T_{Earth}^4$. Using this knowledge with equations 2.30 and 2.32 leads to

$$\sigma T_0^4 = \frac{\sigma T_{Earth}^4}{2} \tag{2.35}$$

which is used with equation 2.34 to obtain

$$T(\tau) = T_{Earth}\left(\frac{3}{4}\tau + \frac{1}{2}\right)^{1/4} \tag{2.36}$$

With some further analysis, the temperature at the ground is determined as well. The radiation incident to the ground is

$$\sigma T_g^4 = \sigma T_{Earth}^4 + I^- \tag{2.37}$$

where the optical thickness at the ground is $\tau_g$. Starting with equations 2.30 and 2.32,

$$\frac{I^+ + I^-}{2} = \sigma T^4(\tau_g),$$

and

$$I^+ - I^- = \sigma T_{Earth}^4,$$

so

$$I^- = \sigma T^4(\tau_g) - \frac{\sigma T_{Earth}^4}{2} \tag{2.38}$$

Combining equations 2.37 and 2.38 gives the equation for the temperature of the ground:

$$T_g = T_{Earth}\left(1 + \frac{3}{4}\tau_g\right) \tag{2.39}$$

Equations 2.36 and 2.39 show that the major variable in the determination of the temperatures experienced on Earth is the optical thickness. Optical thickness varies with the number density and absorption cross section of the gases that make up our atmosphere. In the thermal range of 700 $cm^{-1}$ to 1400 $cm^{-1}$, the atmosphere is considered optically thin. Much of the EM radiation emitted by the Earth falls in this thin range and is able to escape the Earth without absorption and re-emission by the atmosphere.

This is where greenhouse gases enter the discussion, as they do have weak absorption in this range. Greenhouse gases act as a kind of thermal radiation "blanket" in that increases in the concentration of these gases drastically affects the radiation balance in this normally optically thin region. This makes greenhouse gas emissions of critical interest, because increases in concentration have the potential to greatly increase the amount of thermal radiation trapped in the atmosphere, increasing the temperature of the Earth.

In the thermal regime, the target species of the LIFE instrument have a large effect, even though concentrations are small. A concept for quantitative comparisons of the strength of different natural and anthropogenic sources on climate change, known as radiative forcing (RF), provides insight into the importance of these species. Carbon dioxide is used as a baseline comparison; in 2005 the mean concentration of carbon dioxide was 379 ppm with an RF of +1.66 $W/m^2$ [28]. Comparatively, methane had a mean concentration of 1774 ppb and caused an RF of +0.48 $W/m^2$ and nitrous oxide with a mean concentration of 319 ppb caused an RF of +0.16 $W/m^2$ [28]. Note that their overall effect ranges from one third to one tenth the effect of carbon dioxide, but their concentrations are measured in parts per billion compared to carbon dioxide parts per million. Similarly, the best estimate for the effect of tropospheric ozone is an RF of +0.35 $W/m^2$ and stratospheric ozone an RF of -0.05 $W/m^2$ [28]. It was also determined through radiative transfer calculations that an increase in stratospheric water vapor of 1 ppm by volume globally causes an RF of +0.24 $W/m^2$ [29].

Small changes to the concentrations target species of the LIFE project can cause drastic change in the radiative balance of the Earth.

Each of the target species has a significant absorption/emission cross-section in the region of interest of LIFE. These cross sections are depicted in Figure 2.8, obtained from the High-Resolution Transmission (HITRAN database).

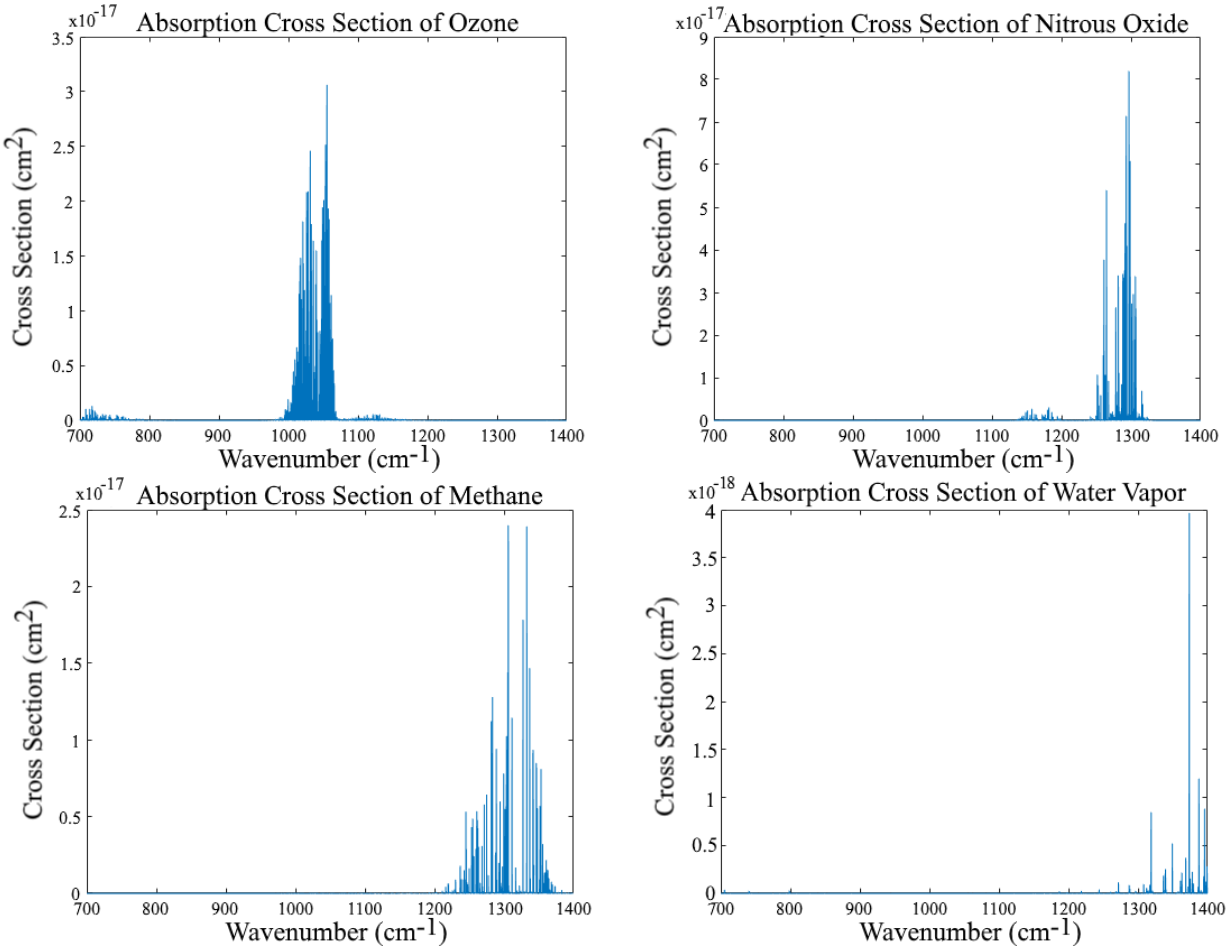


**Figure 2.8:** Absorption/emission cross sections of the target species in the wavenumber range of LIFE.

The cross sections defined are a result of combinations of vibrational, rotational, and electrical modes of particle excitation. Energy is either emitted or absorbed by particles of the given species at these wavenumbers. The focus of this thesis is on instrument design, so the HITRAN database cross-sections are used for all radiative transfer calculations instead of creating a model that simulates and calculates the cross-sections. As per equation 2.28,

these cross sections indicate the wavenumbers at which the target species strongly interact with EM radiation.

### 2.1.3 Remote Sensing in the Thermal Regime

Now that the behaviour of a single cell is characterized, a representation of the scene viewed by an instrument is developed by stacking these cells. For a nadir viewing geometry, the thermal radiation of the Earth acts as an initial source $I_0$, while deep space (considered as 0 K) or the sun act as the source for limb viewing, depending on the type of instrument. For each case, the cells are placed next to one another, with the output of each cell acting as input to the next. Figure 2.9 shows the cell structure for both geometries.

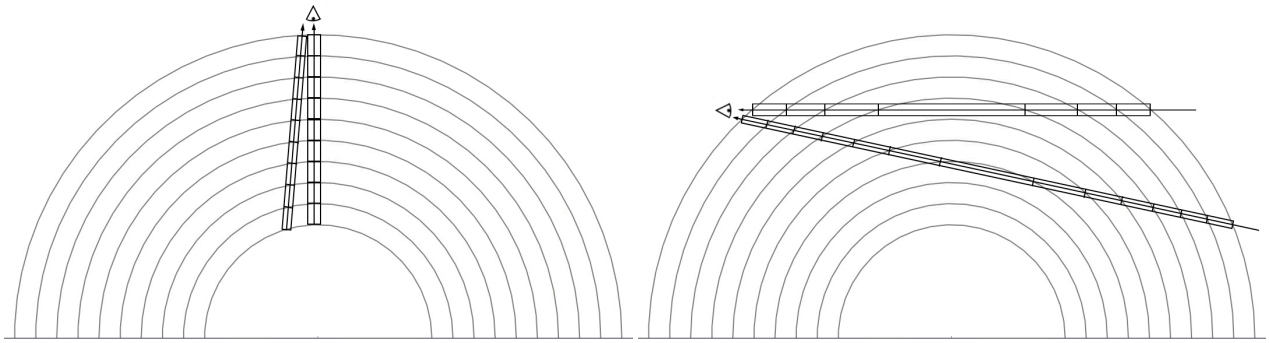

**(a)** Viewing geometry and cell structure for nadir **(b)** Viewing geometry and cell structure for limb

**Figure 2.9:** Nadir and limb viewing geometries, overlaid with the cell structures of an atmospheric model.

It follows from this figure that limb geometry has a large advantage when there is a need for vertical resolution; an instrument with a large field of view (FOV) or with the ability to change viewing direction is able to view several different lines of sight (LOS) intersecting at different altitudes, while nadir is comparatively limited in determining differences as altitude changes. In nadir viewing geometry, the total atmospheric content below an observer is the primary from of data retrieved. While useful for certain applications, trace gas measurements are primarily concerned with vertical resolution.

## 2.2 Remote Sensing with an FTS

Fourier transform spectroscopy is an old, well-understood and well-documented science [2] [30] [31]. In this section, the concepts most important and relevant to this thesis are presented. The subsections describe the basic premise of operation, details the output of an interferometer given an input scene, and how this data is obtained by an imaging detector. The formalism used here follows the framework and notation used by Davis, Abrams, and Brault [30].

### 2.2.1 Overview

Remote sensing allows the determination of atmospheric constituents by way of making indirect observations. Instead of measuring directly the amount of a certain species of gas present in a given area, remote sensors instead measure the electromagnetic (EM) radiation that is scattered or emitted by gases in that area. Each individual species has a specific spectral signature that carries information regarding the properties of the present gas, and so reading that signature allows the determination of gases present in a scene.

An FTS is a device that encodes spectral information into an interferogram. The interferograms are generated by an interferometer using the principles of EM radiation interference and the spectrum is extracted by performing an inverse Fourier transform. The mapping of interferogram samples to the spectrum hinges on a complete understanding of the instrument behaviour. In the next several sections, a theoretical understanding of the FTS is developed.

### 2.2.2 Michelson Interferometer

Michelson interferometers are common and simple interferometers utilized in a wide variety of fields. For LIFE, the Michelson interferometer is utilized as a Fourier transform spectrometer. The general configuration of the device is either a four-port instrument consisting of two inputs and two outputs, or a two-port instrument with one input and one output. Variants of the device can also include the use of flat mirrors or corner cubes. The core of LIFE is a modified two-port Michelson interferometer utilizing corner cubes. Figure 2.10

illustrates such an interferometer. The Michelson interferometer used in LIFE, provided by ABB Canada, makes slight modification to the mirror movement detailed in this section. These modifications, discussed in section 4.3.2, do not affect the theory or concepts of using an interferometer for spectroscopy discussed in this section.

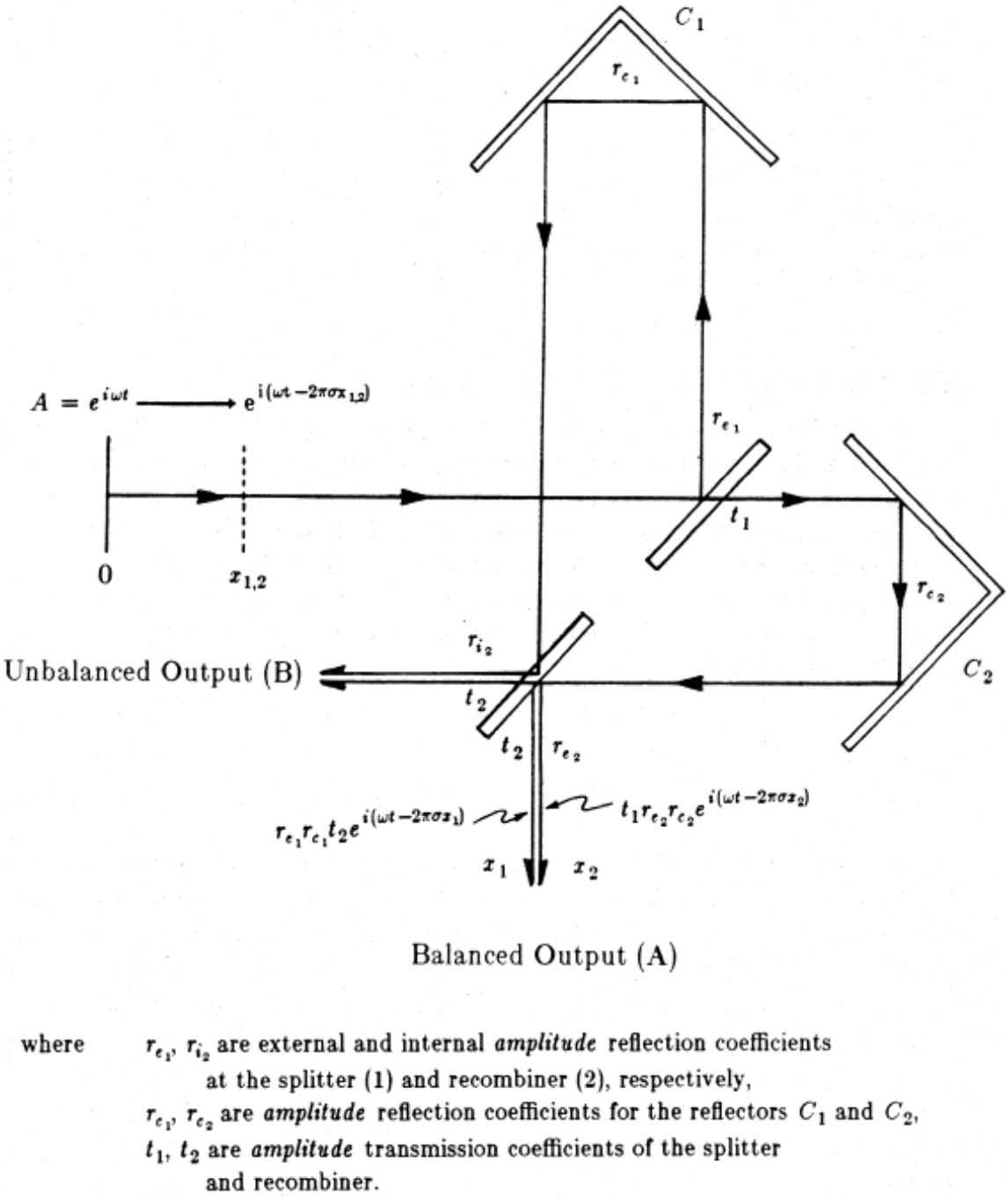


**Figure 2.10:** A two port Michelson interferometer utilizing corner cubes [30].

### 2.2.3 The Ideal Case

An ideal Michelson interferometer, an example of which is shown in Figure 2.10, consists of three major components: a beamsplitter, a fixed mirror, and a moving mirror. Collimated light from a source enters the interferometer through the input port and is then divided by a beamsplitter into two beams. In the case of an ideal beamsplitter with 50% transmittance and 50% reflectance, the two beams have equal amplitude. Each beam travels down an arm of the interferometer where it encounters a mirror. In the case of a simple interferometer, the mirror in one arm moves while the mirror in the other is stationary. The mirrors are positioned to reflect the beams back to the beamsplitter, where they are again transmitted and reflected 50/50. When a lens system is placed at the interferometer output to focus the exiting radiation, the result is that a portion of the beam from one path is recombined with a portion of the beam from the other path. The interferometer works by changing the position of one mirror relative to the other, creating differences in the path length travelled by the two beams. The difference in these paths, denoted by $x$, is defined as the optical path difference (OPD). When each mirror is an equal distance from the beamsplitter, this defines the zero path difference (ZPD).

A detector is placed at the focal plane of the lens system in order to detect and measure the radiation. As the relative mirror position changes, the detector sees a change in the intensity of the signal, as the two beams are interfering with one another. At ZPD, each beam travels the same distance, and thus their signals interfere constructively, increasing the signal incident on the detector. Given a source with wavelength $\lambda$, displacing the moving mirror by $\lambda/4$ creates a path difference of $\lambda/2$. The result is that the two beams are now out of phase with each other, and interfere destructively, and no signal is seen by the detector. Displacing the mirror another $\lambda/4$ creates an OPD of $\lambda$ and so constructive interference occurs again. The displacement of the moving mirror continues, interfering constructively and creating maximum signal when OPD $= n\lambda$, where $n = 0, 1, 2, ....$ Similarly, when OPD $= (n+\frac{1}{2})\lambda$, destructive interference occurs and creates a minimum signal. This variation in signal intensity as a function of OPD is what generates an interferogram.

The equation representing this signal intensity changes based on the source. Considering

a monochromatic source with a wavelength $\lambda_0$ (corresponding to wavenumber $\sigma_0 = 1/\lambda_0$) and radiance $S(\sigma_0)$,

$$I_0(x) = S(\sigma_0)\left[1 + \cos(2\pi\sigma_0 x)\right] \tag{2.40}$$

gives the intensity of the interferogram signal as a function of OPD. Notice that the interferogram contains a modulated and unmodulated term; the modulated term contains the data related to the interference pattern. The modulated portion is extracted by subtracting the mean value from the interferogram.

Polychromatic sources are detected as a superposition of many monochromatic sources,

$$I_p(x) = \int_0^\infty S(\sigma)(1 + \cos(2\pi\sigma x))d\sigma \tag{2.41}$$

It is important to note here that the data obtained by the detector is $I_p(x)$. To obtain the modulated data, the mean value is subtracted,

$$I(x) = I_p(x) - \overline{I_p(x)} \tag{2.42}$$

$$= \int_0^\infty S(\sigma)(\cos(2\pi\sigma x))d\sigma \tag{2.43}$$

Equation 2.42 presents the form of the data that is truly worked with, while equation 2.43 presents the theoretical equation which that data represents.

The maximum signal of the interferogram occurs at the optical ZPD, as all wavelengths of light interfere constructively at this point. As the mirror moves away from ZPD, rays become more out-of-phase. Away from the ZPD only a small fraction of the rays interfere constructively, and most interfere destructively, resulting in a drastic drop in signal levels.

The modulated portion of the interferogram given in 2.42 and 2.43 contains all the spectral information; the distribution that created the interferogram is recovered with an inverse Fourier transformation,

$$S(\sigma) = \int_0^\infty I(x)\cos(2\pi\sigma x)dx \tag{2.44}$$

If we consider the signal extending from $-\infty$ to $\infty$, there is also a spectrum $S(-\sigma)$. At these negative wavenumbers, the spectrum is a mirror of the values at the corresponding positive wavenumber. This means that in terms of a complex Fourier transform, equations

2.43 and 2.44 become

$$I(x) = \int_{-\infty}^{\infty} S(\sigma) e^{i2\pi\sigma x} d\sigma \tag{2.45}$$

and

$$S(\sigma) = \int_{-\infty}^{\infty} I(x) e^{-i2\pi\sigma x} dx \tag{2.46}$$

illustrating the fundamental principle of an FTS; a measured interferogram is the Fourier transformation of the spectrum that is used in its generation.

### 2.2.4 Practical Considerations

A measured interferogram has several non-idealities associated with it that change the relationship shown in 2.45 and 2.46 that must be considered, corrected, and/or mitigated in practice. These instrument effects are discussed in the next several subsections.

#### Asymmetrical Interferograms

The interferogram measured by the instrument is real, but if it is not perfectly symmetrical the complex transform will create a complex function.

$$S(\sigma) = S_r(\sigma) + iS_i(\sigma) = |S(\sigma)| e^{i\phi(\sigma)} \tag{2.47}$$

where $S_r(\sigma)$ is the real and $iS_i(\sigma)$ the imaginary part of the spectrum, and $|S(\sigma)|$ is amplitude with a phase of $\phi(\sigma)$. Amplitude and phase are given, respectively, by

$$|S(\sigma)| = \sqrt{(S_r(\sigma))^2 + (S_i(\sigma))^2} \tag{2.48}$$

$$\phi(\sigma) = \tan^{-1}\left[\frac{S_i(\sigma)}{S_r(\sigma)}\right] \tag{2.49}$$

Effort is made to obtain symmetrical interferograms to simplify data analysis and calibration. In practice, techniques have been developed to perform a phase correction and retrieve the real spectrum. The calibration technique utilized by LIFE is specifically developed for IR-FTS measurements. This technique is discussed in section 3.1.3.

### Instrument Line Shape

In practice, the interferogram measured by the instrument is limited to a finite range determined by the amount of movement possible in the mirror arrangement. The maximum distance obtainable in an FTS system is the Maximum optical Path Difference (MPD), denoted with the value $L$. Thus, a true interferogram does not extend to $\pm\infty$ but is instead truncated to the range $[-L,L]$. This truncation can also be thought of as multiplying the interferogram by a rectangular window.

The truncation of the interferogram has adverse effects on the recovered spectrum. Convolution theory states that a multiplication in one domain is equivalent to taking a Fourier transform after convolution in the Fourier transform domain.

$$f(x) \cdot g(x) = FT(F(\sigma)) \cdot FT(G(\sigma)) = FT(F(\sigma) \otimes (G(\sigma)) \tag{2.50}$$

Thus, if multiplying two functions together in one domain, then they are convolved in the Fourier transform domain. Multiplying by a rectangular function window in interferogram space is therefore equivalent to a convolution of the spectrum with the Fourier transform of the rectangular window, which is a sinc function, in spectral space.

Therefore, the finite interferogram given by

$$I_{finite}(x) = I_{finite}(x) \cdot \Pi\left(\frac{x}{2L}\right) \tag{2.51}$$

where $\Pi(x)$ represents a rectangle function with argument $x$ results in a spectrum:

$$S_{finite}(\sigma) = S_{infinite}(\sigma) \otimes 2L\text{sinc}(2L\sigma) \tag{2.52}$$

This is important to note, as it shows that the act of shortening the length of the interferogram broadens the spectral lines. This effect decreases the spectral resolution of the device. Consider a monochromatic source, which behaves like a Dirac delta function in spectral space. Convolution of a Dirac delta with a sinc function results in a line shape of a sinc function. Thus, a previously infinitesimal width becomes finite and measurable after convolution. This is known as the instrument line shape (ILS) or instrument function and must be considered when analyzing data.

$$ILS(\sigma) = 2L\text{sinc}(2L\sigma) \tag{2.53}$$

Equation 2.53 determines how an input line is broadened by the ILS. Note that a larger $L$ argument in the sinc function makes the center peak narrower, and so interferograms with larger MPD's show less broadening effects.

### Apodization Effects

Due to the sinc function ILS, each spectral line not only broadens with the sinc function center lobe, but creates smaller side-lobes as well, in an effect called ringing. With spectral lines that are sharper than the ILS, these sidelobes have visible effects on the spectrum. An example of this is if a strong spectral line lay next to a weak spectral line; the side-lobes of the strong line have the potential to completely envelop the weak line, effectively destroying the ability to resolve it reliably. The major source of ringing occurs due to discontinuity caused by truncating the infinite interferogram to the $[-L, L]$ range.

This non-ideal effect is mitigated by a process called apodization, where the interferogram is multiplied by a function that reduces the amplitude slowly to zero by the end of the interferogram range. While this removes the effects of side-lobes, it also broadens the spectral lines. Care needs to be taken to ensure that a proper trade-off between side-lobe suppression and line-broadening effects is obtained.

### Discrete Sampling

The scene viewed by the detector as the mirror moves is continuous, but the images taken are not. By nature, detected data is discrete and thus we have a continuous signal that has discrete sample points. The obtained data is expressed as a multiplication of the continuous signal from 2.42 with a Dirac comb with a spacing $\Delta x$.

$$I_{discrete}(x) = I(x) \cdot \text{III}_{\Delta x}(x) \tag{2.54}$$

In this equation, $\text{III}_{\Delta x}(x)$ is the Dirac comb function with period $\Delta x$, meaning that for argument $x$, the result is 1 when $x = \Delta x$ and 0 otherwise. This results in an interferogram

with sample points at $x = \pm n\Delta x \in [-L, L]$, with $n = 0, 1, 2...$

In the spectral space, this leads to an effect known as aliasing. Recalling equation 2.50, this multiplication in interferogram space leads to a convolution of the desired spectrum with a Dirac comb of width $1/\Delta x$ in spectral space. Thus, taking a Fourier transform of a discretely sampled interferogram causes the spectrum to repeat itself on an interval of $1/\Delta x$. The final measured spectrum is the sum of all repeated intervals; this means that aliasing can cause data outside of a certain range to distort the spectrum retrieved.

This distortion is avoided with the following relationship:

$$\sigma_{max} = \frac{1}{2\Delta x} \tag{2.55}$$

or, rearranged:

$$\Delta x = \frac{1}{2\sigma_{max}} \tag{2.56}$$

This relationship indicates that the maximum retrievable wavenumber is limited by the interferogram sample spacing as in 2.55, or alternately that a specific interferogram spacing needs to be chosen to ensure that a certain maximum wavenumber is retrievable. In this manner, the spectrum in the range $[-\sigma_{max}, \sigma_{max}]$ has no loss of information due to aliasing, according to the Nyquist sampling theorem. The maximum wavenumber described in 2.55 and 2.56 is considered as the Nyquist frequency.

In signal recreation, when all signals are in a range $(n-1) \cdot \sigma_{max}/2$ to $n \cdot \sigma_{max}/2$ the spectrum can be reproduced, but the transformation of the interferogram needs to be considered as well. If $n$ is even, the spectral information for the signal appears in the range $[-\sigma_{max}, 0]$, or the first half of the Fourier transform of the interferogram. Similarly, if $n$ is odd, the latter half of the data contains the spectral information to be retrieved, from the range $[0, \sigma_{max}]$. It is important to note what the value $n$ is for the spectra sought and how it relates to the Nyquist frequency; this knowledge allows reconstruction of the spectrum.

### Discrete Spectrum

The interferogram is discrete, and the Fourier transform applied to such data is typically calculated at discrete points as well, resulting in a returned spectrum that is discrete rather

than continuous. In theory, this is thought of as a multiplication of the original spectrum with a Dirac comb. The spacing of this comb is the spectral sampling, and has the form

$$\delta\sigma = \frac{1}{2L} = \frac{1}{N\Delta x} \tag{2.57}$$

Recall that $L$ represents the maximum length the mirror moves in one direction, so total interferogram length from one end to the other spans a distance of $2L$. With a sample spacing of $\Delta x$, this gives an interferogram $N = 2L/\Delta x$ samples. Using convolution theory again, equation 2.57 implies that the discrete interferogram repeats with a period of $2L$. Aliasing effects do not occur here, as the interferogram in the range $[-L, L]$ meets the Nyquist criteria.

The form of a discrete Fourier transform (DFT) needs consideration as well. Taking the DFT of an interferogram with $N$ points results in a spectrum that has $N/2$ points. In discrete notation, equations 2.45 and 2.46 become:

$$I(x_j) = \frac{1}{N}\sum_{k=1}^{N} S(\sigma_k)e^{i2\pi x_j \sigma_k} \tag{2.58}$$

$$S(\sigma_k) = \frac{1}{N}\sum_{j=1}^{N} I(x_j)e^{-i2\pi x_j \sigma_k} \tag{2.59}$$

**Summary of Discretization Effects**

The non-idealities discussed thus far have all dealt with the transformation from continuous space to discrete space in one form or another. Examined here are the total theoretical effects of these transformations on the interferogram and spectrum.

For the interferogram, a continuous signal is multiplied by a rectangular window of length $[-L, L]$, multiplied by a Dirac comb of width $\Delta x$ and convolved with a Dirac comb of width $2L$, resulting in

$$I_{FTS}(x) = \left[I(x) \cdot \Pi\left(\frac{x}{2L}\right) \cdot \mathrm{III}_{\Delta x}(x)\right] \otimes \mathrm{III}_{2L}(x) \tag{2.60}$$

The spectrum that is returned by an FTS can be represented by the continuous spectrum convolved with a sinc function, convolved with a Dirac comb of width $1/\Delta x$, and multiplied by a Dirac comb of width $1/2L = \delta\sigma$, obtaining

$$S_{FTS}(\sigma) = \left[S(\sigma) \otimes [2L \cdot \mathrm{sinc}(2\pi\sigma L)] \otimes \mathrm{III}_{1/(\Delta x)}(\sigma)\right] \cdot \mathrm{III}_{\delta\sigma}(\sigma) \tag{2.61}$$

Equations 2.60 and 2.61 show the theoretical effects of passing through an FTS. Thus, a properly modelled FTS system is equivalent to these equations.

### Finite Aperture

For any spectroscopic instrument, limitations are introduced by the physical effects of finite aperture size. The aperture size limits the throughput available to the system and is closely related to the solid angle and field of view of the instrument. These limitations must be well understood to design any spectrometer, as they introduce parameters which must be met for physical operation.

In this consideration, the highest wavenumber admitted to the system is analyzed because the interference patterns are more sensitive to OPD changes at higher wavenumbers. Recall $x = \left(n + \frac{1}{2}\right)\lambda$ for destructive interference and $x = n\lambda$ for constructive interference, when $n = 0, 1, 2....$ These relations tell us that the OPD required between alternating fringes is smaller when $\lambda$ is smaller, and a small wavelength corresponds to a large wavenumber.

Recalling the signal intensity of a monochromatic source given in equation 2.40 is the modulated and unmodulated portion of the interferogram, the average is subtracted to obtain just the modulated portion. For the sake of simplicity and clarity in the following equations, $S(\sigma_0)$ which defines the radiance of the source is set equal to unity. The method by which this analysis is done follows that done by Davis et al., (2001) [30].

$$I_{0,modulated}(x) = \cos(2\pi\sigma_0 x) \tag{2.62}$$

Now, considering off-axis and solid angle effects, equation 2.62 needs to be integrated with respect to the solid angle subtended by the pixel. In conjunction with off axis effects (see section 2.3 and equation 2.72 for details), this results in

$$dI = d\Omega\cos(2\pi\sigma_0 x\cos\alpha) \tag{2.63}$$

where $d\Omega$ represents a small amount of the solid angle at angle $\alpha$. Considering the small angle approximation $\cos\alpha \sim 1 - \frac{\alpha^2}{2}$,

$$dI = d\Omega\cos(2\pi\sigma_0 x[1 - \frac{\alpha^2}{2}]) \tag{2.64}$$

If $d\Omega$ is a ring at $\alpha$, letting $\Omega$ equal the area inside leads to

$$\Omega = \pi\alpha^2$$
$$\frac{\alpha^2}{2} = \frac{\Omega}{2\pi} \tag{2.65}$$

Assuming circular symmetry and a pixel centered on the optical axis, integrating for the range 0 to the maximum solid angle for the pixel, $\Omega_m$ leads to:

$$I = \int_0^{\Omega_m} \cos(2\pi\sigma_0 x[1 - \frac{\Omega}{2\pi}])d\Omega$$
$$I = \Omega_m \text{sinc}\frac{\sigma_0 x\Omega_m}{2\pi}\cos(2\pi\sigma_0 x[1 - \frac{\Omega_m}{4\pi}]) \tag{2.66}$$

In comparison to equation 2.62, $I$ has two major changes. The first is the term inside the cosine, $1 - \Omega_m/4\pi$, which indicates that there is a change in spectral scale when considering averaging effects. Thus, when a resultant spectrum is obtained from such an interferogram, the wavenumbers recovered will be shifted by this amount. This effect is easily corrected by setting all obtained wavenumbers equal to $\sigma(1 - \Omega_m/4\pi)$, and finding $\sigma$.

The second effect is the multiplication of the interferogram by a sinc function. Knowing that a sinc function has a maximum with argument zero, this indicates that incident radiance signal decreases as the solid angle increases. These effects are dealt with in more depth in section 2.3, but this averaging effect makes logical sense; a larger detector will average some areas of constructive interference and some areas of destructive interference without any ability to differentiate between the zones, reducing the contrast between fringes. The trade-off here is that the detector throughput increases, which increases signal levels at a greater rate than the signal reduction caused by the sinc term. This is true provided the sinc function argument is less than one, as beyond this value the sinc function becomes negative, which means that after this point a large pixel will exhibit a reduced signal. This removes the benefits of the large pixel. Thus, the acceptable range is $0<\frac{\sigma x\Omega_m}{2\pi}<1$.

At the maximum path difference offered by the system, $x = L$, maximum resolving power is found as (using 2.57)

$$R = \frac{\sigma}{\delta\sigma} = 2L\sigma \tag{2.67}$$

and defining a value $k$ for the argument to the sinc function

$$k = \frac{\sigma x\Omega_m}{2\pi} = \frac{R\Omega_m}{4\pi} \tag{2.68}$$

that must be less than 1, this definition of $k$ represents the number of fringes that are incident over a single pixel. Continuing with the analysis of the largest wavenumber for the longest path difference, the optimization criteria is to maximize this sinc function amplitude. The term to maximize is

$$\Omega_m \text{sinc} \frac{\sigma_0 L \Omega_m}{2\pi} = \Omega_m \frac{\sin(\sigma_0 L \Omega_m / 2)}{\sigma_0 L \Omega_m / 2} = \frac{2}{\sigma_0 L} \sin \frac{\sigma_0 L \Omega_m}{2} \tag{2.69}$$

which means the maximum is determined by setting the argument of the sine function to $\pi/2$. Thus, with equation 2.68

$$\frac{\pi}{2} = \frac{\sigma_0 L \Omega_m}{2} = k\pi$$

$$\frac{1}{2} = k \tag{2.70}$$

This indicates that the optimization requires that no more than 1/2 of a fringe is incident upon the pixel. An illustration of this sinc function is shown in figure 2.11

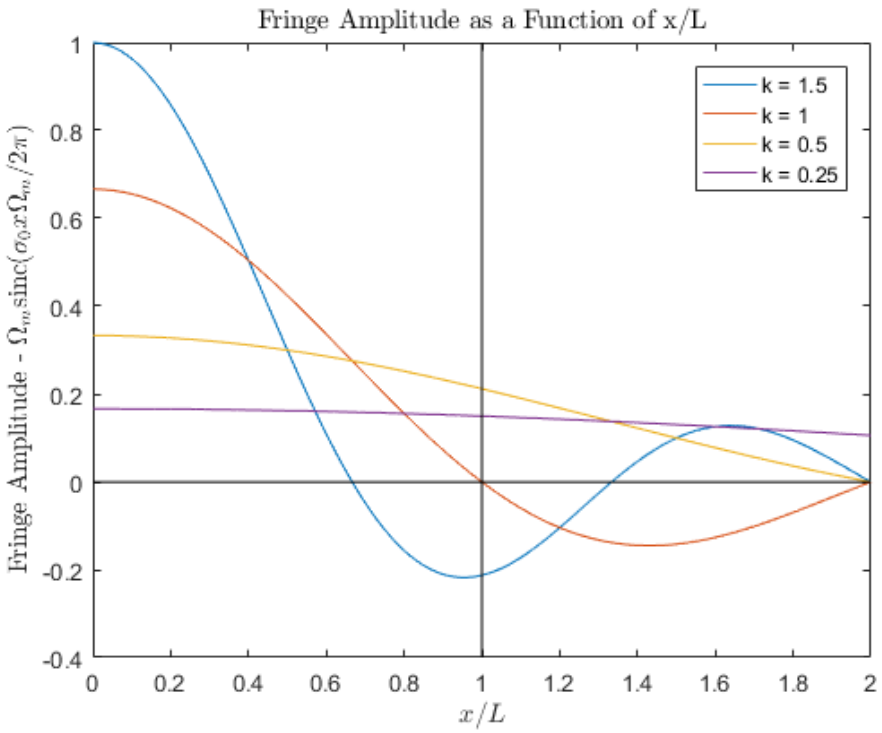


**Figure 2.11:** Fringe amplitude as a function of path difference for different number of incident fringes.

In this figure, the expected fringe amplitude as a function of mirror path difference is given. The $k$ value of each curve indicates the number of fringes incident across the pixel. This shows that while having many fringes leads to a large amplitude signal at ZPD, when the interferometer reaches the limits of motion, information is lost due to the averaging effect. From the figure, it is seen that when $k = 0.5$, a balance is obtained between high amplitude for all mirror positions.

Note that this argument is applied to a pixel centered on the optical axis. From a practical perspective, the half-fringe criteria discussed here applies to off-axis pixels as well, though additional considerations are required.

These off-axis effects also cause a signal reduction, due to averaging. The expected reduction in signal levels is approximated by determining the value of $\text{sinc}\frac{\sigma_0 L\Omega_m}{2\pi}$ at the value $k = \frac{1}{2}$. From figure 2.12, this value is approximately $M = 0.64$ at the half-fringe criteria.

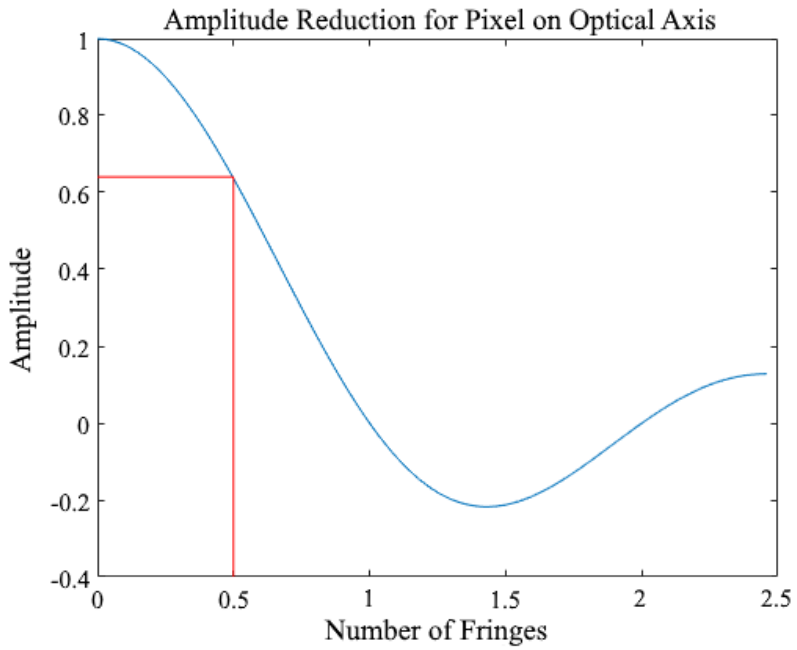


**Figure 2.12:** The amplitude reduction associated with the number of fringes incident across a pixel. The red line shows the half fringe criteria value.

It should be noted that a much more rigorous method of determining this modulation factor for off-axis pixels exists, in the form of [32]

$$M(\alpha_0, \rho_0) = \left[1 - \frac{(2\pi\sigma x)^2\Omega}{8\pi}\left(\sin^2(\alpha_0) + \frac{\Omega}{12\pi}\right)\right] \tag{2.71}$$

where $\rho_0$ is the azimuthal angle associated with $\alpha_0$ and all other variables are as previously defined. The more general solution to this integral requires Lommel functions in the case where $\alpha \neq 0$ [32]. This integration adds a large amount of complexity to the model. For the purposes of this thesis, the faster and less accurate modulation factor determined with the sinc function is used instead of equation 2.71, with the understanding that the true modulation factor can also be determined experimentally and is included in the characterization and calibration methodology.

## 2.3 Imaging FTS

An imaging FTS makes use of the theory presented in section 2.2.2 regarding the operation of the interferometer but uses an array of detectors instead of a single element. This allows the instrument to view different locations at the same time but introduces additional design considerations due to the introduction of elements that do not lie along the optical axis.

Traditionally, FTS instruments have utilized single pixel electronics to sample the interferograms. For limb imaging, as discussed in the introduction, this requires scanning the instrument up and down the limb. With the advancement of two-dimensional detector technology in the UV-IR range, new concepts are applied to take advantage of imaging aspects of the detectors.

For the imaging FTS, the imaging system is designed to form an image of the Haidinger fringes (discussed later in this section) conjugate to the scene of interest on an array detector. This allows for simultaneous samples of the spectral scene information to be obtained from different altitudes.

The simplified geometry showing the relationship between off-axis rays at an angle $\alpha$ and the incident location of those rays on the detector, $r$, is shown in figure 2.13.

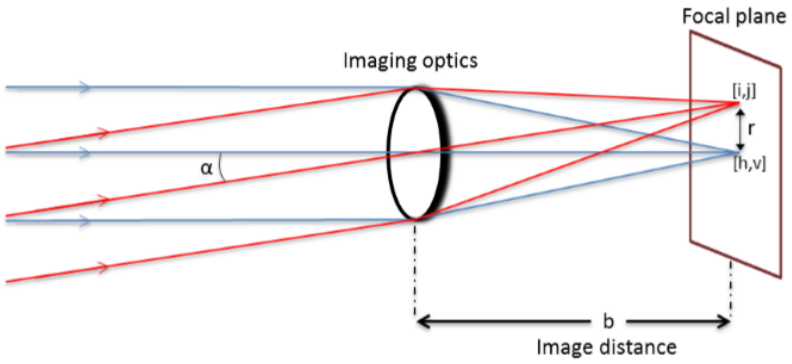


**Figure 2.13:** Ray diagram for on-axis and off-axis pixels. Index (h,v) represents a point on the optical axis, and (i,j) represents the position of a pixel that is off-axis. r is the distance between the distance between the two points, $\alpha$ is the off-axis angle and b is the image distance [13].

For most use cases, collimated light is incident to the entrance of the interferometer. Collimated light rays travelling parallel to the instrument optical axis are focussed to the center at (h,v). Rays that travel at an angle defined by $\alpha$ are focussed to an off-axis location, a pixel denoted by index (i,j). The challenge associated with this geometry is that the off-axis pixels have an optical path difference that is modified by the incident angle $\alpha$. The OPD for a given pixel (i,j) is expressed as

$$x_{i,j} = x_0 \cos(\alpha_{i,j}) \tag{2.72}$$

where $x_0$ is the OPD for the on-axis point, and $\alpha_{i,j}$ is the off-axis angle for a pixel located at (i,j).

This angular dependence of the OPD for off-axis pixels results in a circular fringe pattern, known as Haidinger fringes, at each mirror position in a scan. This pattern changes with each step of the interferometer mirror, and each pixel takes an independent measurement of the fringe pattern incident across its area for each mirror location. Figure 2.14 shows a simulated two-dimensional image of a Haidinger fringe pattern. This simulation uses a Michelson interferometer with MPD $L = 1$ cm, off-axis angle $\alpha = 2.85°$, and a monochromatic source of $\sigma = 1400$ cm$^{-1}$.

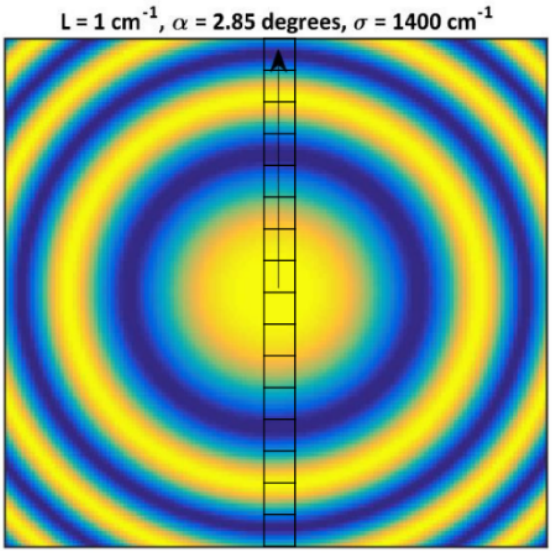


**Figure 2.14:** A simulated Haidinger Fringe pattern with a hypothetical detector array overlay.

Overlaid on the Haidinger fringe pattern is an idealized set of bins in a 1x16 linear array, showing the areas that each pixel in a hypothetical sensor detects. Each of these bins averages a finite portion of the interference pattern incident across their area. The Haidinger pattern observed shows areas of high signal caused by constructive interference (yellow) and areas of low signal caused by destructive interference (blue). For each mirror position, a different Haidinger pattern is created, and each pixel records a unique interferogram over the course of the mirror scanning from $[-L, L]$.

Recalling the discussion of section 2.2.4, the effects of this averaging are a reduction in the coherence between the interfering beams. To ensure that the imaging array maintains the best possible resolving power across all pixels, the bin size and spacing must be chosen such that no more than half of a fringe crosses the field of view for any pixel.

## 2.4 Detector of IR Radiation

Many materials exist for imaging detectors, such as bolometers, pyroelectric detectors, quantum well infrared photodetectors (QWIP), and Mercury cadmium telluride (HgCdTe or

MCT) detectors. For the discussion in this thesis, the detector chosen is the photoconductive MCT for their versatility and unique advantages offered. Among the advantages are the ability to adjust energy gaps by changing composition, small effective mass and high carrier mobility, long minority carrier lifetime, and low carrier concentration [33]. MCT detectors are typically used to make measurements in the short- mid- and long-wave infrared atmospheric windows; the MCT boasts high response and sensitivity to infrared radiation. This high sensitivity, however, means that many components of an IFTS utilizing an MCT must be temperature controlled.

Photoconductive detectors have three major sources of noise that are considered in this model. These are the thermal Johnson noise, generation-recombination (g-r) noise inherent to the detector, and background Generation-Recombination noise caused by background flux incident on the detector. The theory discussed here follows the discussion by Dwivedi and Chakrabarti [34]

In addition to these sources of error in the detector measurements, there are sources of error associated with the operation of the interferometer. These errors result in another source of uncertainty and noise in the measurements and are discussed as well.

### Sampling Noise

In the discussion of noise, a value known as the frequency bandwidth, $B_w$ or $\delta f$, is often required. This parameter is Nyquist frequency set by the sampling frequency of the system. The equation for this effective bandwidth is [32];

$$B_w = \delta f = f_{Ny} = \frac{1}{2} f_{samp} = \frac{1}{2t_{samp}} = \frac{N}{2T} \tag{2.73}$$

where $N$ is the total number of samples taken by the detector (equivalently, the number of points in a full interferogram) and $T$ is the total duration of an interferometer scan.

### Thermal Johnson Noise

This noise is due to the latent energy of charge carriers that exist even in the absence of an applied voltage. Since these charge carriers always have energy of some sort, the detector always reads some baseline for change in voltage. This value must be accounted for, because

this means not all voltage measured with incident photons is due solely to the scene. The Johnson noise for a photoconductor is given by equation 2.74. [34]

$$V_j = \left( \frac{4kTlB_w}{(qwt(n_0\mu_n + p_0\mu_p))} \right)^{1/2} \tag{2.74}$$

where $k$ is the Boltzmann constant, $T$ is the temperature of the detector in Kelvin, $l$, $w$ and $t$ are the length, width, and thickness (or depth) of the detector element, $B_w$ is the frequency bandwidth of the instrument, $q$ is the charge of an electron, $n_0$ and $p_0$ are the carrier concentrations of electrons and holes, respectively, and $\mu_n$ and $\mu_p$ are electron and hole mobility, respectively. The resulting measurement of noise has units of volts.

### G-R Noise

This noise is the result of fluctuations in the rate at which generation and recombination of free charge carriers occurs. The noise this causes in voltage readings is given by equation 2.75 [34] [35]

$$V_{gr} = \frac{2V_a}{(lwt)^{1/2}} \frac{1+b}{n_0 b + p_0} \left( \frac{n_0 p_0}{n_0 + p_0} \right)^{1/2} \left( \frac{\tau_e B_w}{1 + 4\pi^2 f^2 \tau_e^2} \right)^{1/2} \tag{2.75}$$

where $V_a$ is the voltage applied for operation, $b$ is the ratio of electron to hole mobility, $f$ is the frequency of the modulating signal, $\tau_e$ is the effective lifetime of a charge carrier, and all other variable are as previously defined. The units are in volts.

### Background Flux Noise

This source of noise is caused by background photon flux incident on the detector, and is given by the following:

$$V_B = 2qR\frac{\mu n E_a}{l}\tau_e\sqrt{lwt}\sqrt{\frac{\eta\varphi_B B_w}{t}} \tag{2.76}$$

Where $R$ is the detector resistance, $E_a$ is the applied electric field caused by $V_a$, $\eta$ is the internal quantum efficiency of the detector and $\varphi_B$ is the background photon flux. The units of this equation are volts.

### Total Voltage Noise

The root-mean-square (rms) voltage caused by these major sources together are obtained as

$$V_n = \sqrt{\left(V_j^2 + V_{gr}^2 + V_B^2\right)} \tag{2.77}$$

This noise is representative of an average error in voltage given off by the detector when making measurements. In general, each measurement in an interferogram is approximately $V_n$ volts larger than it should be. While variations from measurement to measurement cause errors in the modulated portion of an interferogram and must be considered, a large portion of this noise effects are expected to be removed with the averaging to remove the unmodulated term.

### Interferometer Noise

The theory of an IFTS works on the assumption that the data points are evenly spaced in the spatial domain of the moving mirror, but actual measurements are evenly spaced in the time domain. These evenly spaced samples have no established connection to the OPD due to vibrations of mechanical limitations that limit the perfect scanning motion of the mirror. That is, no OPD value can be assigned absolutely to each sample. For this reason, an IFTS requires what is known as a metrology system, consisting of a reference laser of known wavelength that is sampled at the maxima, zero crossings or minima of the signal as a function of time. Since the wavelength of the reference laser is known, a mapping of OPD as a function of time is developed and can be applied to the interferogram samples. Further complications are introduced by variations in mirror velocity caused by vibrations in the instrument, which lead to additional position errors. All undamped vibrations in the system, such as from the cooler or operating electronics, have the potential to influence the velocity of the mirrors. This position uncertainty leads directly to an error in the frequency of the interferogram signal and leads to a phenomenon known as “ghosts” in the returned spectra after Fourier transformation. The metrology signal allows for correction of these issues through the process of uniform time sampling (UTS) algorithms, discussed in section 6.9.

While the UTS algorithms reduce the position errors, there is still an error associated with the accuracy of the metrology signal capture. Uncertainty in the metrology signal capture cannot be removed, and so requires a system that is able to capture the signal within acceptable uncertainty limits. The capture of this signal is done with software, hardware, or a combination of the two. The speed at which the signal is processed is the limiting factor for this source of noise in the interferogram.

Another interferometer related source of noise comes in the form of the alignment of the corner cubes. If the alignment shifts, the modulation transfer efficiency of the system will change over time.

## 2.5 Trace Gas Retrievals using Limb Imaging FTS

An IFTS system as described, in the limb viewing geometry, views several different paths along the atmosphere, and gathers information along those paths. These measurements that are taken are a result of the atmospheric make-up, which is the information that is sought. This is generally known as the inverse problem, or as inversion theory. The IFTS takes measurements samples of the limb conjugate to the Haidinger fringes; the light detected is encoded with the spectral information of the scene, and the inverse problem is to extract this information and determine the vertical distribution of trace species that are present in the scene.

The arguments presented here follow from *Inverse Methods for Atmospheric Sounding Theory and Practice* by Clive D. Rodgers [1]. This section discusses what the inverse problem is, and methods of solution.

### The Inverse Problem

In general function, a result is determined by a function that takes known inputs as argument and returns a result. This can take the general form of

$$f(\mathbf{x},\mathbf{b}) = \mathbf{y} + \epsilon \tag{2.78}$$

where $f$ is the forward model, a function that encapsulates the physics involved in the measurements, $\mathbf{x}$ is a vector of length $n$ of whatever a user is interested in, $\mathbf{b}$ is auxiliary

information, $\mathbf{y}$ is a vector of length $m$ of measurements and $\epsilon$ is the vector containing the error in those measurements.

The issue that arises is that $\mathbf{y}$ is the resultant information, corresponding to known measurements, and $\mathbf{x}$ is an input to the function but is unknown. Thus, the forward model must be inverted to find a solution. However, this inversion is not simple because $f$ is usually non-linear. Additionally, atmospheric inverse problems are fundamentally ill-posed, meaning the measurements do not contain enough information to fully describe the vector $\mathbf{x}$.

The solution to the inverse problem then requires many considerations and a series of parameters to be developed, which is the fundamental idea behind the retrieval method.

### 2.5.1 Linear Case

The starting point for the solution is the linear case in the absence of error. In this form, a simple inversion is possible in the form of

$$\mathbf{y} = \mathbf{K}\mathbf{x} \tag{2.79}$$

where $K$ is an $m \times n$ matrix. The rank of $K$ is assumed to be the minimum of $m$ and $n$, meaning that $K$ is full rank. There are three cases that result from this: $n = m$, $n < m$ (overdetermined), or $n > m$ (underdetermined).

In the simplest case when $n = m$, $K$ is square and invertible and there exists one "exact" solution

$$\mathbf{x} = \mathbf{K}^{-1}\mathbf{y} \tag{2.80}$$

This is rarely the case in real problems, unless the problem is specifically engineered.

The underdetermined case of $n > m$, also known as ill-posed, has infinitely many solutions. This occurs because there is an attempt to retrieve more information than there is available from measurements. Solutions to this problem require another source of information, such as lowering the resolution of the retrieval grid, the acquisition of more measurements, or the addition of a constraint.

Overdetermined cases, when $n < m$, have no solution that perfectly matches all data. As an example, a solution of the inverse problem may match two of the three measurements,

and not the third. This illustrates the need for error in the model, to allow for discrepancies arising in the measurement values that are not matched. Ideal solutions are those that fit within error criteria.

Determination of the best possible $\mathbf{x}$ is done by minimizing the least squares difference between the measurements and the model,

$$\chi^2 = (\mathbf{y} - \mathbf{K}\mathbf{x})^T(\mathbf{y} - \mathbf{K}\mathbf{x}) \tag{2.81}$$

and setting the derivative to zero

$$\nabla_{\mathbf{x}}\chi^2 = -\mathbf{K}^T(\mathbf{y} - \mathbf{K}\mathbf{x}) - (\mathbf{y} - \mathbf{K}\mathbf{x})^T\mathbf{K} = 0$$

$$\mathbf{K}^T\mathbf{K}\mathbf{x} = \mathbf{K}^T\mathbf{y}$$

$$\mathbf{x} = (\mathbf{K}^T\mathbf{K})^{-1}\mathbf{K}^T\mathbf{y} \tag{2.82}$$

**Including Error**

Any practical retrieval must allow for experimental error and noise in the measurements, as no measurement is made without these effects. It is for this reason that any measurement is described by a probability density function. Considering a Gaussian case, a typical and robust assumption for many statistical phenomena, a probability density function is expressed as

$$P(\mathbf{y}) \sim \exp\left[-\frac{1}{2}(\mathbf{y} - \bar{\mathbf{y}})^T\mathbf{S}_{\mathbf{y}}^{-1}(\mathbf{y} - \bar{\mathbf{y}})\right] \tag{2.83}$$

with $\mathbf{S}_{\mathbf{y}}$ being a covariance matrix representing correlation between errors between channels,

$$\mathbf{S}_{ij} = \epsilon\{(y_i - \bar{y}_i)(y_j - \bar{y}_j)\} \tag{2.84}$$

Given that the quantity $\mathbf{K}\mathbf{x}$ is the best estimate for $\bar{\mathbf{y}}$ leads to the probability of measurement $\mathbf{y}$ occurring for a specific $\mathbf{x}$ of

$$P(\mathbf{y} \mid \mathbf{x}) \sim \exp\left[-\frac{1}{2}(\mathbf{y} - \mathbf{K}\mathbf{x})^T\mathbf{S}_{\mathbf{y}}^{-1}(\mathbf{y} - \mathbf{K}\mathbf{x})\right] \tag{2.85}$$

Where the maximum likelihood solution is at the maximum of this probability density function. Now, least squares difference takes the form of

$$\chi^2 = (\mathbf{y} - \mathbf{K}\mathbf{x})^T\mathbf{S}_{\mathbf{y}}^{-1}(\mathbf{y} - \mathbf{K}\mathbf{x}) \tag{2.86}$$

Setting the derivative of equation 2.86 to zero, leads to the most likely solution from a probabilistic perspective of

$$\mathbf{x} = (\mathbf{K}^T\mathbf{S}_\mathbf{y}^{-1}\mathbf{K})^{-1}\mathbf{S}_\mathbf{y}^{-1}\mathbf{K}^T\mathbf{y} \tag{2.87}$$

However, there are issues that arise with this form as well; a proper solution cannot be found if $\mathbf{K}^T\mathbf{S}_\mathbf{y}^{-1}\mathbf{K}$ is non-invertible (underdetermined or non-trivial null-space), and even if it is there is no guarantee that it is well-behaved. This leads to the need for additional information.

### A priori information

The additional information required here is *a priori* information, that is, information about the atmosphere that is known prior to the measurements. This information can be represented by a Gaussian probability density function,

$$P(\mathbf{x}) \sim \exp\left[-\frac{1}{2}(\mathbf{x}-\mathbf{x}_a)^T\mathbf{S}_a^{-1}(\mathbf{x}-\mathbf{x}_a)\right] \tag{2.88}$$

where $\mathbf{x}_a$ is the prior knowledge of vector $\mathbf{x}$. This leads to a least squares solution for a modified equation 2.86 of

$$\chi^2 = (\mathbf{y}-\mathbf{K}\mathbf{x})^T\mathbf{S}_\mathbf{y}^{-1}(\mathbf{y}-\mathbf{K}\mathbf{x}) + (\mathbf{x}-\mathbf{x}_a)^T\mathbf{S}_a^{-1}(\mathbf{x}-\mathbf{x}_a) \tag{2.89}$$

and further results in a solution for $\mathbf{x}$

$$\hat{\mathbf{x}} = \mathbf{x}_a + (\mathbf{K}^T\mathbf{S}_\epsilon^{-1}\mathbf{K} + \mathbf{S}_a^{-1})^{-1}\mathbf{K}^T\mathbf{S}_\epsilon^{-1}(\mathbf{y}-\mathbf{K}\mathbf{x}_a) \tag{2.90}$$

where $\mathbf{S}_\epsilon$ is a more generalized form for error covariance matrix previously defined as $\mathbf{S}_\mathbf{y}$. Equation 2.90 represents the maximum a posteriori solution, the vector $\mathbf{x}$ for which the probability of $\mathbf{x}$ is maximized for a given measurement vector $\mathbf{y}$.

### Regularization

The introduction of the $\mathbf{S}_a$ term requires special consideration. A common choice is to use Tikhonov regularization of the first or second order to determine the value of $\mathbf{S}_a$. For this regularization method,

$$\mathbf{S}_a^{-1} = \Gamma^T\Gamma \tag{2.91}$$

where

$$\Gamma = \alpha \begin{pmatrix} 1 & -1 & 0 & 0 & 0 & \dots \\ 0 & 1 & -1 & 0 & 0 & \dots \\ 0 & 0 & 1 & -1 & 0 & \dots \\ & & & & & \ddots \end{pmatrix} \tag{2.92}$$

for first-order and

$$\Gamma = \alpha \begin{pmatrix} -1 & 2 & -1 & 0 & 0 & \dots \\ 0 & -1 & 2 & -1 & 0 & \dots \\ 0 & 0 & -1 & 2 & 1 & \dots \\ & & & & & \ddots \end{pmatrix} \tag{2.93}$$

for second-order, where $\alpha$ is a tuning parameter. These regularization methods ensure that either the first derivative or second derivative of the solution is continuous or well-behaved. Without this regularization, retrievals tend to attempt to overfit, causing unrealistic oscillations.

### Non-linear Case

Problems are divided up into three degrees of linearity. These are linear, as discussed previously, moderately non-linear, and highly non-linear. Moderately non-linear systems are linear for values on the order of measurement noise, meaning that the inverse problem can be solved by linearizing the system and iteratively solving. This is not possible for highly non-linear systems; the method outlined in this thesis cannot be applied to highly non-linear cases.

The retrieval of atmospheric trace gases classifies as a moderately non-linear problem, so linearization and iteration can be used to solve the system. This requires modifications to the equations presented. Now, the matrix $\mathbf{K}$ must be replaced with a model of the physics present in the problem, leading equation 2.89 to become

$$\chi^2 = (\mathbf{y} - F(\mathbf{x}))^T \mathbf{S}_\mathbf{y}^{-1} (\mathbf{y} - F(\mathbf{x})) + (\mathbf{x} - \mathbf{x}_a)^T \mathbf{S}_a^{-1} (\mathbf{x} - \mathbf{x}_a) \tag{2.94}$$

Taking the derivative and setting it equal to zero as before,

$$-[\nabla_\mathbf{x} F(\mathbf{x})]^T \mathbf{S}_\epsilon^{-1} [(\mathbf{y} - F(\mathbf{x}))] + \mathbf{S}_a^{-1} (\mathbf{x} - \mathbf{x}_a) = 0 \tag{2.95}$$

Then, define

$$\nabla_{\mathbf{x}} F(\mathbf{x}) = \frac{\partial F(\mathbf{x})}{\partial \mathbf{x}} = \mathbf{K}(\mathbf{x}) = \mathbf{K} \tag{2.96}$$

Thus, an equation is obtained,

$$g(\mathbf{x}) = -\mathbf{K}^T \mathbf{S}_\epsilon^{-1}[\mathbf{y} - F(\mathbf{x})] + \mathbf{S}_a^{-1}(\mathbf{x} - \mathbf{x}_a) = 0 \tag{2.97}$$

to which Newton's method is applied:

$$\mathbf{x}_{i+1} = \mathbf{x}_i - [\nabla_{\mathbf{x}} g(\mathbf{x}_i)]^{-1} g(\mathbf{x}_i) \tag{2.98}$$

where

$$\nabla_{\mathbf{x}} g(\mathbf{x}) = \mathbf{K}^T \mathbf{S}_\epsilon^{-1} \mathbf{K} + \mathbf{S}_a^{-1} - [\nabla_{\mathbf{x}} \mathbf{K}^T] \mathbf{S}_\epsilon^{-1}[\mathbf{y} - F(\mathbf{x})] \tag{2.99}$$

**Gauss Newton Method**

The Gauss-Newton method is applied to equation 2.99, where the term $\nabla_{\mathbf{x}} K^T = 0$. This leads to the general equation representing the iterative solution approach to the moderately non-linear case:

$$\mathbf{x}_{i+1} = \mathbf{x}_i + (\mathbf{K}_i^T \mathbf{S}_\epsilon^{-1} \mathbf{K}_i + \mathbf{S}_a^{-1})^{-1}[\mathbf{K}_i^T \mathbf{S}_\epsilon^{-1}(\mathbf{y} - F(\mathbf{x}_i)) - \mathbf{S}_a^{-1}(\mathbf{x}_i - \mathbf{x}_a)] \tag{2.100}$$

The results of this equation from iteration to iteration are checked for convergence, of which there are several that can be chosen. Additional terms can also be added to damp oscillations around the end solution.

For this thesis, equation 2.100 is used, run a number of times specified by the user. Advanced methods are to be applied in future work on the LIFE instrument.

## 2.6 Summary

In this background section, an overview of all sections required for the development of a limb imaging FTS instrument is given. First, the composition of the atmosphere and a description of the propagation of thermal radiation is given, as well as the viewing geometry required for such an instrument. Together, these factors allow an understanding and development of

a forward model of all physics involved with generating a scene from the atmosphere that is incident to an instrument.

Second, the interferometer and the effects of this device on incident radiation is given. The accounting of how incident radiation is encoded into an interferogram and the addition of noise allows the development of an instrument model. With this model, when given a scene as input it is determined what the end result detected by the instrument is, with expected statistical variation.

Thirdly, the inverse problem is described, and a framework under which having a result allows determination of the conditions that create that result. In this case, this means that there is a way to create an atmosphere, determine what the detector would see from such an atmosphere, and a way to recreate the atmosphere from those measurements. In Chapter 3, this theory is applied to allow the development of an IFTS.

# Chapter 3

# Developing Measurement Simulator for an Infrared IFTS

This section details the development of an end-to-end measurement simulator for an IFTS instrument such as LIFE. This includes the forward model created to simulate atmospheric radiance profiles, the instrument model for a Michelson based imaging FTS, and aspects of optical design and noise considerations critical to the design of such a system. The code created for this thesis and used in the design of LIFE is based in MATLAB. In general terms, this section describes the implementation of all aspects covered in the Background in a simulation that facilitates the designing and analysis of an IFTS. The general form of the code and the parameters that can be changed are described and are divorced from the design decisions made for LIFE.

Using the information in the chapter, it is possible to design an IFTS and simulate the spectrum that it would obtain in the thermal regime. Note, however, that at the time of this thesis many of the more complex phenomena associated with the IFTS are temporarily neglected. These facets and the reasons for neglecting them are indicated in the relevant sections.

## 3.1 Forward Model

During the design of an instrument, a model of the physical phenomena to be studied is typically developed. For the case of a limb imaging FTS, the model includes the atmospheric composition and behaviour in the thermal regime. The physical model is used to simulate radiation that is input to an instrument model. Only by developing this "forward model"

can different design choices be examined and compared. In practice, the forward model is also utilized in the retrieval of atmospheric parameters, the ultimate end-goal of a remote sensing instrument. This section provides an overview of the forward model and retrieval architecture.

The forward model encompasses the knowledge of the physics involved, including atmospheric composition and behaviour as well as the knowledge of instrument behaviour. The model allows an observer to be placed in or above an atmosphere and simulate the data expected to be observed. There are two major portions to the forward model. The first is the radiative transfer model, concerned with determining the radiation reaching the instrument through the simulated atmosphere. The second is the instrument model, concerned with the encoding of atmospheric scene information into an interferogram generated at the detector.

### 3.1.1 Radiative Transfer Model

The radiative transfer model utilizes our knowledge of the atmosphere to simulate the process of radiative transfer through the simulated atmosphere. It deals with the solution to the radiative transfer equation, as discussed in section 2.1.2. This theory is applied to create a model in MATLAB. In the model, a representation of the atmosphere must be created that accounts for the physical properties exhibited by the atmosphere. Due to the spherical geometry of the Earth, the simplest and most common representation of the atmosphere is to consider it a series of spherical shells. This representation is then assigned values for temperature, pressure, number density of gas species and other information pertinent to the goals of the instrument being designed. Then an observer is placed in the atmosphere and the line of sight (LOS) of that observer must be defined. The LOS of the observer defines the path(s) along which the radiative transfer equation is to be applied.

In the radiative transfer model utilized in this thesis the atmosphere is generated as a series of shells of a chosen thickness. Each shell is given a temperature and pressure from a standard atmospheric state (such as MSIS90) that corresponds to the center altitude of that shell. An observer is placed in this atmosphere with a field of view (FOV) divided into several LOS. Figure 3.1 shows an idealization of the viewing geometry through the spherical shells of this atmosphere.

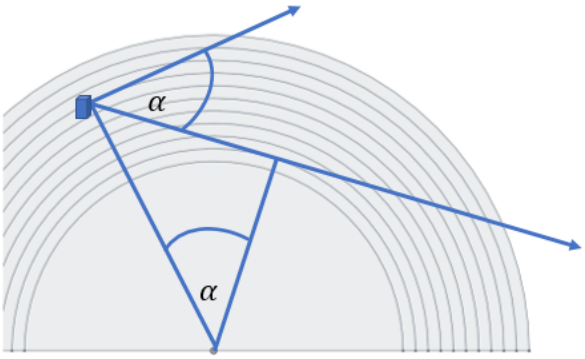


**Figure 3.1:** Idealization of limb IFTS viewing geometry. The instrument has an FOV defined by $\alpha$, which also defines the relationship between the observer and the tangent altitude for a given LOS.

For the IFTS developed in this thesis, the scene viewed through the limb is imaged conjugate to the Haidinger fringes on the detector. In this configuration, the vertical FOV at the limb is mapped one-to-one to pixel position on the detector. The number of pixels used in the detector array defines the number of LOS to be generated in the model. Each pixel covers a different portion of the full FOV and has a distinct LOS. Each of these LOS are mapped to a tangent altitude at the limb. Taking the angle $\alpha$ to be the angle measured from the uppermost possible LOS to the target LOS, the tangent altitude associated with the target is given by:

$$H_{tangent} = (R_E + H_{observer})\cos(\alpha) - R_E \tag{3.1}$$

where $R_E$ is the radius of the Earth, $H_{observer}$ is the altitude of the observer and $H_{tangent}$ defines the altitude of a sphere that is tangent to the considered LOS.

Thus, for any observer, if a series of viewing angles defined by the FOV and number of pixels are known, the view paths through the atmosphere are determined by equation 3.1. This information is used in conjunction with the multiple shells of the atmospheric model to create a series of cells to use with the radiative transfer equation defined by equation 2.28. In figure 3.1, each place where a LOS intersects an atmospheric shell is considered as the boundary to a cell.

Thus, the distance between two intersections is $\Delta x$ used in optical thickness calculations. With an atmosphere created, an observer is placed in the model and the geometry related to

how it views the environment are defined. This allows the application of the radiative transfer equation. Radiative transfer equations take different forms depending on the regime one is wanting to model. For example, in the visible-UV regime, scattering effects are extremely important, but scattering effects are minimal in the thermal regime. Thus, each has very different forms that need to be considered. LIFE makes use of the thermal regime.

The atmospheric model utilizes cells as described in section 2.1.3 and illustrated by figure 2.7. In a cell such as this, there are many different species present, each with a unique $\sigma$ and $n$ value. From 2.27, this means that each species has a unique optical thickness. The optical thickness used in 2.28 is the summation of the optical thicknesses of each species, $\tau = \tau_1 + \tau_2 + ...$ For a system that has multiple layers, a layer-by-layer approach is used, where the initial $I_0$ comes from some radiation source in the form of empty space or the ground, and the $I_f$ of this first layer is used as an input to the second layer. This pattern continues until the ray encounters the observer. With knowledge of how radiation propagates through layers with defined variables, it is possible to simulate the observed radiance.

The calculation of these pathlengths starts with defining a LOS and the accompanying tangent altitude. Taking these two parameters, the number of atmospheric layers relevant to the LOS for a limb view are determined by taking the total number of layers available and subtracting the number of layers that exist below the tangent altitude. However, this is only a measure of the number of layers that are above the tangent altitude, not the number of layers that are intersected. To find the maximum number of possible layers, this number is first doubled, then one is removed to account for the center layer being counted twice. This maximum number of layers is now representative of an observer existing *outside* of the atmosphere and looking along the defined LOS. Figure 2.9b of the background illustrates this situation.

The next step is to determine the pathlength between the intersection points defined by this geometry. This is done by cycling through the relevant layers and using the following formulae.

$$\Delta x_i = 2\sqrt{(R_E + (i)\Delta z)^2 - (R_E + H_{tangent})^2} \text{ (center layer)} \tag{3.2}$$

$$\Delta x_i = \sqrt{(R_E + (i)\Delta z)^2 - (R_E + H_{tangent})^2} - \sqrt{(R_E + (i-1)\Delta z)^2 - (R_E + H_{tangent})^2} \text{ (all others)} \tag{3.3}$$

where $i$ is the layer being examined, $\Delta z$ is the layer thickness and other variables are previously defined. Notice that the center layer has had the thickness doubled and only relevant layers are looped through; the model again makes use of the symmetry of the LOS to determine pathlengths for all potentially viewed layers.

The next step is to determine the layers viewed by an observer placed *inside* the atmosphere. This is done by determining the layer in which the observer sits, and the number of layers "above" the observer. In terms of the LOS, all layers meeting this criterion are behind the observer, and have no impact on the radiative transfer. The model has now defined a set of pathlengths for use in the radiative transfer equations.

The geometry has given the values for $\Delta x$ in determining $\tau$, now $n$ and $\sigma$ need to be determined as well. This step requires calls to other datasets that have accepted values. For determination of $\sigma$, the absorption/emission cross-section, the High-Resolution Transmission (HITRAN) database is used. For the current cell, the target species, altitude, and wavelength range are given to the database and an appropriate $\sigma$ value is returned, taking into account the effects of pressure broadening. Pressure broadening is the phenomenon where collisions between individual molecules of a species induce coupling between closely spaced spectral lines. Thus, at lower altitudes where pressure is higher and more collisions occur, the cross sections of molecules are broadened. Determination of $n$ for target species requires the input of an atmospheric profile that gives number density as a function of altitude. Starting at the layer farthest from the observer, these values are used to calculate the radiance output of equation 2.28. The process then moves to the next layer, where calculations are repeated and an output for that layer is computed. This continues until the layer of the observer is reached, at which point the final output defines the radiance viewed by the observer along the defined LOS. This entire process is repeated for each LOS.

The validity of the radiative transfer model was examined by comparison with a similar radiative transfer model utilized during the development of the GLORIA instrument [13]. Taking the observer position to be 40 km, the output of the radiative transfer equation for the 20 km tangent altitude is shown in figure 3.2 and figure 3.3 for the GLORIA and LIFE radiative transfer models, respectively.

In this comparison, the signature of each species is determined independently and then

superimposed. For the LIFE simulation, only $O_3$, $CO_2$, $H_2O$ and $N_2O$ are used, $CO_2$ included with the LIFE targets as it is radiatively significant, and $CH_4$ omitted due to an error in the cross-section database in the considered range that exists at the time of writing. Based on qualitative analysis of the two spectra, there is reasonable agreement between the GLORIA and LIFE models for these species.

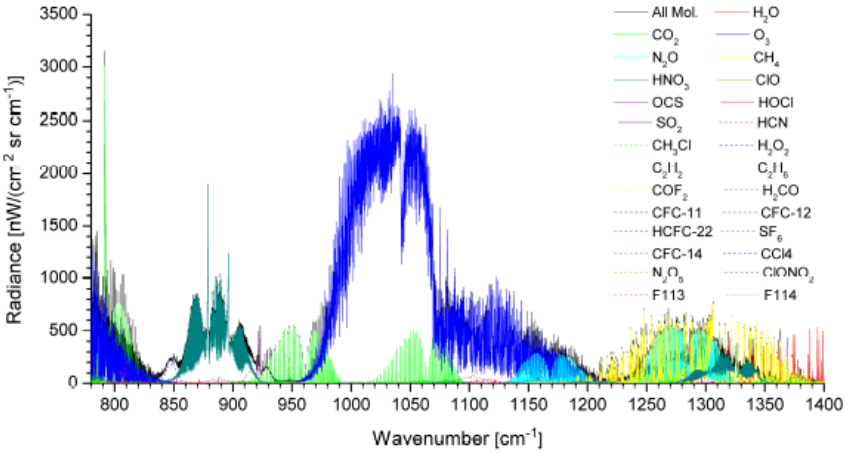


**Figure 3.2:** Forward calculated spectra for mid-latitude July standard atmosphere at 20 km tangent altitude as presented in M. K. Sha (2013) [13].

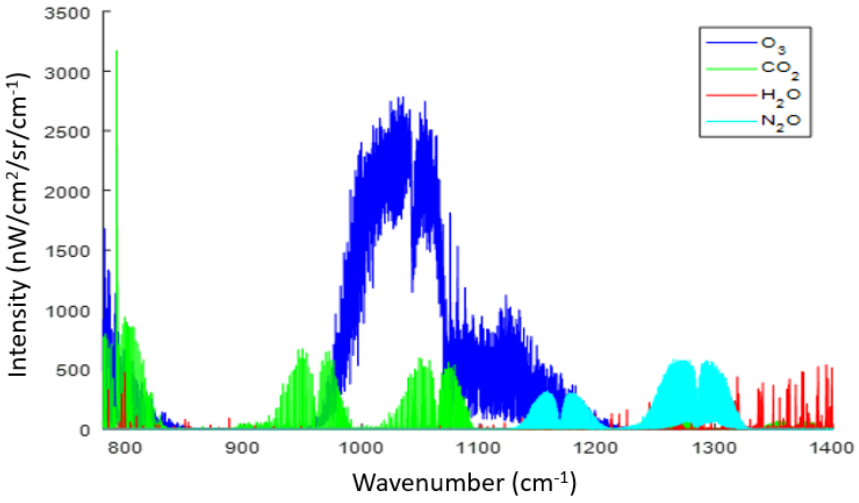


**Figure 3.3:** Superposition of individually calculated spectra for mid-latitude July standard atmosphere at 20 km tangent altitude as calculated by the radiative transfer model developed in this thesis.

Considering this result as a realistic representation of atmospheric signal levels, the results

of this model are used as input radiance to the instrument model. For the LIFE viewing geometry, the expected radiance for selected tangent altitudes is shown in figure 3.4. In these expected radiances, the radiance information for all species is combined.

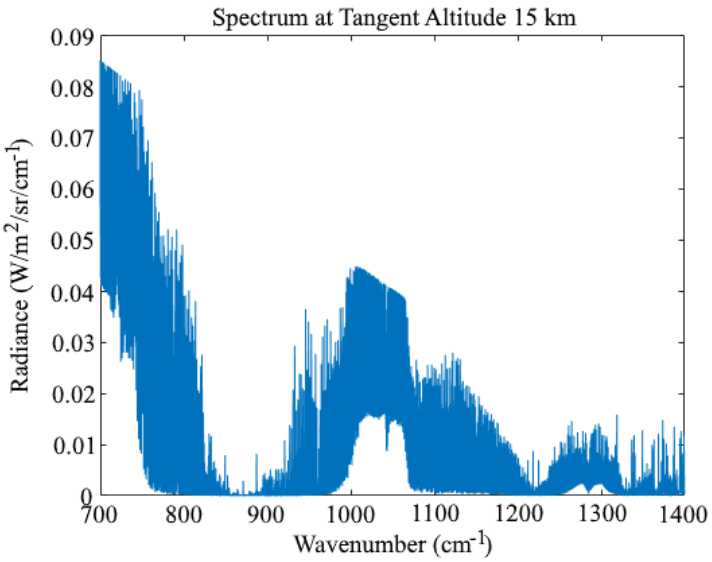


**Figure 3.4:** Forward calculated spectra for expected LIFE geometry.

From these figures, it is seen that there is variation in overall signal as a function of altitude. To view the sensitivity of these lines to different LOS, figure 3.5 shows a zoomed in, overlapped section to view how a few of the detected lines change as a function of altitude.

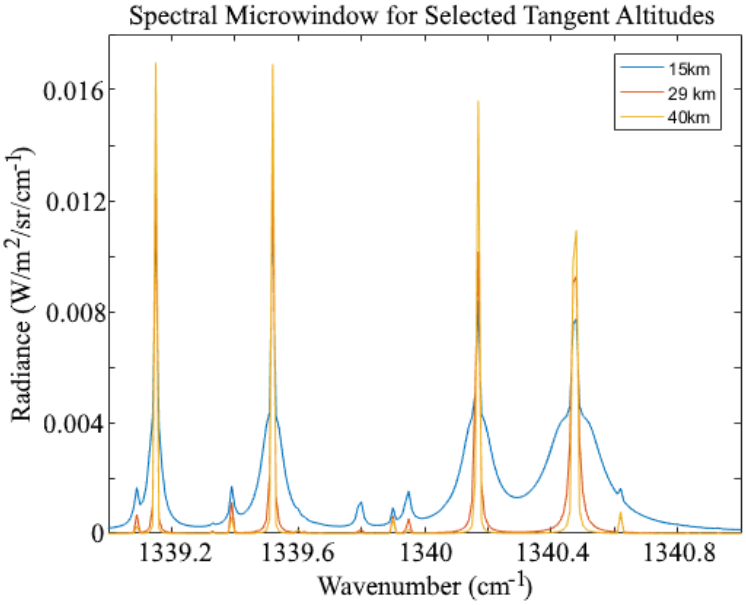

**Figure 3.5:** An arbitrary microwindow chosen to illustrate the effects of input spectra as a function of altitude.

This figure shows that the spectral features are broader at lower altitudes. This demonstrates the pressure broadening effects at lower altitudes due to higher pressures. Each cell in an LOS through the atmosphere has a different broadening based on altitude, and this is part of what allows the retrieval to determine abundances of the target species.

### 3.1.2 Instrument Model

The instrument model primarily deals with the application of theory described in section 2.2. Operation on an FTS in the thermal regime demands that great care be taken to understand the thermal emissions of the instrument, known as self-emission. Taking instrument self-emission into account, there are three sources typically given as incident upon a detector [15] [36]:

i) Scene radiation plus radiation of optical components between entrance and beamsplitter. The same number of reflections are present in both arms of the interferometer.

ii) Radiation emitted by optical components between the beamsplitter and detector. These sources pass through the beamsplitter in the opposite direction, and do not have the same number of reflections in each arm. These are out of phase with the radiation sources occurring before the beamsplitter by $\pi$.

iii) Beamsplitter self-emission, which is different in each arm of the interferometer. This source is out of phase with radiation sources occurring before the beamsplitter by $\pi/2$. Variation in dispersion through the beamsplitter creates additional phase differences.

At this time, the assumption is made that the self-emission is from the beamsplitter, and that it is in-phase with the scene signal, neglecting for now the phase errors associated with radiation emitted by the beamsplitter and optical components between the beamsplitter and detector. These sources primarily contribute to phase errors that require calibration for level 1 data acquisition. This is discussed more in the section 3.1.3. The final form of the interferogram incident upon the detector for the included sources is a modified form of equation 2.41,

$$I_{raw}(x,i,j) = \frac{1}{2}\int_{\sigma}^{\sigma_{max}} [\Re(\tau_{optics}S(\sigma) + \epsilon S_{instr}(\sigma))(1 + M\cos(2\pi\sigma x_{mapped}(i,j))d\sigma] \quad (3.4)$$

The imaging nature of the IFTS and the lens system mean that the raw signal reaching the detector is modified by the throughput available to the system, and so $S(\sigma)$ is the signal from the radiative transfer model, multiplied by the instrument throughput as defined in equation 3.7 in the following throughput subsection. $S_{instr}(\sigma)$ is the signal from background emissions of the instrument, also multiplied by instrument throughput.

Additional factors in this equation represent several effects of the instrument model. These extra factors are: transmittance of the optics ($\tau_{optics}$), emissivity from the instrument ($\epsilon$), detector responsivity ($\Re$), and a modulation factor related to averaging over the solid angle subtended by a detector ($M$). The value $x_{mapped}(i.j)$ is the corrected OPD value for a pixel at location (i,j) as described in equation 2.72.

### Sampling Criteria

The output generated from the radiative transfer model forms the continuous spectrum $S(\sigma)$. Recalling the relationships set by equation 2.57, a vector of OPDs, $x$, is created for the interferogram, with spacing $\Delta x$ defined by equation 2.56. For quick reference, these equations combine to give the number of points necessary to satisfy the Nyquist criteria:

$$N = \frac{2L}{\Delta x} = \frac{2\sigma_{max}}{\delta\sigma} = 2L \cdot 2\sigma_{max} = 4L\sigma_{max} \quad (3.5)$$

This equation allows for an easy calculation of the number of interferogram samples required when the mirror MPD and maximum wavenumber to be measured are known. Now $x$ is a vector of length $N$.

### Off-axis Effects

Recall from equation 2.72 that the OPD varies as the cosine of the incident angle. This creates a shift in the observed wavenumber as one moves off-axis. Therefore, a correction mapping is created for all pixels used in the detector, such that the OPD for each pixel properly takes the off-axis effects into account. With the mapping in place, equation 2.41 is

applied, with the upper and lower bounds set by the range the user wishes to examine. At each point in vector $x$, and for each pixel, this integral is performed.

### Optical Geometry and Throughput Considerations

As noted in Chapter 2, the Haidinger fringes are imaged at the focus of an imaging lens onto the detector. For this section, the optics are treated as a blackbox that must meet certain criteria at the system entrance and detector planes. In the case of LIFE, the corner cubes are chosen as the location of the imaging plane, to utilize the throughput provided by the FTS. Recall that care must be taken to reduce the effects of background signal corruption. This is achieved either by cooling all components, or by introducing a cold stop element in the aft optics. LIFE makes use of a cold stop at the detector location. Therefore, the detector and cold stop limits the throughput of the system. The image at the cold stop plane is associated with the plane of the corner cube.

The decisions made for the stop aperture size and distance provide a system requirement known as the f-number (F#), and is given as

$$F\# = \frac{l}{d} \tag{3.6}$$

where $l$ is the distance and $d$ is the diameter of the opening. A proper lens design must match this definition for proper focussing to occur.

The size of the pixels is also important in determining the system throughput, which directly relates to the intensity of the signal detected; a larger throughput offers higher intensity, as more light enters the system. Throughput is calculated as the area of an element multiplied by the solid angle of that element.

$$A\Omega = (A_{pixel}\Omega) = l_{pixel}w_{pixel} \cdot \frac{\pi r_{aperture}^2}{d^2} \tag{3.7}$$

This throughput is calculated from the detector point of view but is constant for the whole optical system. Therefore, the input of the optical system has the same throughput. With a defined FOV, the size of the optical beam is determined as well with equation 3.8.

$$r_{input} = \sqrt{\frac{1}{\pi}\frac{A\Omega}{(FOV_{vertical}) \cdot (FOV_{horizontal})}} \tag{3.8}$$

This is the maximum radius of a beam at the imaging plane that can be handled by the aft optical system. If an input beam is larger than this value, scene information is lost, resulting in a smaller effective FOV than what is desired. With a beam smaller than this, the effective throughput to the system is lower than expected. Optics must be designed with this trade-off in mind, as matching these values perfectly may require highly specialized and expensive lenses.

Along with these parameters, also of need for consideration is the effects of the finite aperture, discussed in section 2.2.4. When considering the effects of a finite aperture with the optical geometry, there is a trade-off that arises in the design process. A balance is found between throughput and spectral resolution, which are inversely related; a larger throughput increases signal levels, but also the solid angle of integration, reducing the spectral resolution due to fringe averaging. A smaller solid angle requiring less averaging corresponds to a smaller throughput. These effects can be investigated with the instrument model.

#### Level 0 Output data

The interferogram generated by equation 3.4 includes both modulated and un-modulated data. The useful form of the interferogram requires only the modulated component, so the un-modulated signal portion must be removed. Equation 2.42 indicates the relationship between the modulated and un-modulated components, replacing $I_p$ with $I_{raw}$. Removing the average value as suggested in equation 2.42 results in an interferogram containing only the modulated data. At this time, the chosen apodization method is applied. The interferogram simulated here is now considered as the level 0 output expected from the LIFE instrument.

Note that the at this stage, the model has perfectly equal spacing for all samples of the interferogram. However, the interferogram is not generated with perfect spacing as described in section 2.2.4; these effects and a method of correction to obtain this spacing is described in section 6.9. For now, the perfect spacing of the model is used.

### 3.1.3 Radiometric Calibration

The retrieval of a spectrum from the level 0 data is the next step in the process. Level 1 data is considered as a spectrum representative of the scene. Taking a Fourier transform

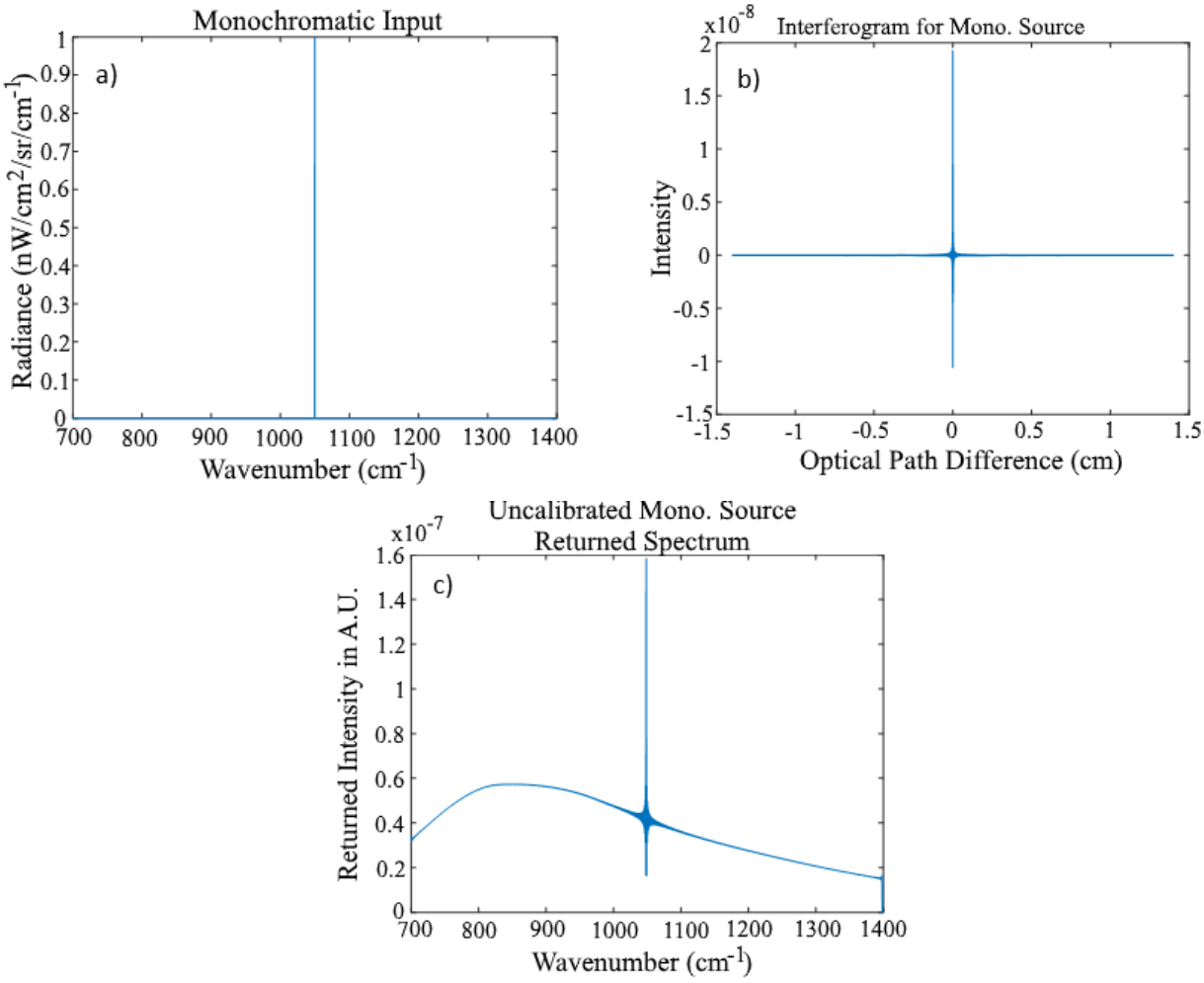


**Figure 3.6:** Monochromatic Source Simulation: a) Input Spectrum b) Interferogram generated by input and instrument factors c) Uncalibrated spectrum returned. Notice the input is recreated on top of the background signal.

of the interferogram described previously results in obtaining $S_{measured}(\sigma)$. However, this spectrum represents the scene added to the additional background emissions coming from the instrument components included in equation 3.4. Additionally, the Fourier transform leaves the recovered spectrum in arbitrary units. To obtain level 1 data then requires a calibration.

As an example of this issue is illustrated using a monochromatic spike source as an input. In figure 3.6, a monochromatic spike is used as input, and the interferogram and uncalibrated resulting spectrum are shown.

It is clear to see from figure 3.6c that the calibration step must be performed, as the

delta function of the monochromatic source is recreated on top of a curve. This curve is the Planck function for a source radiating at 298 K, the temperature that much of the instrument operates at and is the consequence of including instrument background emissions. Calibration must be applied to remove this background artifact.

This figure also indicates that the units are not representative of the scene units; the spectra from the model do not have proper radiometric units. Certain information, such as atmospheric temperature, cannot be obtained form arbitrary units, and so calibration methods must allow the conversion back to radiometric units. Also seen in the figure is the ringing and broadening of the input delta function by the ILS on the instrument.

Another major factor considered by the calibration is the correction of phase errors. Phase errors are introduced by the three additional sources described at the beginning of section 3.1.2, in addition to any noise in the system. The introduction of phase errors results in spectra that have both real and imaginary components.

The phase error introduced by these sources must be corrected to use the data collected by the instrument. Different methods have been validated, such as the statistical approach used for MIPAS-B2 [36] or the two-point calibration methods used for GLORIA [15]. The statistical approach allows the calculation of phase for each individual spectrum and is accurate regardless of thermal drift which causes differences in phase error between scans [36]. Comparatively, the two-point calibration method provides a "faster" form of calibration with less need for post-processing but requires measurements of onboard blackbodies at determined time intervals to correct for phase drift [15]. In these cases, the accuracy of returned spectra is potentially less than those obtained through statistical processing. Care needs to be taken in deciding the method and how much error is acceptable in the measurements.

LIFE makes use of the two-point calibration, requiring two blackbodies to be incorporated into the design, with the ability to choose to look at the blackbodies or the scene. This calibration requires the assumption that the system response scales linearly with temperature. The calibration uses the following equations [15] [37]:

$$g = \frac{S_h - S_c}{B_h - B_c} \text{ (Gain correction)} \tag{3.9}$$

$$O = \frac{S_c}{g} - B_c \text{ (Offset correction)} \tag{3.10}$$

$$L_{atm} = \frac{S_{atm}}{g} - O \text{ (Calibrated spectrum)} \tag{3.11}$$

where all $S$ values refer to the complex, uncalibrated spectra recovered from the interferograms, $B$ denotes the blackbody spectra and $L$ is the calibrated spectrum. The subscripts refer to the source of the various spectra; subscript $h$ is for the hot blackbody, $c$ for the cold blackbody and $atm$ for the atmosphere. Since the instrument background radiation is present in all measured $S$, the calibration removes these artifacts when performed properly. The calibration also divides the scene radiance into the real part of the complex spectra, and all noise into the imaginary part [15].

There are several points to consider when using this calibration method. The method assumes a linear response, so any non-linearity in the detector response must be appropriately characterized and corrected. Thermal drift must also be considered and requires the blackbodies to be periodically viewed during a flight to ensure that the gain and offset are being calculated properly. There are also errors in the blackbody temperatures that lead to erroneous determination of gain and offset. Finally, noise in the measurements themselves will lead to errors in gain and offset. The model aims to allow the inclusion of these errors to determine how accurate certain factors need to be, and how these errors propagate into the recovered spectra.

To model the calibration performed properly, two additional input sources are added to the simulation. These are the hot and cold blackbodies, which are set to emit at a certain temperature. For LIFE, the hot blackbody is considered to emit at 300 K, and the cold blackbody emits at 273 K.

Using the monochromatic source of figure 3.6 as the scene, figure 3.7 shows the resulting spectrum after the application of the two-point calibration.

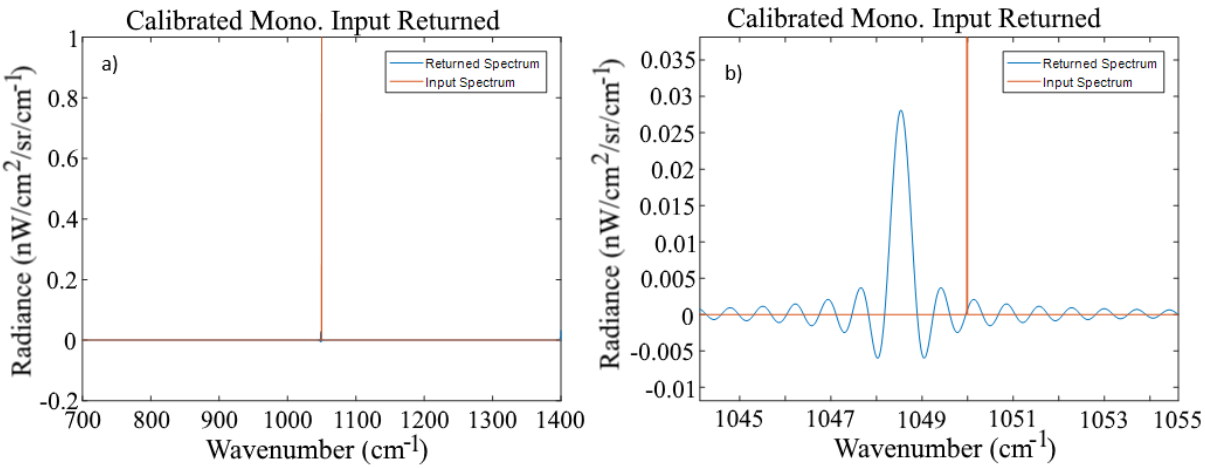


**Figure 3.7:** Monochromatic Source Simulation with calibration applied: a) full spectral range b) zoomed in to show effects of model.

From this figure, it is seen that a single line undergoes a spectral shift to lower wavenumbers (due to off-axis and averaging effects) as expected. The intensity levels of the returned signal are also greatly reduced. While it may be alarming at first glance, this reduction effect is directly related to the sampling $\delta\sigma$. With a tighter spectral sampling spacing, the returned spectra magnitudes more closely resemble the input. Recall that this is a limitation set by the MPD of the instrument, and so this reduction is exactly what is expected for an instrument such as LIFE. This figure also demonstrates the broadening and ringing effects associated with the ILS of the instrument, as described in section 2.2.4.

Another issue with the application of this calibration that exists in the case of LIFE is that the two-point calibration is at its core a method of linear interpolation. Thus, it is most accurate when the two calibration reference points frame the scene, and when the assumption of a linear relationship between those points hold. However, for LIFE the blackbodies do not frame the scene temperature, which is expected to be between 245 K and 275 K. When the scene is framed by the blackbodies, error is at a minimum, meaning that the calibration of LIFE will have errors that need to be characterized as well [38].

Finally, the calibration method applied depends on knowledge of the temperatures of the calibration sources and introduces additional dependant quantities. An error in this knowledge leads to errors in the calibration. An examination of the possible error in measurements

caused by this error is shown in figure 3.8. In this example, an error on the order of 1° C in knowledge of blackbody temperature is introduced.

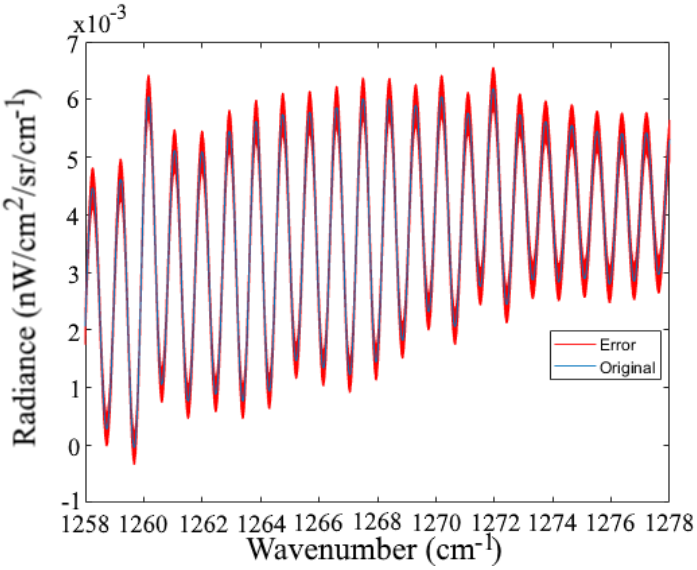


**Figure 3.8:** Example of the radiance error caused by a 1° C uncertainty in calibration method.

This figure shows that uncertainty in blackbody temperature of this order causes an uncertainty on the order of 1x10$^{-4}$ nW/cm$^2$/sr/cm$^{-1}$. This has the potential to be significant if detector noise is on a similar scale. An examination of how sensitive the instrument is to these effects is done with LIFE parameters in section 5.3.

### 3.1.4 Noise in the Model

The discussion of the model thus far has focussed only on cases where the detection of all factors is perfect. However, as discussed in the background, every measurement has fluctuations that lead to non-ideal representations of the data recovered. This section deals with the noise modelling implemented for the LIFE system in a general sense, as this modelling applies to any photoconductive detector. Noise effects need to be characterized and modelled accurately to determine how they change the system results. These are typically defined by the noise equivalent power (NEP) and noise equivalent spectral radiance (NESR) which are closely linked. NEP gives an indication of how much power needs to be incident on the detector to inarguably be from the scene and not caused by noise effects. Similarly, NESR gives

an indication of the spectral intensity required to be sure that a recovered spectral feature is from the scene and not caused by random fluctuations in measurements.

The interferogram generated by equation 3.4 has measurement units of volts, meaning that all sources of error need to have a measurable voltage effect. The detector errors very are already in volts, making their inclusion in the model easily implemented. Any given measurement has an added noise of the order $V_n$. This error is added in as a random variation of approximate magnitude $V_n$ after the unmodulated interferogram values are calculated.

The error associated with mirror position determined by the accuracy of the metrology signal knowledge is implemented within the calculation of the unmodulated interferogram. This error is directly related to the OPD value of each measurement, $x_0$. This propagates into equation 2.72, changing the values for all $x(i, j)$ for off-axis pixels. The array that stores all of these off-axis values for mirror positions and off-axis locations, $x_{mapped}$, then has an added term where the random variation of expected magnitude, $\delta x$, is added. This accurately represents the amount of error in calculated interferogram values when the knowledge of position is accurate to within a distance $\delta x$.

### 3.1.5 Noise Equivalent Power

The NEP of a system is representative of the amount of power incident on the detector to obtain a signal-to-noise ratio (SNR) of one. This means that knowledge of the NEP is directly related to the sensitivity of the detector. NEP is one of the most important parameters in the determination of how well a system operates. However, literature on the subject is occasionally inconsistent, due to there being two major ways of thinking about the NEP. Since most literature only quotes one convention, this section includes a discussion of both conventions, in the hopes of providing a reference for how the two are related.

The first way of considering the NEP is as just the power necessary to produce a signal-to-noise ratio of one. In this convention NEP is measured in watts and is a direct value for the SNR. In this convention, parameters such as sampling rate and measurement bandwidth are *included* in the calculations. That is, whichever detector is being used, the sampling rate being used and the associated bandwidth *need* to be included. When using this convention, quotes of NEP are tied specifically to a certain setup.

The second way of considering NEP is to divorce the equations from the setup being used and making a general statement about the detector. In this convention, sampling rates and measurement bandwidth are *not included* in the calculations, and discussion of NEP takes place with units of $W/\sqrt{Hz}$. This allows a discussion of the NEP for a device for a variety of set-ups and sampling rates. This convention also allows comparison of two detectors with different sampling rate capabilities. Since this NEP ignores the sampling, direct comparisons can be made.

### NEP in Watts

This convention starts with a value known as the detector normalized specific detectivity:

$$D^* = \frac{R_v (lwB_w)^{1/2}}{V_n} \tag{3.12}$$

where $R_v$ is the detector responsivity, in units of volts per watt and all others are previously defined. Combining this with the definition of NEP with units of watts:

$$NEP = \frac{A^{1/2} B_w^{1/2}}{D^*} \tag{3.13}$$

where $A$ is the detector area. Equations 3.12 and 3.13 result in

$$NEP = \frac{V_n}{R_v} \tag{3.14}$$

This ensures that, if the responsivity of the system is determined, the NEP has units of watts, and can be directly compared to the radiant power from a forward model.

### NEP in Watts per $\sqrt{\text{Hz}}$

The equation for this convention takes the form of

$$NEP = \frac{V_n}{R_v \sqrt{1/(2t_{samp})}} \tag{3.15}$$

where $t_{samp}$ is the time between interferogram samples. This can be combined with equation 2.73 to arrive at

$$NEP = \frac{V_n}{R_v \sqrt{\delta f}} \tag{3.16}$$

Equations 3.14 and 3.16 are clearly very similar, and while it seems pedantic to so explicitly define the differences between definitions, it is *vitally* important to know which NEP value is quoted when determining the effects of the noise on the system. This carries over to the determination of noise equivalent spectral radiance as well, as this value depends directly on the NEP, and also changes forms depending on the convention used.

### 3.1.6 Noise Equivalent Spectral Radiance

Noise equivalent spectral radiance (NESR) is the primary method by which an instrument is evaluated. This value is defined as the spectral radiance required to achieve a signal-to-noise ratio of one. It ties closely to the NEP of the detector, but also depends on the characteristics of the interferogram. While NEP is an indication of the amount of noise in any given measurement, NESR is an indication of the reliability of the full system in detection of spectral lines. In a given scene, any emission lines less than the NESR are not detected. This is extremely important to scientific operation, as it indicates which emission lines are useful, and is directly related to the accuracy to which atmospheric density profiles are determined for trace species.

The NESR has many forms, based on the definitions and conventions used in the system. Considering that the NESR is the primary determinant in whether an instrument is able to provide proper measurements and completes the scientific objectives, it is vital to ensure that the values and factors are consistent and correct. Like NEP, existing literature uses different convention between articles, but always has the same units in the end. It is vital to ensure that the defined terms used in a reference paper match the ones used in analysis. The primary points of potential confusion are the definition of NEP, and the definition of spectral sampling.

$$NESR = \frac{2 * NEP}{A_{pixel}\Omega\eta\delta\sigma\sqrt{Nt_{samp}}} \tag{3.17}$$

where the NEP uses the watts per square root Hertz convention, defined by equation 3.16 and $\delta\sigma$ is defined as per equation 2.57. $A_{pixel}$ is pixel area, $\Omega$ is the solid angle. $\eta = M\tau_{optics}A_{po}$ is the total system efficiency, with $M$ as the modulation efficiency term, $\tau_{optics}$ is the optical

transmission through the system, and $A_{po}$ is an apodization factor related to the apodization function used on the interferogram. $N$ is the number of samples and $t_{samp}$ is the time required for each sample.

It is not uncommon to come across literature that has a very similar form, but without the factor of 2. This is due to the use of definition spectral sampling versus spectral resolution, and the NEP convention used.

The spectral resolution is defined as $\Delta\nu$ and is the spacing at which two lines can be distinctly resolved. That is, lines separated by $\Delta\nu$ can be seen as two distinct lines. To achieve this, samples must be taken on a spacing of $\Delta\nu/2$, which is the definition used in equation 2.57. A simple replacement can be done in equation 3.17 with $\delta\sigma = \Delta\nu/2$ and the form of NESR without the factor two is found. This shows the importance of knowing if the definition being used is the spectral resolution or the spectral spacing.

Additionally, other forms of NESR can be found, such as that found in Hearn [32]:

$$NESR = \frac{4L\sigma_x}{A_0\Omega\tau_{0x}\eta_S\Re_\nu}\sqrt{\frac{2}{N}} \tag{3.18}$$

In this equation, $\sigma_x$ is the noise incident on the detector, $L$ is maximum path difference (effectively moving $\delta\sigma$ in equation 3.17 to the top, resulting in the factor 4), $\tau_{0x}$ and $\eta_S$ are equivalent to the $\eta$ term in 3.17 and detector responsivity $\Re_\nu$ appears in the denominator. This form of NESR requires that the NEP is defined in terms of Watts. Equation 3.17 and 3.18 are equivalent, but make use of different definitions, highlighting the potential for confusion amongst the literature, and the need to provide careful thought when developing and using NESR equations.

### Modelled

Modelling the NESR allows the determination of which spectral lines the instrument can detect. At any point, if an observed spectral line is below the theoretical NESR, then the instrument is not able to see that line. This effect is modelled by means of adding in the randomized error discussed earlier in this section and performing a Monte Carlo simulation.

The purpose of this type of simulation is to gather hundreds of different scans, each with a different random error. Statistical analysis is then done on these scans, and NESR values

are determined. The analysis method is discussed with the results in section 4.2.2.

With a fully developed model capable of determining the instrument response for a given set of inputs, it is possible to use these simulations to create and design an imaging FTS system. It is possible to see how changes to the scene, changes to optical elements and detector properties, and noise effects propagate through the system, and the impact of each design decision.

## 3.2 Simulated Measurement Model Validation

To validate the operation of the measurement model, a baseline comparison to GLORIA is made. This is done by using the known parameters of the GLORIA instrument in the created measurement model and comparing NESR results to the NESR obtained by KIT. The spectrometry specifications for GLORIA are given in table 3.1.

**Table 3.1:** GLORIA Instrument Specifications - spectrometry [17].

| **Requirement** | **Value** |
|---|---|
| Spectral coverage | 780-1400cm$^{-1}$ |
| Spectral sampling | <0.625 cm$^{-1}$/<0.0625 cm$^{-1}$ for DM/CM |
| Sensitivity (DM) | <(5 nW/cm$^2$/cm$^{-1}$/sr),<br>(10 nW/cm$^2$/cm$^{-1}$/sr) (threshold) |
| Sensitivity (CM) | <(15 nW/cm$^2$/cm$^{-1}$/sr),<br>(30 nW/cm$^2$/cm$^{-1}$/sr) (threshold) |
| Radiometric gain accuracy | 1%/2% |
| Spectral accuracy | 10 ppm |

Using these parameters and the detector parameters from *Sha, 2013* in the created model results in an NESR level as depicted in Figure 3.9. Figure 3.10 depicts the results of the true GLORIA instrument [13].

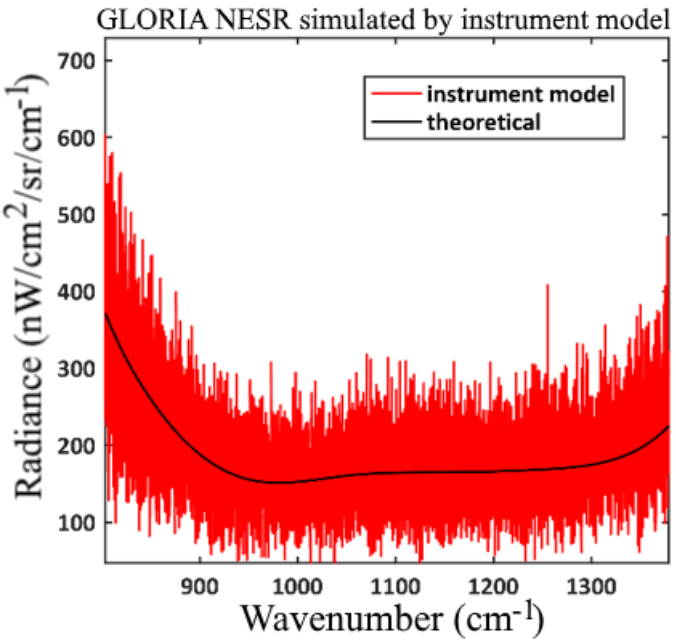


**Figure 3.9:** Theoretical and simulated NESR for GLORIA parameters in developed measurement model.

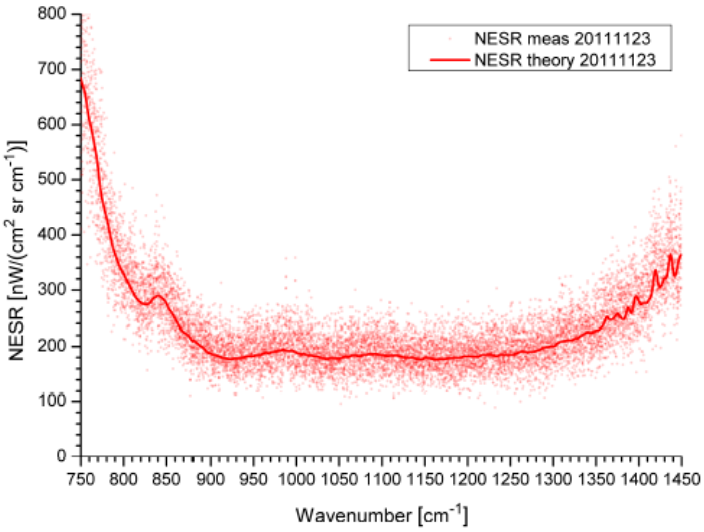


**Figure 3.10:** Measured and theoretical NESR for GLORIA operation in chemistry mode [13].

Comparing the two plots, it is seen that there is reasonable agreement in the overall shape and radiance levels. The difference between the two plots is due primarily to the estimation of the transmission curves used in GLORIA, leading to a smoother trend in the

LIFE model. The larger variation seen in the simulation is also a function of the number of simulations performed to generate the data; a larger number of runs would decrease the standard deviation, leading to a smaller spread. The agreement between the trends validates that the measurement model is functioning properly.

# Chapter 4

# LIFE Instrument Design

## 4.1 Overview

The previous chapters in this thesis have described a framework that can be used to simulate the end-to-end measurement process of a limb-imaging IR-IFTS instrument. In this chapter, this framework is utilized to design a balloon borne limb imaging IFTS. This instrument concept, called LIFE, is being developed to measure the vertical distribution of ozone, methane, nitrous oxide and water vapor in the UTLS with 1-2 ppm accuracy. It has been shown from GLORIA that this accuracy is achieved with an instrument that provides an NESR of less than or equal to 15 $nW/cm^2/sr/cm^{-1}$ [17] [21]. In Chapter 3, concepts and equations were introduced that allow the creation of a measurement simulator. These concepts are executed in MATLAB to create the simulation model and examine and inform the design of LIFE. This is referred to as the measurement model.

The preliminary conceptual model of the balloon borne prototype is shown in figure 4.1. The primary components of the instrument are the FTS interferometer, linear array MCT detector and cold stop assembly, optical imaging system, blackbody calibration system, and a platform to which all other components mount.

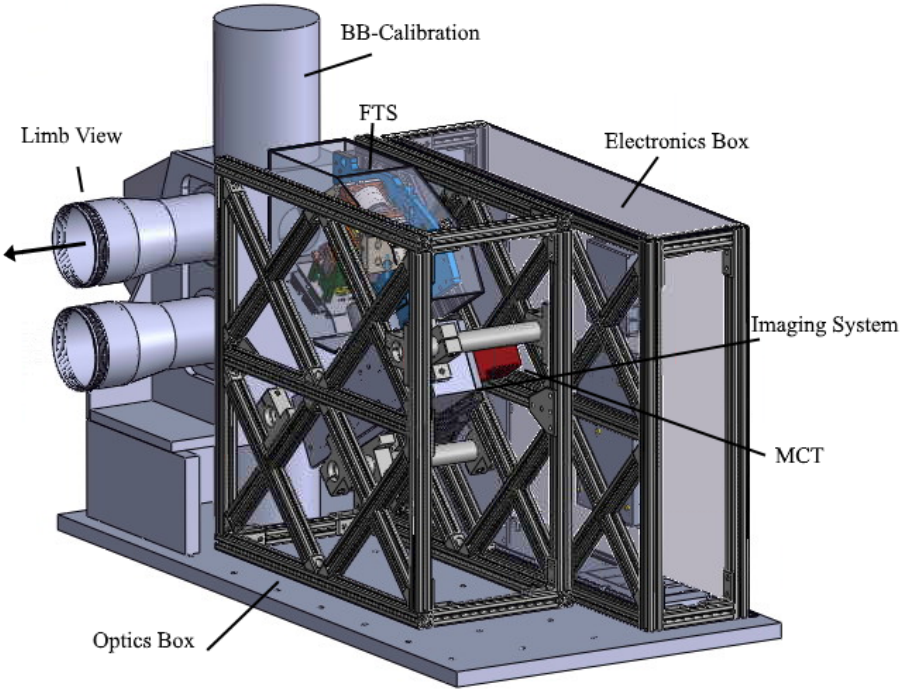


**Figure 4.1:** SolidWorks model of LIFE conceptual design.

One of the main factors that drives the design of infrared instruments is the cost of the detector and FTS system. The FAST project for LIFE had a budget of $250,000 to build the complete instrument. Therefore, one of the primary goals of the LIFE project is to obtain a lower cost instrument without sacrificing the science goals of the project. This is achieved through a collaboration with ABB Inc. This company is a world leader in the development of space borne FTS technology, which allowed off-the-shelf components to be modified for the purposes of the LIFE project. In addition, the pointing system and blackbody calibration system was salvaged from an older existing system in the lab at the University of Saskatchewan.

This chapter is separated into several sections. The first section details the practical considerations that drove the overall design of the instrument. This includes the viewing geometry of the balloon borne FTS, the array size, sampling requirement, resolution and sensitivity considerations. The remaining sections detail the design of the three primary components, the interferometer, detector, and imaging system, into a prototype instrument suitable for balloon-borne limb measurements in the infrared regime.

## 4.2 Practical Considerations

### 4.2.1 Viewing Geometry and Array Size

The balloon launch for the LIFE instrument is set to be at 40 km altitude. The range of altitudes identified for acquiring science goals is horizontal viewing at 40 km, down to a tangent altitude of 15 km. This leads to an FOV of 5.72° that needs to be focussed onto the detector array of the LIFE instrument. Recalling the discussion of section 2.2.4, each array element optimally meets the half-fringe criteria, and must not exceed the averaging of a full fringe across its surface, lest information be lost.

### 4.2.2 Sensitivity Considerations

#### NESR

The NESR is the primary metric by which the performance of the instrument is validated. Ideally, the NESR is fully simulated by the measurement model through use of the equations discussed in chapter 3, but discussion with ABB indicated that developing accurate models from the theory is difficult, and that trusting the responsivity measurements provided with the detector leads to more accurate results. Thus, the NEP used in equation 3.17 comes from real measurements made in lab. It is known that an NESR of 15 $\mathrm{nW/cm^2/sr/cm^{-1}}$ is required for science goals. If the NESR is higher than this, a number of scans will be averaged together to reduce the NESR. If $M$ scans are averaged together, this creates a reduction of $\sqrt{M}$.

#### Resolution

In section 2.2.2, it was discussed that the limited MPD made available by the interferometer causes a broadening effect in detected lines.

**Radiometric Sensitivity**

The spectra obtained in the measurement model are calibrated as per equations 3.9, 3.10 and 3.11. Recall however that this two-point calibration is not fool-proof; in providing a correction for the spectra, more dependent quantities are introduced. Knowledge of the blackbody temperatures becomes paramount in calculations, as any error here creates an error in the result spectrum as well. Error is minimized when a scene is framed by these blackbodies and must be characterized when the scene is not framed.

### 4.2.3 Sampling

Recalling section 2.2.4 of the background, much consideration must be given to the Nyquist limits, and subsequently the number of samples to be taken, and the MPD of the system. From section 1.2, science requirements for LIFE indicate that $\sigma_{max} = 1400\text{cm}^{-1}$ at least, meaning that a $\Delta x$ of no larger than $3.57 \times 10^{-4}$ cm is required by the system, by way of equation 2.56. The spacing can be smaller than this, but any larger will start to reduce the upper wavenumber limit below the accepted range.

The decision of $\Delta x$ has ramifications for the number of points, $N$, required in an interferogram as well. Recalling equation 2.57, the desired spectral sampling is directly related to the MPD available, and thus also fixes the quantity $N\Delta x = 2L$. With a maximum available spacing, this means there is also a minimum number of points required to meet science goals. This naturally leads to a minimum amount of time required to complete a scan; if a scan takes a large amount of time to complete, the data recovered may not be useful as the scene could change during the time it takes to complete. This leads to one of the first major trade-offs in the system: scans need to be short to ensure coherence in the viewed scene, but more sampling points offers more data and less potential noise.

Examination started with viewing the NESR levels using the path differences of GLORIA in each of its operation modes. GLORIA makes use of MPD values of 8 cm for chemical mode and 0.8 cm for dynamics mode. This leads to a $\delta\sigma$ of 0.0625 $\text{cm}^{-1}$ and 0.625 $\text{cm}^{-1}$ respectively.

With the NESR criteria known to be on the order of 15 $\text{nW/cm}^2/\text{cm}^{-1}/\text{sr}$, the decision

was made that GLORIA dynamics mode made a reasonable target for LIFE, to reduce the amount of time required for a scan while allowing the retrieval of trace gases within the desired accuracy of 1-2 ppm.

### 4.2.4 Self-emission

Discussion regarding radiometric errors introduced by components that contribute thermally to the signal in a non-ideal manner, in section 3.1.2, lead to the need to provide a method of reducing these stray signals. This is achieved by either cooling all components that influence the signal, thus limiting their contributions, or providing a cold stop to limit the ability of the emissions from components to be detected. For LIFE the decision was made to use a cold stop, as this allows for a simpler thermal and mechanical design. This means that only the cold stop needs to be actively cooled, and contributions from other components are to be removed with calibration techniques.

## 4.3 The Interferometer

### 4.3.1 Overview

The LIFE prototype uses a modified version of the off-the-shelf MB3000 interferometer developed by ABB Inc. This interferometer was the option available within the budget of the LIFE project, and so it set the specifications of the system. The modified MB3000 has a useable aperture of 2 cm and a maximum beam divergence of 5.75°. The MB3000 design is based off the patented ABB two-port cube corner FTS and utilizes a specifically designed Zinc Selenide (ZnSe) beamsplitter to minimize multiple reflections associated with beamsplitter self-emission. It also utilizes a patented mirror scanning system with built in laser metrology to track the mirror motion. This section details the specifications of the modified version of the MB3000 used for the LIFE prototype. How this design meets the science requirements is also discussed.

### 4.3.2 ABB MB3000

The SolidWorks representation of the MB3000 utilized by LIFE is shown in figure 4.2.

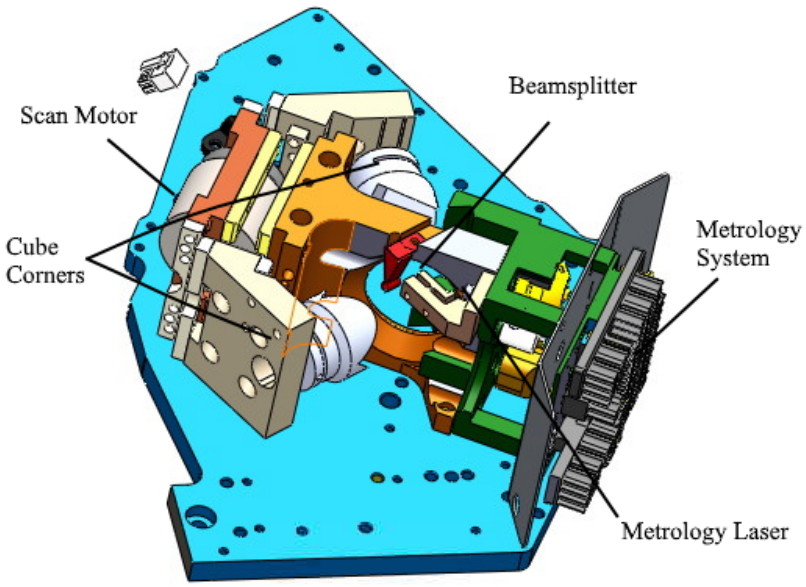


**Figure 4.2:** SolidWorks model of the ABB MB3000 interferometer.

The MB3000 interferometer, which has been modified for the purposes of LIFE, offers a unique "double pendulum" motion, where the mirror movement is controlled by a motor that moves both mirrors. Moving both mirrors together allows for a more compact design, as much less mechanical movement is required. Specifics are proprietary knowledge belonging to ABB [39] [40]. The off-the-shelf MB3000 has a maximum path difference of 1 cm, but modifications made by ABB for the LIFE project increase the MPD to 1.4 cm. By equation 2.57 this provides a spectral spacing of 0.36 $cm^{-1}$.

The expanded MPD of $L = \pm 1.4$ cm and the corresponding resolution are appropriate for science goals, as this allows LIFE to provide a spectral spacing higher than that offered by the dynamics mode of GLORIA. The interferometer has an optical scan speed of $v = 1.25$cm/s, leading to an approximate full scan time of 2.26 s with the arrangement of the mirror system providing a usable MPD of 1.4 cm. The maximum required wavenumber for the spectral

window examined by LIFE is 1400 $cm^{-1}$. Using these two values and equation 3.5, the minimum number of sample points required to meet Nyquist criteria is $N = 7840$ samples. With the time of the scan and this many samples, the detector chosen must be able to sample at least a rate of 3.4 kHz. These criteria are deemed acceptable as well, and the interferometer proposed is the one used by LIFE. The specifications for the interferometer obtained from ABB are summarized in table 4.1.

Ensuring that the measurement model accurately represents the resolution offered by the interferometer, a Dirac delta was input to the measurement model and the spectra found. Figure 4.3 zooms in on the central peak, showing that a single line is broadened to a sinc function with zero crossing matching the instrument spectral spacing.

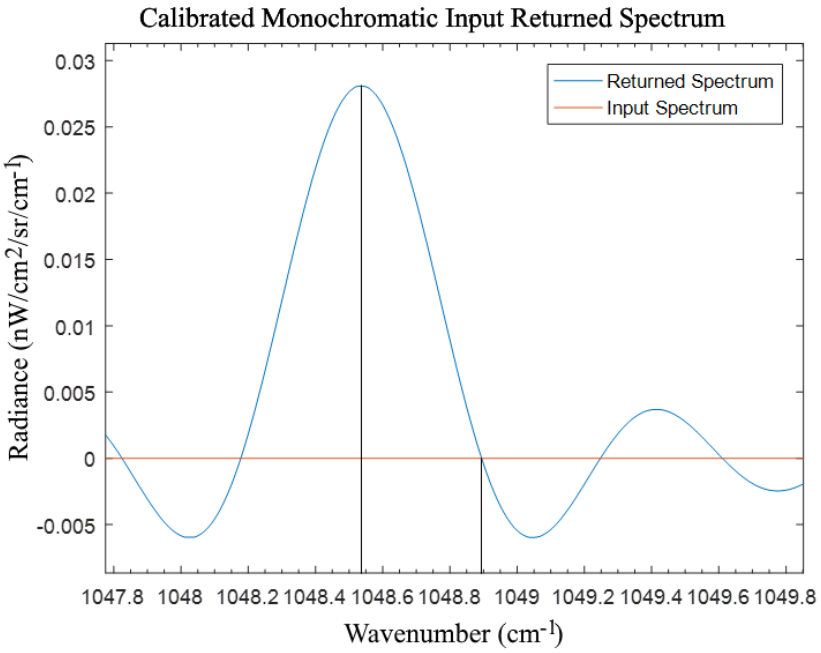


**Figure 4.3:** Zoom in on spectral broadening feature of monochromatic result.

In the figure, distance between black lines indicates the spectral sampling provided by the MPD of LIFE. The peak occurs before the mark indicating 1048.55 $cm^{-1}$, and the first zero crossing occurs at the 1048.9 $cm^{-1}$ marker, indicating a spectral spacing between 0.35 to 0.36 $cm^{-1}$. For LIFE, with an MPD of 1.4 cm, the expected spectral spacing is 0.3571 $cm^{-1}$,

indicating that the measurement model is broadening lines appropriately in the absence of apodization effects.

The maximum FOV through the interferometer is defined by the clear aperture of the cube corners and the length of the path of a ray passing through the entrance and out the exit of the interferometer. Taking the clear aperture to be 20 mm at the cube corner, the maximum possible FOV of the interferometer is 5.75°. This is slightly larger than the 5.72° FOV required for the science objectives. To minimize the self emission of the instrument, it was decided that no entrance optics are utilized for the prototype. In this case, the exit optics are designed with a cold stop assembly that provides a limiting aperture for the instrument. This aperture is imaged at the cube corner and the exit optics are designed to image the 5.72° FOV onto the detector plane.

**Table 4.1:** LIFE interferometer specifications

| **Parameter** | **Value** |
|---|---|
| Interferometer Configuration | Cube corners, 2-port |
| Angle of Incidence | 30 degrees |
| Pupil Diameter | 20 mm (25.4 mm corner cube) |
| FOV | 5.75° maximum |
| Spectral Range | 700 - 2500 $cm^{-1}$ |
| Maximum Path Difference | ±1.4 cm optical (±0.36 cm mechanical) |
| Spectral Sampling (FWHM) | 0.7$cm^{-1}$ |
| Beamsplitter Substrate Material | Zinc Selenide (ZnSe) |
| Metrology Laser | 760 nm VCSEL |
| OPD Scan Velocity | 1.25 cm/s - continuous forward/reverse scans w/ short turn around |
| OPD Speed Stability | <1 % (vibration free environment) |
| Operating Temperature Range | 15 to 35 °C |
| Operating Humidity Range | <35 % (typical) |

The beam-splitter is made of ZnSe and the corner cube mirrors are gold coated. The assumption is made that the reflection coefficient of the cube corners is close to one, such

that the beam-splitter is the primary source of self-emission and multiple reflection effects. The emissivity of the beamsplitter is about 3% and the beamsplitter and FTS system is specifically designed to minimize the self-emission effects associated with multiple reflections from the beamsplitter [39][40]. For this reason, the assumption that the primary self-emission is an unmodulated DC component that adds to the modulated signal, as described in section 3.1.2, is valid for this FTS system. The modelled net transmittance for the LIFE instrument is shown in figure 4.4.

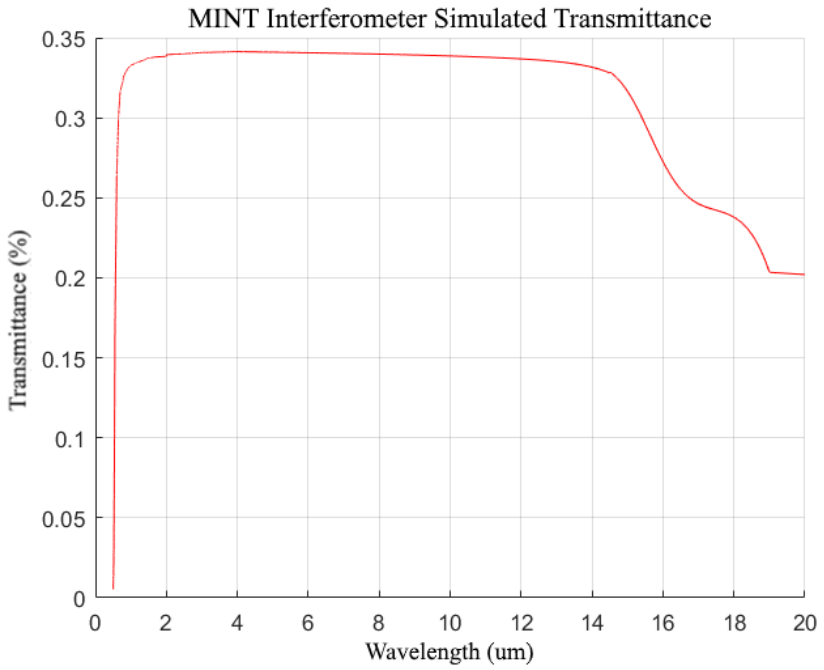


**Figure 4.4:** Transmittance curve for the MINT instrument, using the same beamsplitter material as LIFE, provided by ABB.

The range in which LIFE operates, 700 to 1400 $cm^{-1}$ in wavenumber is approximately the range 7 to 14 $\mu$m in wavelength. In this range, figure 4.4 shows a mostly flat transmittance of $\sim$ 34% with a bit of a drop toward the 14 $\mu$m edge. This means that for much of the wavenumber range $\sim$ 66% of the incident radiation is being reflected back out through the interferometer and is not incident upon the detector. This is one of the primary factors that needs to be included in the $\tau_{optics}$ variable in equation 3.4. The emissivity of the beamsplitter material is included in the measurement model as the emissivity $\epsilon$ term as well.

The modified MB3000 interferometer meets the science requirements determined by the viewing geometry and required FOV and the provided spectral spacing of 0.36 $cm^{-1}$ meets the scientific goal of matching the GLORIA dynamics mode resolution. Applicable background regarding sampling and speeds resulted in reasonable sampling speeds required for the detector. Additionally, the patented methods of ABB in the creation of the interferometer provides beneficial simplifications in the determination of self-emission from beamsplitter multiple reflections. This analysis led to the conclusion that the modified MB3000 meets the science goals.

## 4.4 The Detector

### 4.4.1 Overview

The detector module used by LIFE contains a linear array of pixels, each of which is a 0.25 mm x 0.25 mm MCT-14-0.250 PC photoconductor manufactured by Infrared Associates. These detectors are sensitive to wavelengths from 2 to 14 $\mu$m, encompassing the range required by science goals. Typically, a cooled MCT array would exceed the LIFE project budget, but through collaboration with ABB two array options were made available, a 1x8 array or a 1x16.

Recalling the need to consider off-axis effects, the elements of the chosen array ideally meet the half-fringe criteria from section 2.2.4. For the smaller array, the FOV is divided into fewer elements meaning each element views a larger portion of the scene. This gives fewer data points in the reconstruction of atmospheric profiles in the retrieval step, but also means each pixel has more incident photons from the scene detected, greatly increasing the signal-to-noise ratio. The large array gives more points of contact but has a lower signal-to-noise.

In addition to this, pixels used in this application contain only one reading for the full solid angle covered; nuances in the data in that solid angle are lost as they are averaged together. This loss of nuance is unavoidable for LIFE with the large pixels utilized, but the number of elements modifies how much data is averaged together. After a certain point, this

averaging destroys enough of the data to make measurements effectively useless.

Each element in the arrays needs to be checked to ensure the half-fringe optimization is met, and the full fringe criteria is not exceeded. Using the set of equations defined in section 2.2.4, an analysis of fringes incident across the elements of each array is done. Figure 4.5 shows a plot of these fringes as measured from the center. These trends are symmetric around the zero point.

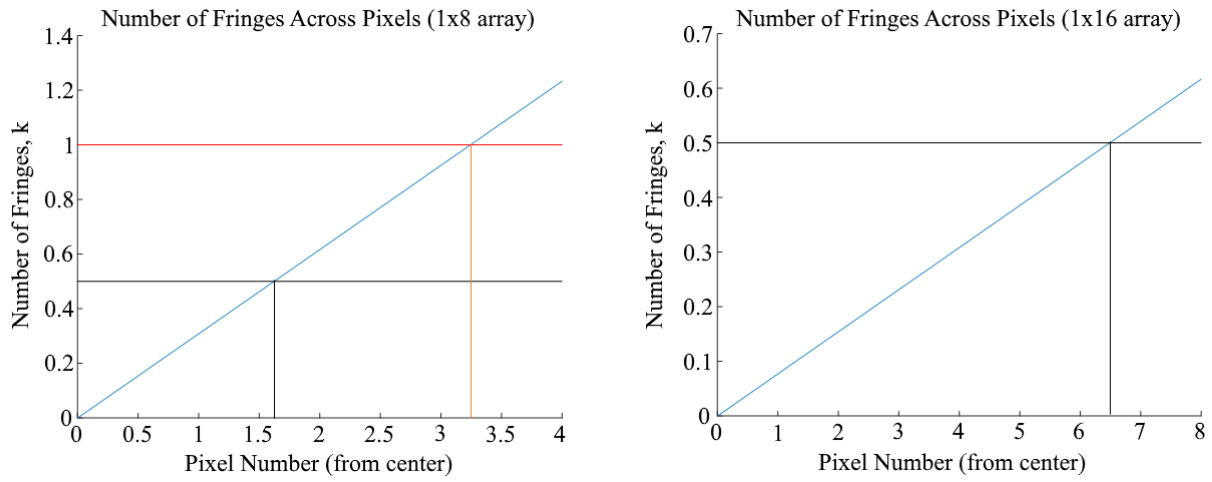


**Figure 4.5:** The number of fringes across a pixel, measured from the center out to one edge for an array that has a total of 8 elements (left) and a total of 16 elements (right). Symmetry makes analysis of one half of the array sufficient. The black reference line is for k =1/2 an intersect line for the location this occurs. Similarly, the red line shows the limit for k = 1 and the intersect pixel location.

From this figure the half-fringe criteria, shown in black, is not met by all pixels in either array. However, it is also clear that the 1x16 array does not suffer as greatly from off-axis effects as the 1x8 array. The 1x8 array only has a single pixel to either side of the center that meets the half fringe criteria; all others start to lose information, and the pixel at the farthest edge even goes beyond the acceptable range of k =1.

This analysis allowed the decision of a 1x16 linear array to be chosen as the only appropriate option for scientific objectives. This detector module is shown in figure 4.6.

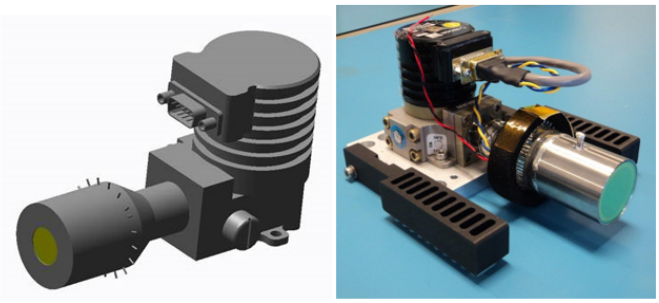

**Figure 4.6:** LIFE detector developed by ABB. SolidWorks model (left) and captured image (right).

The array is packaged into a Dewar and is cooled to 77 K with a Ricor K-508 sterling cooler. Figure 4.7 shows a schematic of the customized cold stop and Dewar system.

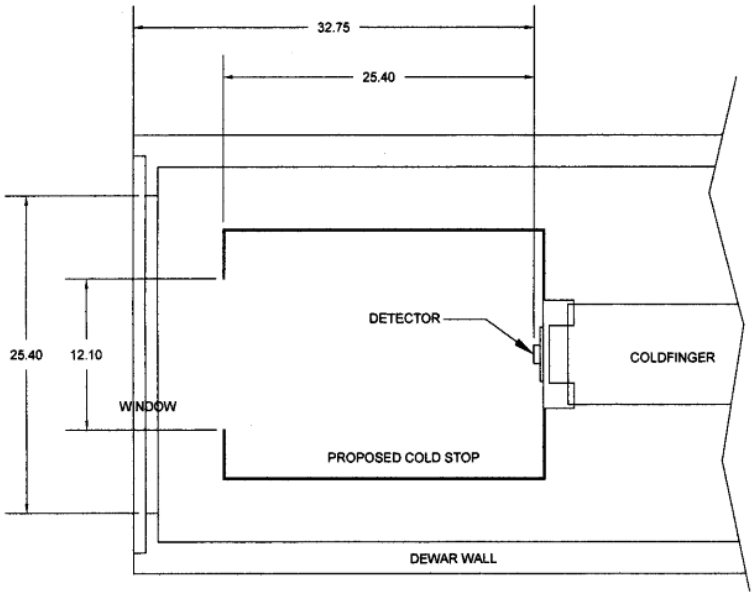


**Figure 4.7:** Mechanical drawing of LIFE cold stop system.

From this figure the distance between the stop and the detector, $l$ is 25.4 mm, and the diameter $d$ is 12.10 mm. Using equation 3.6 this gives an F# of $\sim$ 2.1 for the system. The total useful throughput to the system is found with equation 3.7 to be 0.0111 mm$^2$sr. However, proper calculation for the image placement at the corner cube requires the small area between pixels to be accounted for. The total useful length measurement for all 16

pixels is 4 mm, but from end to end the measurement is actually 4.42 mm. Dividing this into 16 parts gives the effective length for the pixel and using this value instead in equation 3.7 results in a larger throughput of 0.0136 $mm^2sr$, with only 0.0111$mm^2sr$ being utilized by the detector.

With the throughput known, and FOV for each pixel defined as $5.72°/16 \approx 0.36°$, these values are used in equation 3.8 to obtain an input beam radius of 10.47 mm. The optical system must be designed such that the image at the corner cube has a diameter of 20 mm, or radius 10 mm, meaning that the exit optics design reduces the system throughput determined here.

### 4.4.2 Acquisition System

Provided with the interferometer and detector is a customized pre-amplification and acquisition system. The system consists of two Pleora boards to read out the signal from the MCT pixels and an interface that can be utilized to synchronize the mirror motion with the MCT signals. A schematic of this electrical system is given in figure 4.8 [41].

Each Pleora board is responsible the processing of data for 8 pixels, requiring two boards for the system. The BMXS board, part of the OEM kit, is responsible diagnostics and synchronization. This board is responsible for providing timing data to the Pleora boards, allowing image timing to be matched to OPD timing data. This is necessary to make a proper mapping of OPD to MCT image signals. Proper synchronization of these signals is to be done in the future.

The acquisition cards trigger on the falling edge of a specific signal, and then performs a 177,000-sample acquisition. This data is saved in a 24-bit, 160 by 8851-pixel BGR image. The first line is a header, and the other lines contain the data. To obtain the interferograms for analysis, a program is written to unpack and re-arrange this data.

Recall that the Nyquist criteria is 7840 samples for the spectrum to be fully defined within the range of the science goals. This acquisition system provides far more points than this requirement, primarily for the purposes of synchronization with mirror motion. Recall in section 3.1.2 that perfect spacing is assumed for the equations used. In reality, this is only applicable if an accurate mapping of OPD to acquisitions is created. A larger number of

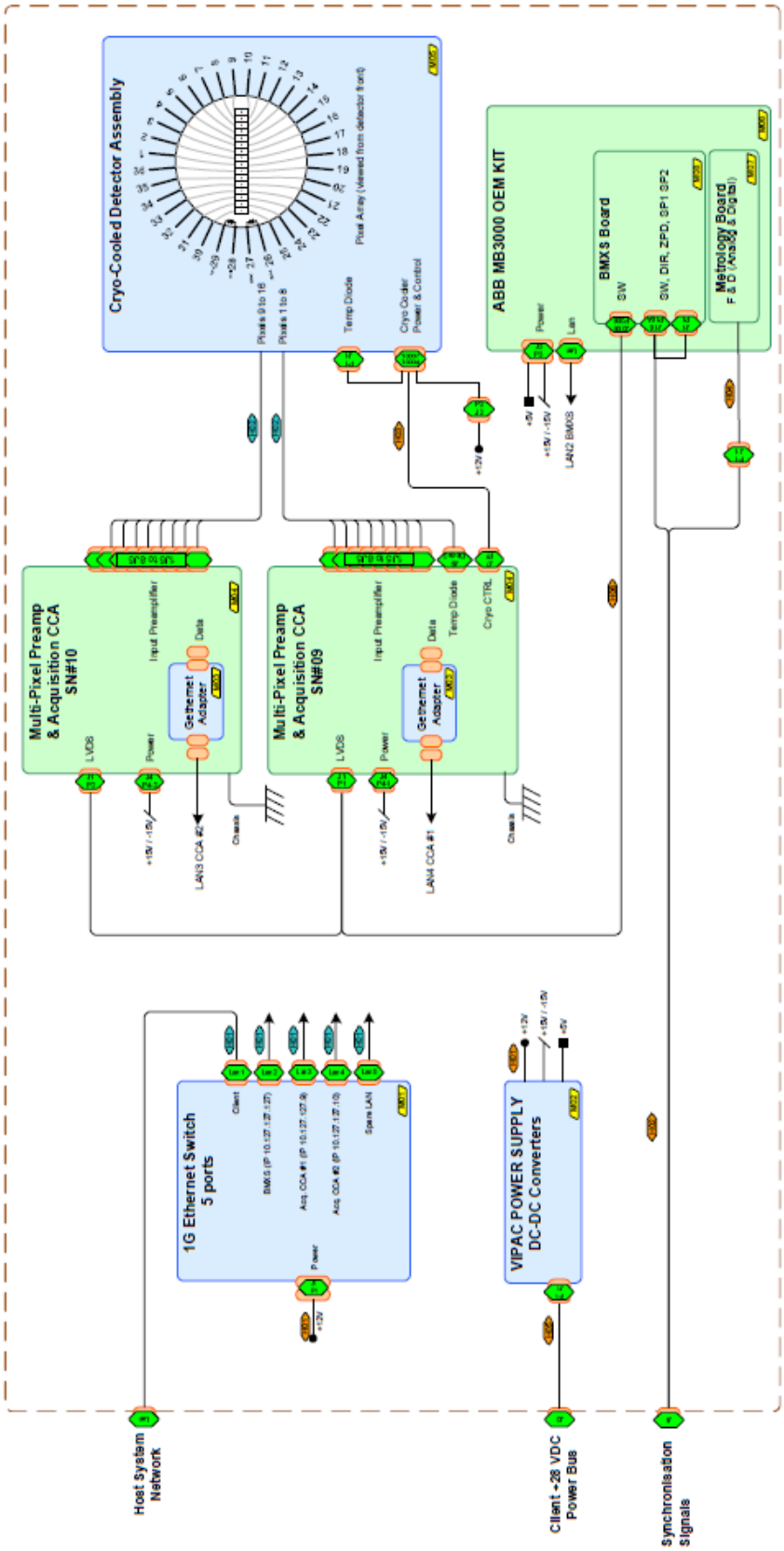


**Figure 4.8:** LIFE acquisition system electrical layout.

acquisitions allows more accurate mapping to be created through the methods of uniform time sampling.

### 4.4.3 Responsivity

The response of the MCT pixels was characterized by the manufacturer, Infrared Associates, prior to integration with the LIFE acquisition system. The dependence of the response on wavenumber for a single pixel is recreated from this information in figure 4.9. The pixel shows good response in the target wavenumber range with 60% in the 7 - 14 $\mu$m range. For these tests the pixels were operated in constant current mode with a 500K blackbody. The associated peak response (in V/W) of a single pixel as well as the NEP and detectivity are shown in table 4.2.

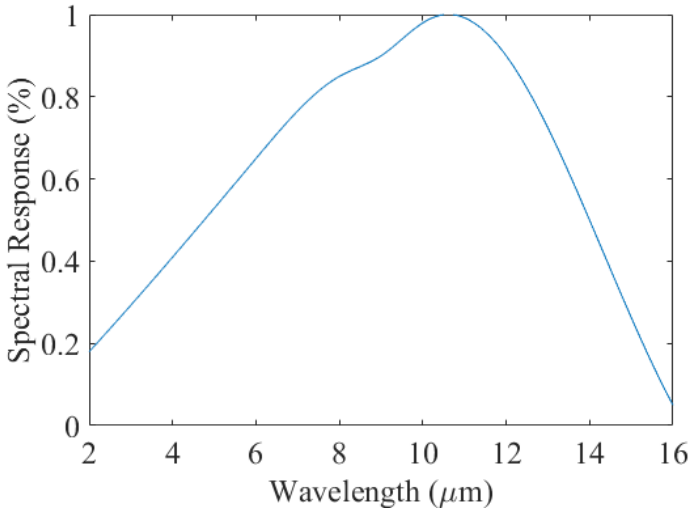


**Figure 4.9:** Responsivity curve for one of the pixels in the MCT linear array.

Note that the quoted NEP values use the definition per $\sqrt{Hz}$, and require the multiplication by the frequency to obtain the usable NEP. The dominant source of noise in the detector when operating in this mode is detector noise, indicating that the system is not photon limited regarding noise.

For LIFE and the detector used, it was advised that the methods and formulae discussed in section 2.4 are extremely difficult to model correctly, and that lab measurements are a far

**Table 4.2:** Detector test data for MCT pixel in constant current mode

| Resistance 298K | Current (mA) | Voltage (mV) | Resistance 77K | Responsivity (Peak V/W) | NEP (nV RMS/Hz$^{1/2}$) | |
|---|---|---|---|---|---|---|
| | | | | | 1khz | 10 kHz |
| 15.6 | 8.0 | 625 | 78.1 | 53977 | 59.32 | 42.43 |
| | 6.0 | 431 | 71.8 | 74617 | 42.37 | 30.37 |
| | 4.0 | 246 | 61.5 | 38459 | 22.60 | 17.60 |

more reliable way of determining the NEP. As such, further testing and lab characterization is required to determine the proper NEP values at the sampling rate, bias voltage, and offset current used for LIFE.

## 4.5 The Optical System

### 4.5.1 Overview

As noted in section 4.3, the prototype LIFE instrument does not utilize entrance optics. Instead, the collimated light from the limb enters the FTS itself. The exit optics are designed to capture this light and form an image of the limb conjugate to the Haidinger fringes at the detector. This provides a one-to-one mapping of incident angle through the interferometer to position on the linear array. However, the MCT cold stop limits the throughput of the instrument.

As mentioned in section 4.4, the MCT cold stop defines an F# of 2.1 for the system. Additionally, the cold stop is imaged at the cube corner to minimize extraneous light from instrument components. The clear aperture of the cube corners is 20 mm, thus the cold stop images at the plane of the cube corner must be chosen to be 20 mm. This ensure that the only radiation arriving at the detector is due to the optical components between the detector and FTS. All lens components are constructed from ZnSe and Germanium to minimize the self-emission. This section details the design of the LIFE optical system based on these constraints.

### 4.5.2 Optical Design

The design of the prototype LIFE optical system was performed with the CODE V optical design software. The design is based on a preliminary two lens design provided by ABB. This design was optimized to match the requirements of the system.

The optimization is performed by allowing the lens curvatures to change, as well as the distance between them. The distance between the front of the first lens and the corner cube needed to be fixed to a minimum distance that ensures the lens did not intersect with interferometer parts. Similarly, the distance between the back of the second lens and the window of the detector module is fixed to a length that is reasonable to work with such that the two do not collide and can be adjusted in lab.

The optical elements considered are the corner cube as the "entrance aperture", a front lens made of ZnSe, a back lens of Germanium (Ge) and the detector module. The module has a window made of ZnSe and contains the cold stop between the window and detector. Figure 4.10 shows the optimized optical system as designed in CODE-V.

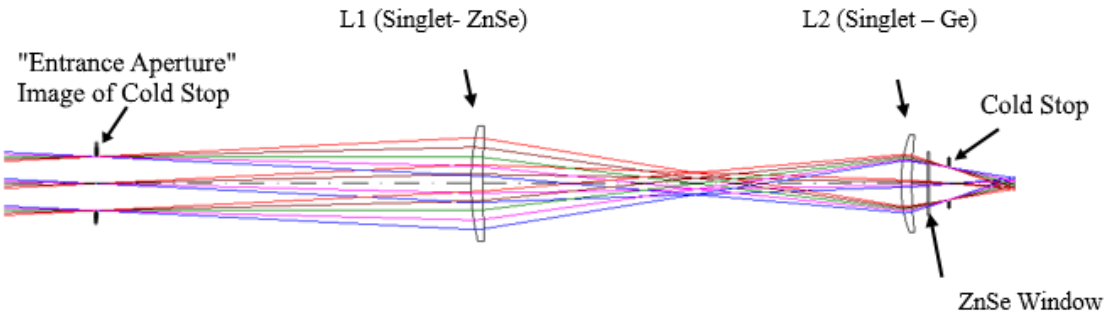


**Figure 4.10:** LIFE exit optics ray trace from CODE-V.

The primary parameter for this optimization is the focusing and spot size of the rays incident upon the pixels to ensure the limb is imaged conjugate to the Haidinger interference fringes and to ensure no cross-talk between vertical bins. These criteria require the spot size to be smaller than the pixel size. The nature of optical components causes different wavelengths to trace differently through the system; an optimization for 7 $\mu$m (1400 wavenumber) is not

well optimized for light at 14 $\mu$m (700 wavenumber). Thus, the optimization is chosen roughly in the center of the desired range and knowing that the focusing of light at the edges of the wavelength range are not optimized. Therefore, the optimization is performed at 10 $\mu$m.

Off-axis pixels also suffer adverse effects, as two lens systems focus more efficiently at the point where the optical axis and imaging plane intersect than it does at any other point on the imaging plane. These adverse effects include aberrations, departures from ideal conditions [42]. Of primary concern for this design are the phenomena of vignetting and coma aberrations. Vignetting is the phenomenon where off-axis rays do not pass through the lens system properly, leading to a faded or smeared image toward the edges of a detector [42]. This vignetting effect is significant for the pixels farthest from the optical axis. Coma is the description of how rays do not focus properly on off-axis points due to the shape of lenses [42]. These effects are examined by way of a spot diagram, which shows how the rays specified in the system spread at locations on the imaging plane. Figure 4.11 shows the spot diagram for the LIFE system at 7 $\mu$m and 13 $\mu$m, the latter being the largest wavelength CODE-V is capable of producing.

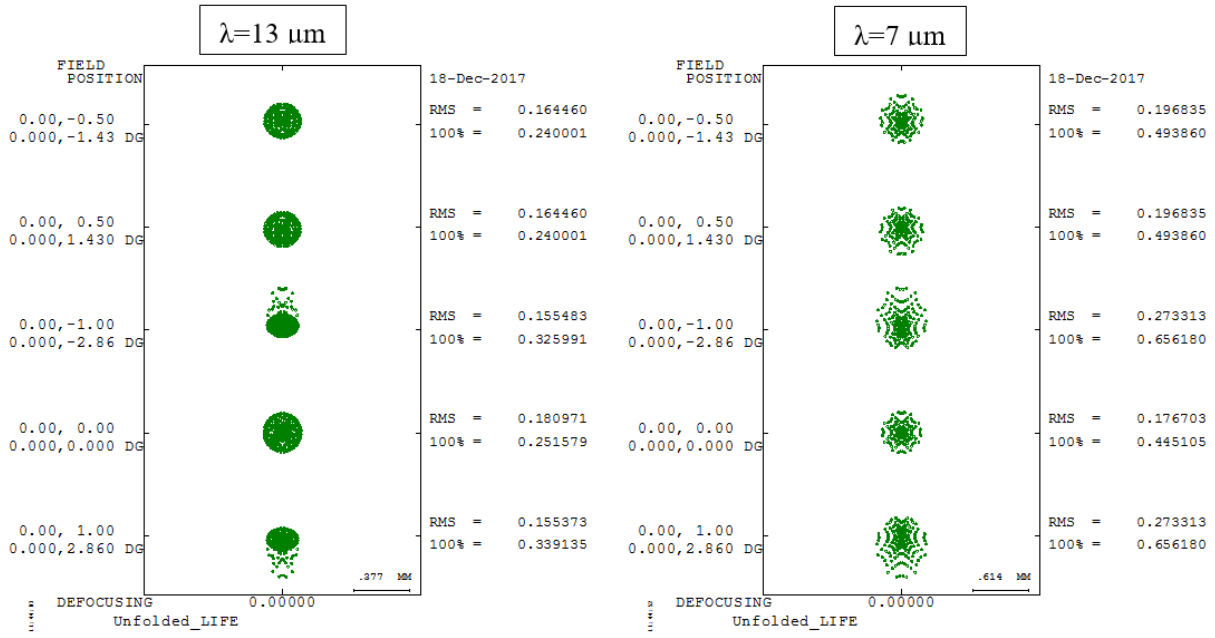


**Figure 4.11:** Two LIFE exit optics spot diagrams, for 7 and 13 $\mu$m. Each diagram shows spot sizes for the on-axis location and four off-axis locations.

The RMS values shown to the right of each image shows the vertical distribution length of the spot diagram. For 13$\mu$m, on axis spot size is 0.18 mm, and at the edge of the field of view $\pm 2.86^{\circ}$, the spot size is 0.16 mm. Each of these spot sizes is less than the size of the detector, 0.25mm x 0.25 mm. Variation and vignetting effects are minimized since all rays are still focussed onto the detector area. For 7 $\mu$m, the on-axis spot size is 0.18 mm, and the edges have spot size of 0.27 mm. This is an indication that vignetting effects will be seen by the edge pixels. Reducing the spot size further requires a more complex system; a third lens could be added, or the existing lenses could be manufactured to have aspherical surfaces. However, both options greatly increase the cost of the system, and so the minor amounts of vignetting on the elements at the edge of the array are deemed acceptable compared to increased cost.

The lens prescription data was taken from CODE-V and sent to BMV Optical Technologies to manufacture lenses that met the specifications. Table 4.3 shows the specifications of the two lenses, and figures 4.12 and 4.13 show the transmission curves for the two lenses, adapted from the lens report received from BMV Optical [43]. These transmission curves are entered into the measurement model, as part of the term $\tau_{optics}$ in equation 3.4.

**Table 4.3:** Lens Specifications

| | Lens 1 | Lens 2 |
|---|---|---|
| Material | ZnSe | Ge |
| Size | 40mm ($\pm$ 0.1mm) | 30mm ($\pm$ 0.1mm) |
| Center Thickness | 4.44mm ($\pm$ 0.1mm) | 4.04 ($\pm$ 0.1mm) |
| R1 | 91.94mm CX | 54.43mm CX |
| R2 | 434.33mm CC | 164.36mm CC |
| Irregularity | 1 wave @ 633nm | 1 wave @ 633nm |
| S-D | 60-40 | 60-40 |
| Chamfer | 0.25mm | 0.25mm |
| Coating | AR for 7-14$\mu$m both sides | AR for 7-14$\mu$m both sides |

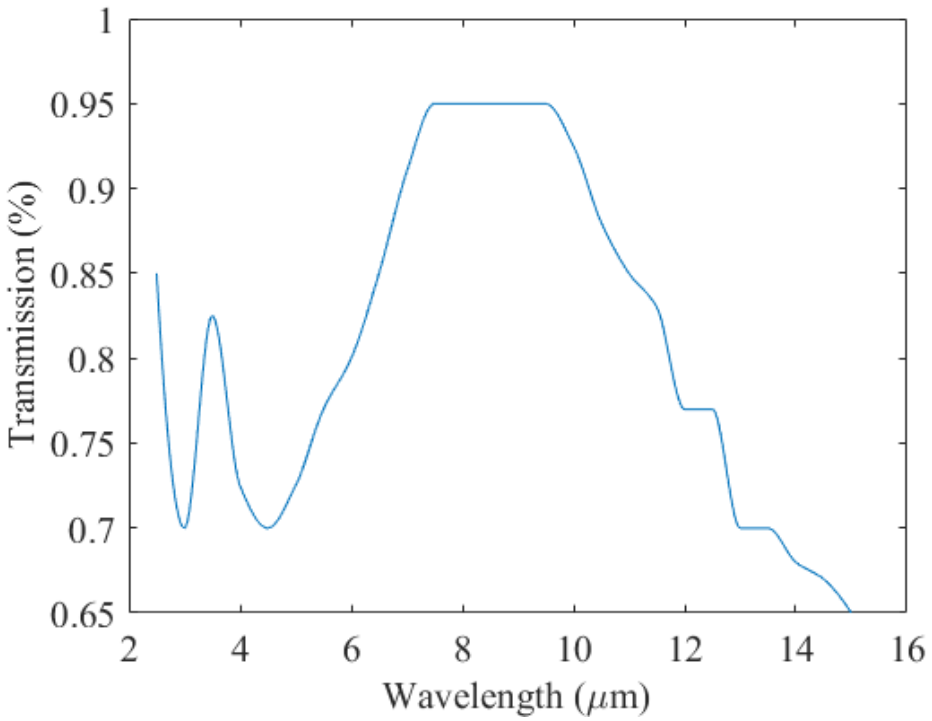


**Figure 4.12:** Transmission curve for the ZnSe lens used by LIFE, recreated in MATLAB.

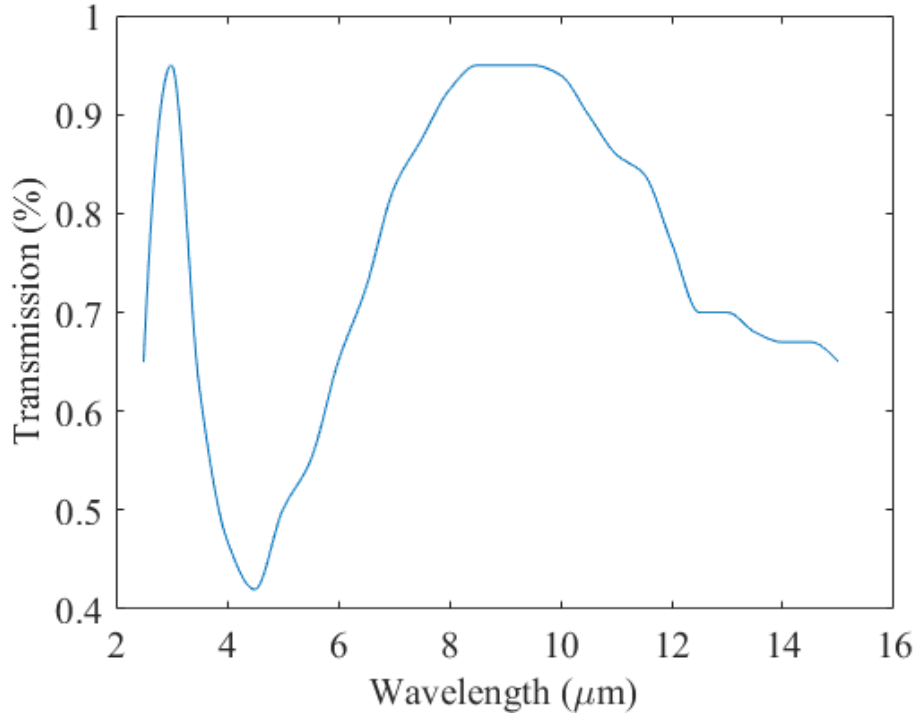


**Figure 4.13:** Transmission curve for the Ge lens used by LIFE, recreated in MATLAB.

With the transmission of all components known, the full transmittance of the LIFE instrument is found by multiplying all transmission curves together. Figure 4.14 shows the transmittance through the lenses, beamsplitter, and entrance window.

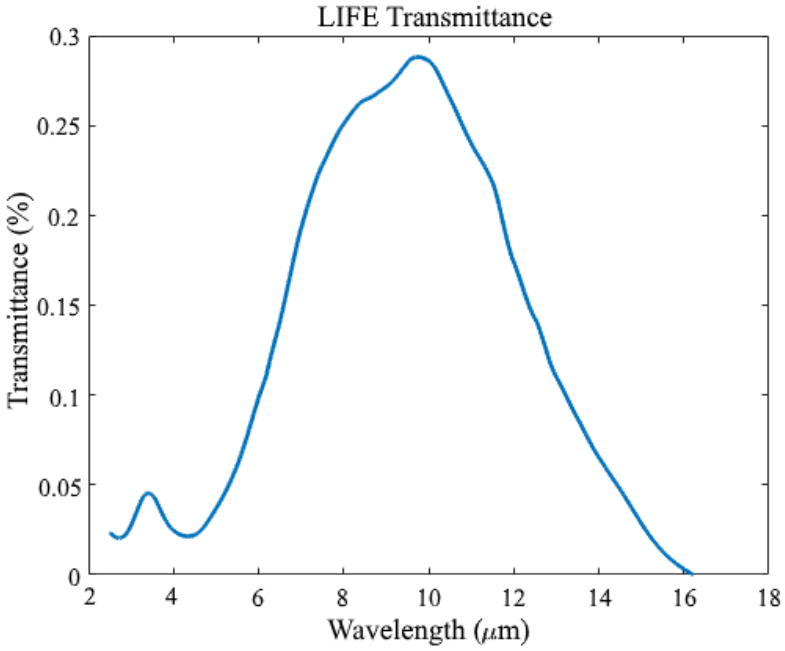


**Figure 4.14:** Full transmittance of the LIFE instrument.

### 4.5.3 Off-axis Wavenumber Shift

The primary cause of the spectral shift observed is the change in OPD for off-axis pixels, with another slight effect coming from the averaging of fringes over the pixel [32]. Recalling equation 2.72, this OPD change can be directly related to the spectral shift through the equation

$$\sigma_{i,j} = \sigma_0 \cos(\alpha_{i,j}) \tag{4.1}$$

with $\sigma$ representing wavenumber, $i$ and $j$ represent pixel location and $\alpha$ is the off-axis angle to that location. Thus, the value given by the measurement model is $\sigma_{i,j}$ and the true value that needs to be returned is $\sigma_0$. Assuming LIFE instrument parameters, the expected off-axis dependence $\sigma/\sigma_0 = \cos(\alpha_{i,j})$ is shown in Figure 4.15.

This shift needs to be corrected during data processing to properly interpret the measurements. A calibration such as this can be performed using a gas cell with many distinct spectral lines in the range of interest. A simple rearrangement of equation 4.1 indicates that division of obtained wavenumbers for a given pixel by $\cos(\alpha_{i,j})$ returns the true wavenumber.

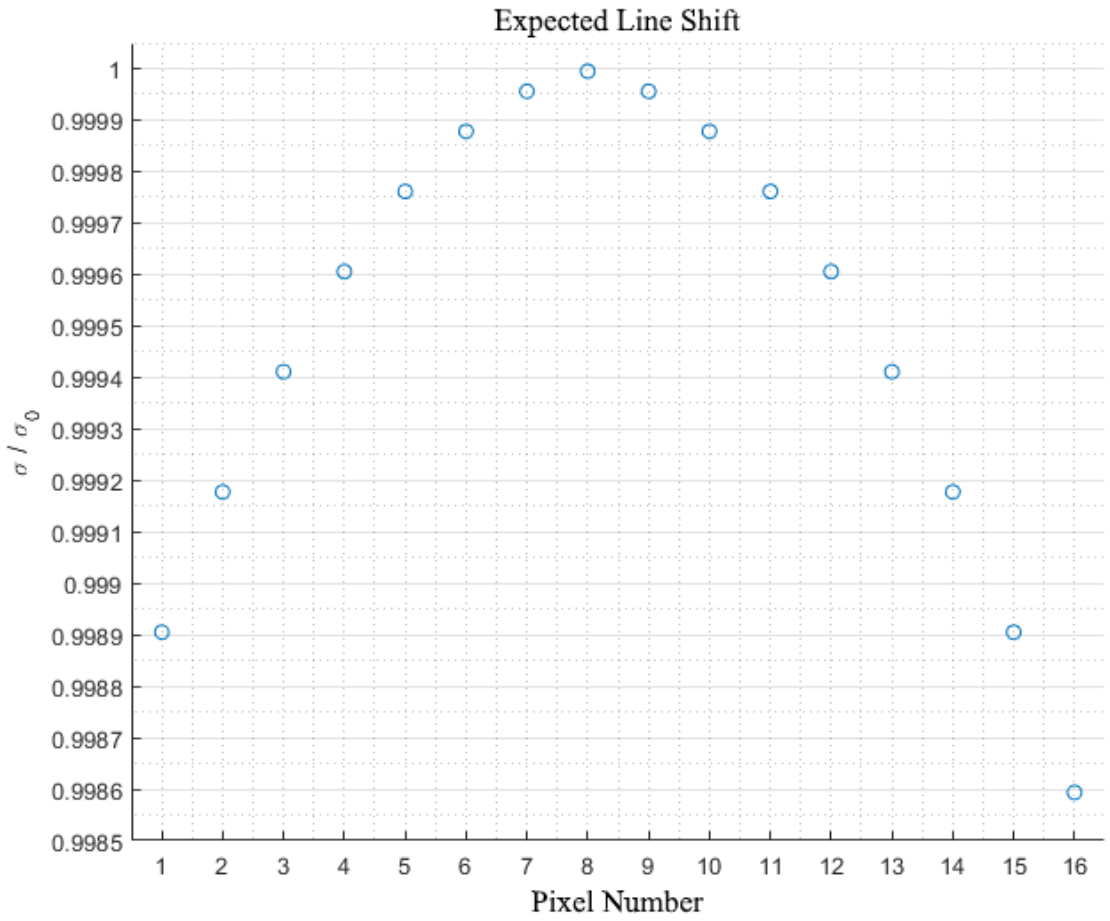


**Figure 4.15:** Expected line shift as a fraction of obtained over actual for pixels in the array.

This correction does not account for the shift caused by averaging but gives a good approximation from a modelling perspective. In practice, this calibration is more complex and requires detailed characterization in the lab. Figure 4.16 shows the input and calibrated returned spectrum as before and adds the line result when the equation 4.1 line position correction is used.

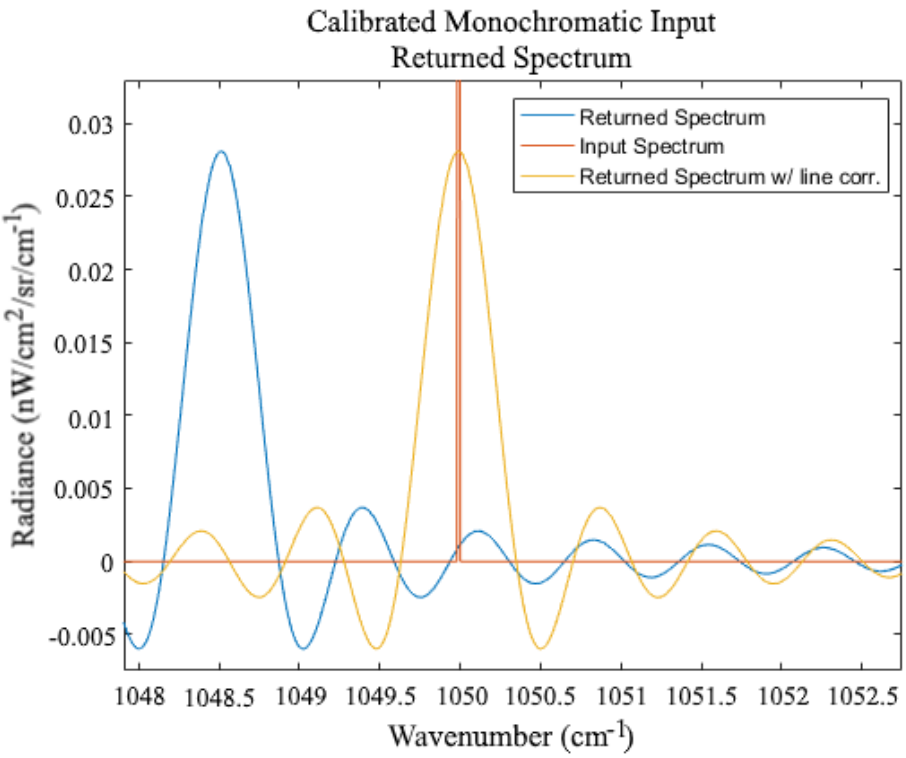


**Figure 4.16:** Line correction applied to the blue curve to obtain the yellow curve. The peak of the yellow curve is much closer to the monochromatic line used as an input.

The agreement between the peak position of the yellow curve and the input shows that the line correction is a good estimate. Since averaging effects are ignored by the measurement model, real measurements will not be fully corrected by this method. It is for this reason that a more complex, lab-based characterization and correction is required. By using a blackbody and $N_2O$ gas cell, additional scaling factors not covered by the measurement model can be determined experimentally. This characterization also allows for an accurate accounting of deviations in path difference, which the idealized instrument model does not account for.

## 4.6 The Blackbody Calibration System

The calibration unit utilized by LIFE is a legacy pointing and blackbody system previously used by the University of Saskatchewan. This system, depicted in figure 4.17, consists of a pointing mirror on a rotating motor that facilitates viewing a hot, warm, or cold blackbody, or through a baffle aimed at the atmospheric scene [44].

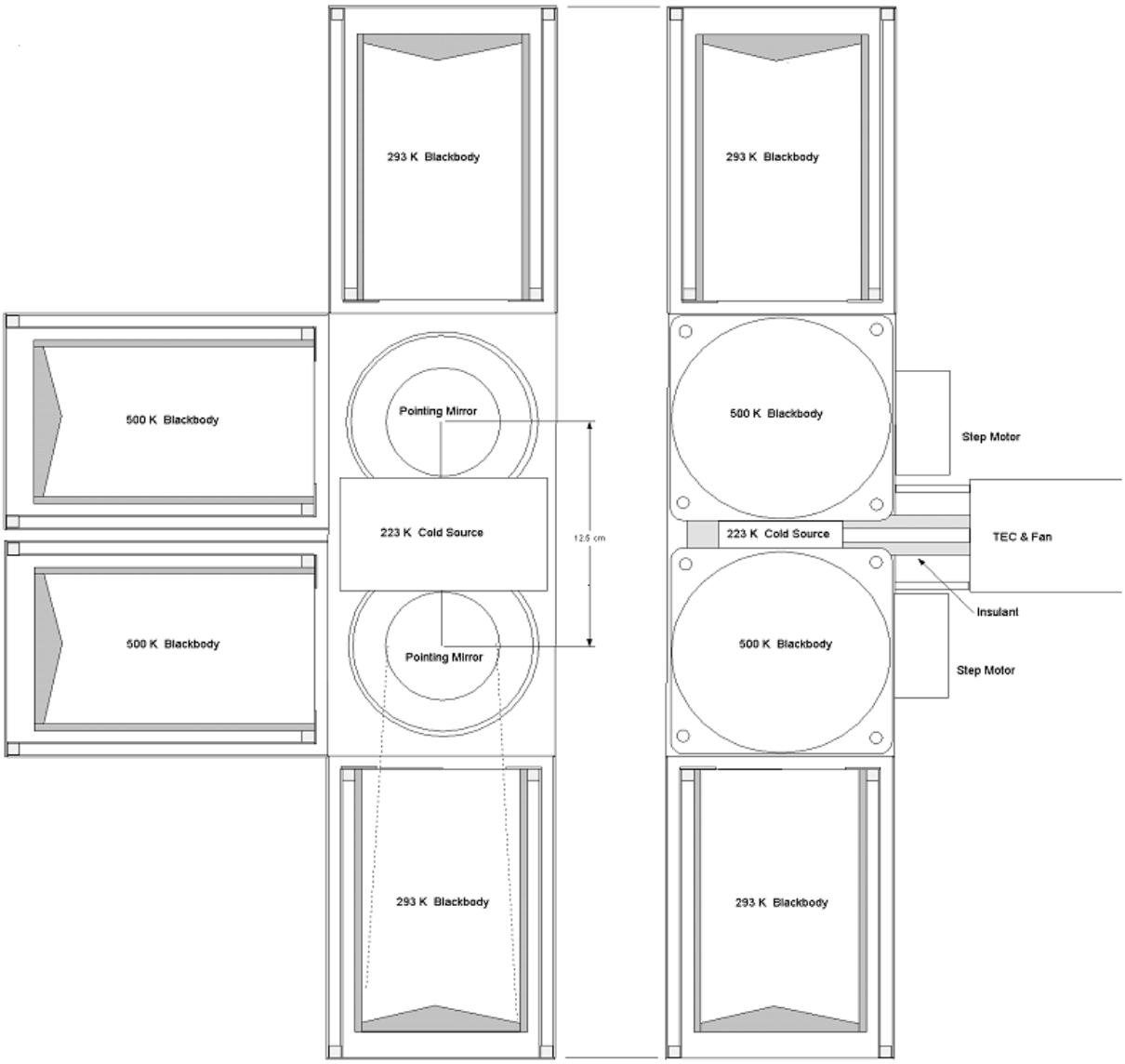


**Figure 4.17:** The pointing system and blackbody calibration sources for the LIFE version 1.

The "hot" and "warm" sources used in this design were intended to operate at 500 K (227°) and 293 K (20°) respectively, but aside from operating temperature are identical [44]. The maximum error in the temperature reading is 0.5° based on existing calibration reports [44]. It was determined that these blackbodies can operate in an appropriate range for use with LIFE. The emissivity of these blackbody sources in the thermal regime is greater than 0.995 [44]. Additionally, there is a cold blackbody source, cooled by way of a thermoelectric

cooler. This source has an emissivity of 0.98. [44].

For LIFE, one blackbody is meant to operate at 273 K (0°), and the other at room temperature 298 K (25°). This leads to the conclusion that during flight where LIFE is in a cold environment, the "cold" source must be one of the heaters, heating the source from ambient to zero. In the lab, however, the cold source must be used for the zero, being cooled from room temperature.

Since this system was not originally designed to work with LIFE, care needed to be taken to ensure that the systems integrate properly, one of the primary considerations being that the blackbody system does not limit the FOV of the instrument. Figure 4.18 shows the geometry used in determining the distance between the existing blackbody system and the interferometer.

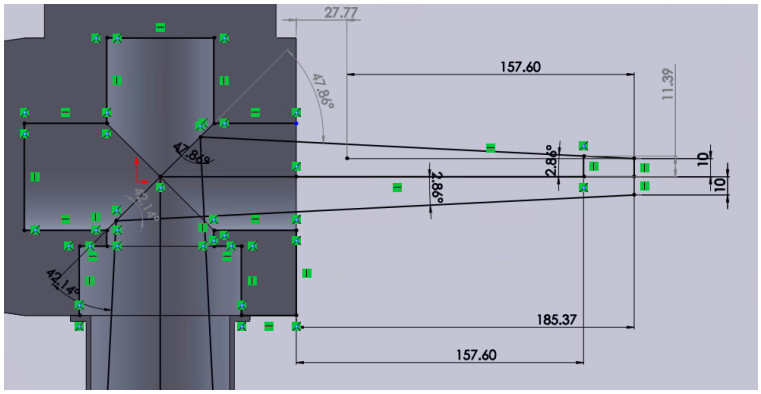


**Figure 4.18:** Solidworks diagram used to determine the clipping distances.

In this diagram, the maximum distance for which no clipping of the optical beam occurs is shown. With a combination of in-lab measurements and CAD modelling, it was determined that at any distance between the corner cube aperture and the front of the blackbody system greater than 185.37 mm would cause the beam to clip, introducing a source other than the blackbodies or scene into the measurement. Recalling that the cold stop plane is projected to the corner cube, the maximum allowable distance is between the displaced corner cube and blackbody system. Measuring distance in the CAD model between the corner cube and the edge of the interferometer and allowing for the corner cube displacement results in 157.60 mm. This means that the maximum allowable gap between the edge of the interferometer

and the blackbody assembly is 27.77 mm. Any farther away, and the beam clips. This is a critical parameter in the mechanical design of LIFE when it enters the flight model design phase.

## 4.7 Summary

The development of the preliminary conceptual model consists of design decisions meant to procure components that meet the LIFE science goals. A modified version of the MB3000 interferometer developed by ABB is chosen for the 0.36 $cm^{-1}$ spectral spacing provided as well as the allowable FOV of 5.75° exceeding the required 5.72° for science goals.

The detector chosen is an MCT linear 1x16 array sensitive in the wavenumber range of interest and is mounted in a cooler with aperture appropriately matched to the FTS. Additionally, the system includes Pleora boards allowing the collection of critical timing data.

The optical system between the detector and FTS is designed to maximize system throughput and minimize spot size at the detector to less than the pixel size. This optimization minimizes effects associated with aberrations and vignetting. The system is a two-lens design optimized with CODE V optical design software.

The blackbody calibration system utilized in the LIFE project is salvaged from a previous system at the University of Saskatchewan and requires special consideration in the mechanical design to ensure proper integration and that the FOV of the detector does not clip and introduce errors.

# Chapter 5

# LIFE Measurement Simulations

The LIFE measurement simulation model is now fully defined, and an end-to-end analysis of instrument performance is done. The instrument design described in Chapter 4 chapters is modelled using the considerations of Chapter 2 and Chapter 3, and the measurements from a stratospheric balloon use the framework described in Chapter 3.

The model takes as input a series of representative atmospheric profiles and populates the simulated atmosphere as designed by the parameters of the radiative transfer model, discussed in sections 2.1.2 and 2.1.3. Along each of the defined LOS of the system, a radiance in units of $\mathrm{nW/cm^2/cm^{-1}/sr}$ is generated and multiplied by the system defined throughput (area times solid angle) to create a flux, in watts, that is representative of the incident radiance upon the instrument. This value is used in equation 3.4 as $S(\sigma)$. Similarly, the Planck function is used to determine radiance of background and blackbody sources, and flux from each of these is found by multiplication with the system throughput.

These flux values are used to develop an interferogram, by calculating the integral defined by equation 3.4 at each location specified by the OPD, over the range 700 to 1400 $\mathrm{cm^{-1}}$. The units of the interferogram are in volts, multiplied by some gain and offset factor unique to the pixel; the raw values themselves are therefore arbitrary. Taking a Fourier transform of this interferogram leads to an uncalibrated spectrum in arbitrary units, with phase errors introduced by noise and other effects described in section 3.1.3.

Next, the radiometric calibration is simulated by generating interferograms for the blackbody sources. For LIFE, two sources are utilized to facilitate the two-point correction described in section 3.1.3. After the application of equations 3.9, 3.10 and 3.11, a representative spectrum that has been radiometrically calibrated is obtained.

To analyze the performance of the system, each step of the process has expected error

added based on the discussions of Chapters 2 and 3. A cumulative effect on the NESR for each source is done. In the NESR analysis, each of the sources are additive, so including all error sources and viewing the NESR is equivalent to analyzing the NESR of each source and viewing their combined effect.

A flow diagram of this process is shown in figure 5.1

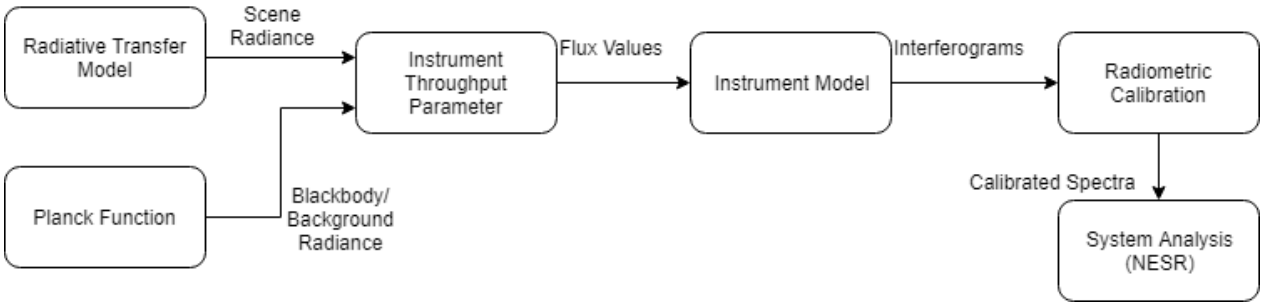


**Figure 5.1:** End-to-end LIFE simulation flowchart.

The NESR is the primary metric by which the model is judged. The sensitivity demonstrated by GLORIA, 15 nW/cm$^2$/cm$^{-1}$/sr, is the benchmark that LIFE aims to match. If the sensitivity is larger than this, techniques such as averaging the results of scans together can be used to increase signal to noise ratios and lower the scene NESR at the cost of temporal degradation.

## 5.1 Model Configuration

In this simulation, LIFE is placed in the simulated atmosphere at an altitude of 40 km and given a 5.72° FOV, consistent with the anticipated balloon flight conditions. The atmospheric pressure and temperature profiles are provided by a standard MSIS90 atmospheric model, and individual trace gas profiles for the target species are created from MIPAS observation data. The wavenumber range is set from 700 to 1400 cm$^{-1}$. The instrument is assumed to operate at roughly room temperature, using a value of 298 K for calculation of instrument self emission. The scene temperatures are expected to range from 240 K to 275 K. The blackbody calibration temperatures are set to 273 K and 300 K. Refer to section 3.1.3 for a discussion of the effects of calibration points that do not frame the scene.

## 5.2 Data Processing

For purposes of this end-to-end simulation, all images are made from data related to pixel 14, which corresponds to the detector element viewing a LOS with tangent altitude 15 km. The scene spectrum input to this pixel is given in figure 5.2

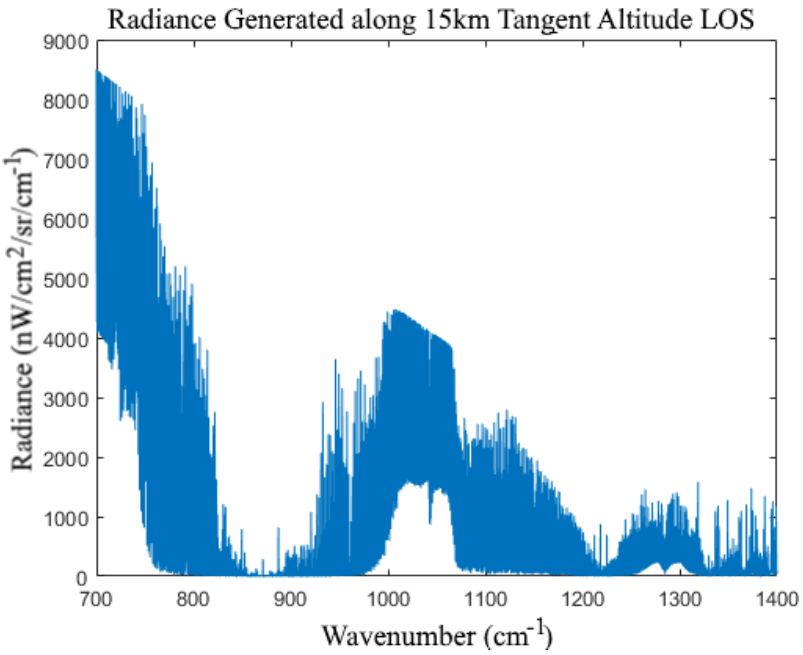


**Figure 5.2:** Radiance generated using the radiative transfer model along a LOS passing through a tangent altitude of 15 km.

### 5.2.1 Interferograms

The radiative transfer model provides a flux value, measured in watts, that is turned by the instrument model into an interferogram in units of volts by the application of equation 3.4. In a true measurement, the detector applies a gain and offset that need to be accounted for, but those factors are not included in this simulation. The raw interferogram as it is measured by the detector, in volts, is shown if figure 5.3.

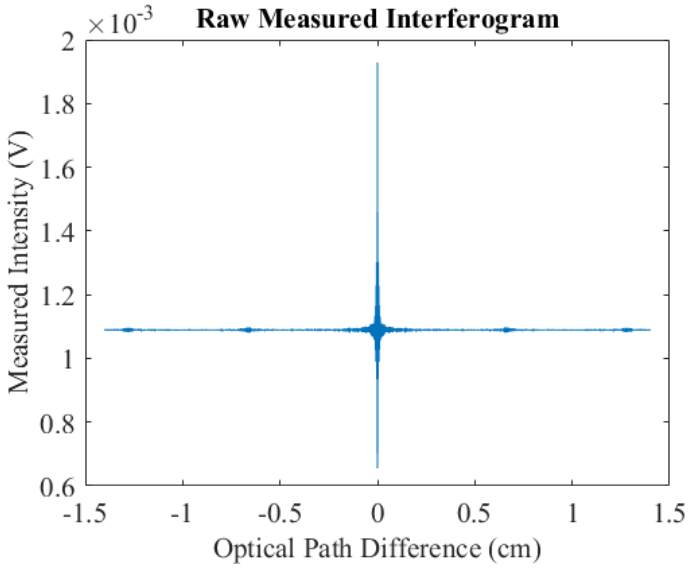


**Figure 5.3:** Raw interferogram measured by the detector, in volts.

Recall that equation 3.4 indicates the interferogram contains both modulated and unmodulated components. To obtain the spectrum used to create the interferogram, a Fourier transform needs to be performed on the modulated component only. As per equation 2.42, the mean of the interferogram is determined and then subtracted, to remove the DC signal component and leave only the modulated portion. Figure 5.4 shows the modulated component obtained after removing the mean from the interferogram depicted in 5.3

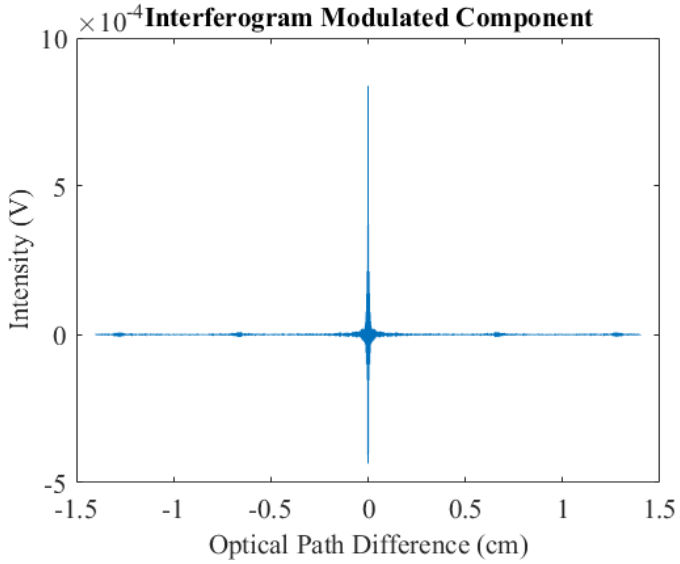


**Figure 5.4:** Modulated component of an interferogram, measured in volts.

The primary noise in the LIFE MCT pixels in detector noise (recall section 4.4.3). Detector "NEP" was measured by the manufacturer to be 42.43 nV/$\sqrt{Hz}$. Taking the frame frequency as 3500 Hz based on the Nyquist criteria and $N = 7840$ samples, the noise is determined by multiplying the square root of frame frequency by the quoted NEP and multiplying by a randomly generated number from a Gaussian distribution. In this way, detector noise is added to the interferogram. This step occurs before the modulated component is found.

### 5.2.2 Spectra

In chapter 2, discussion regarding discontinuity at the interferogram causing side lobes led to apodization as a method of side lobe suppression at cost the of further line broadening. Therefore, apodization is applied. In the current simulation, the Hann function is applied:

$$w(n) = \frac{1}{2}\left(1 - \cos\left(\frac{2\pi n}{N-1}\right)\right) \tag{5.1}$$

Multiplication of the interferogram with this function brings the endpoints smoothly down to zero, as shown in figure 5.5.

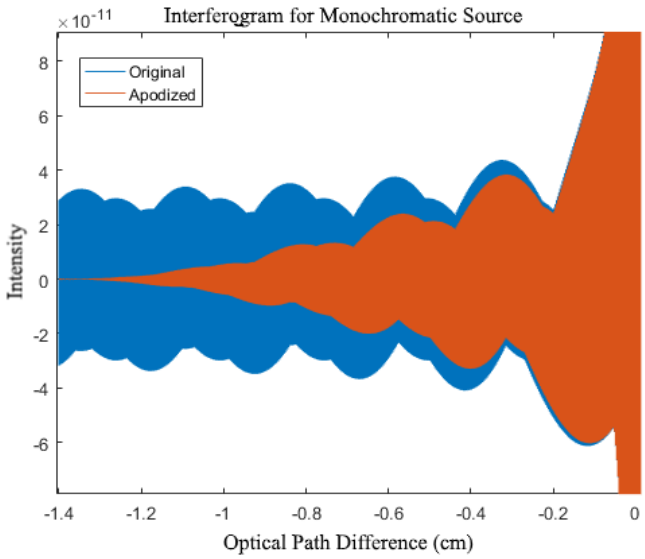


**Figure 5.5:** Zoomed in from negative range to zero, to show the apodization effects at the edge of the interferogram.

Assuming a perfectly monochromatic source, emulated with a Dirac delta function, centered at 1050 cm$^{-1}$, the effect of apodization is demonstrated in figure 5.6.

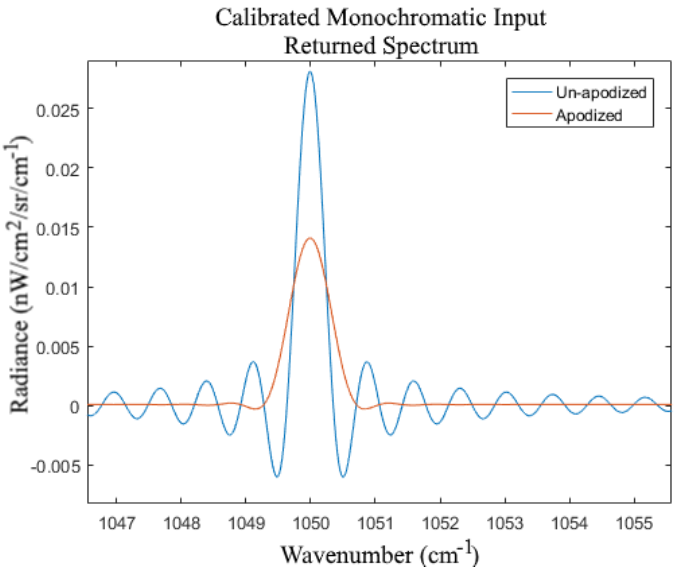


**Figure 5.6:** Comparison of unapodized and apodized result spectrum. Line correction is applied in both cases.

This figure shows that the apodization used causes a reduction in the amplitude of the spectrum returned by the model, as well as broadening the line. However, it also demonstrates that the side lobes have been greatly reduced.

Every apodization function has a different set of parameters and affects the spectrum in unique ways. "Strong" apodization functions like the Hann function mostly remove side lobe effects but also reduce amplitude and broaden the lines the most. The choice of apodization function is strongly related to the quality of data required by the retrieval software. The model is created such that different apodization methods are easily implemented, should future studies reveal that a weaker apodization function is beneficial.

The interferogram containing only the modulated component allows extraction of the spectral information. A Fourier transform is applied to this interferogram; from the discussion of the Nyquist criteria, the result of this FFT gives a double sided spectral result. Taking the first half of the returned data and appropriately determining the spectral spacing using the bin spacing in interferogram space, a representative spectrum is obtained. This spectrum is complex due to the presence of noise and potential phase errors in the calibration.

Figure 5.7 shows the real and imaginary components of the returned spectrum before radiometric calibration occurs.

This figure shows that the presence of noise has introduced imaginary components to the spectrum. This also occurs in the presence of uncalibrated phase errors. In this case, the noise in the signal has caused phase errors, introducing imaginary components. In figure 5.8, the phase of this complex spectrum along with an arbitrary zoom-in on the phase shows that the phase of this spectrum is non-zero over the wavenumber range.

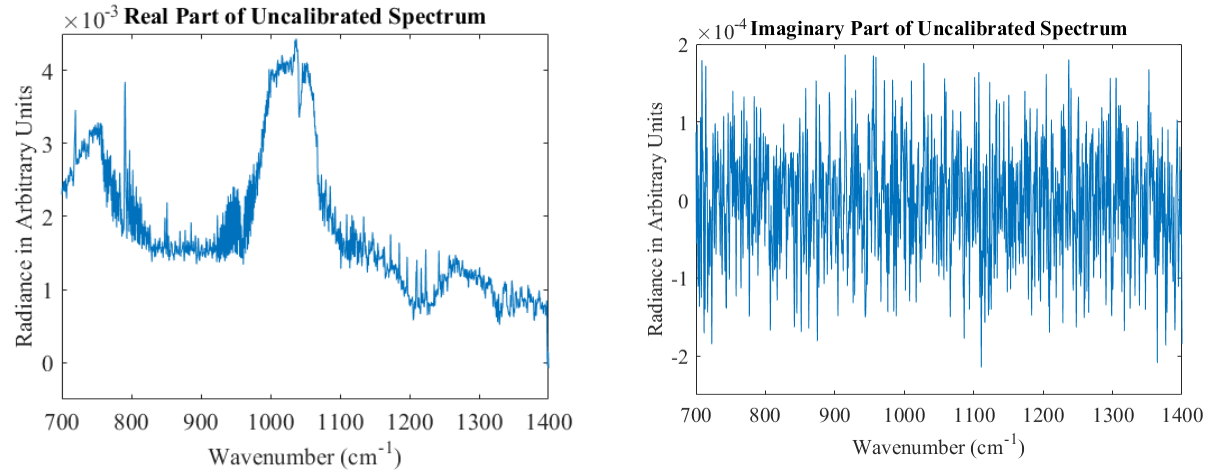


**(a)** Real in AU.

**(b)** Imaginary in AU.

**Figure 5.7:** Real and imaginary components of a complex, uncalibrated spectrum with detector noise added to the interferogram.

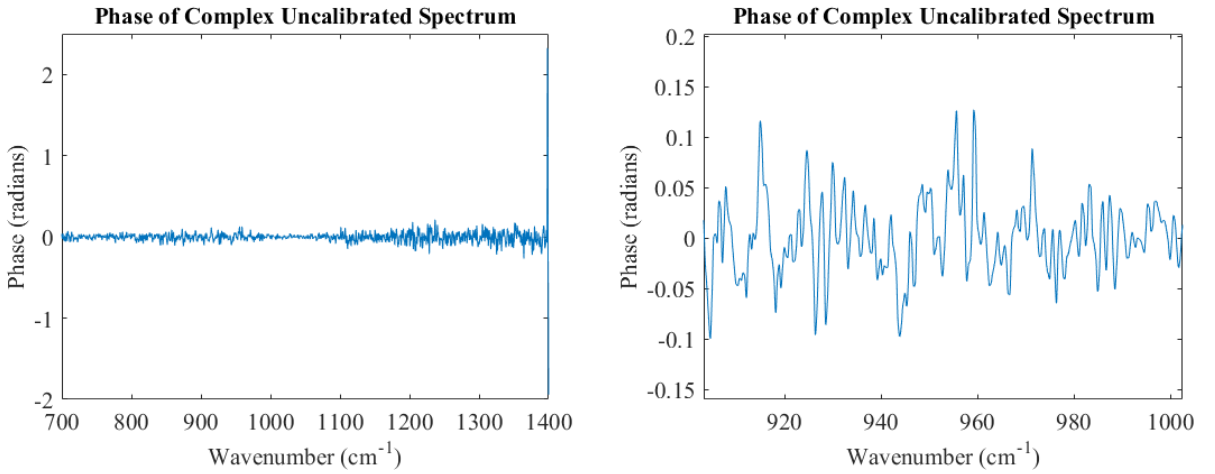


**(a)** Phase for full range.

**(b)** Phase in arbitrary range, to show detail.

**Figure 5.8:** Phase of an uncalibrated, complex spectra obtained from a Fourier transform of an interferogram.

### 5.2.3 Radiometric Calibration

Figure 5.7 shows that both spectral information and noise information appear in both the real and imaginary components of the complex spectrum. To separate the spectral information from the noise, the two-point calibration is applied as per equations 3.9, 3.10 and 3.11.

The application of this calibration requires two blackbody spectra to be input to the model, and have their responses determined. In Figure 5.9, the input and output spectra are summarized, having followed the same process as the true scene.

Using the calibration equations, the gain and offset over the range are calculated, shown in Figure 5.10.

Note the large values at the right edge of the offset term. This is caused by some values after 1398.5 $cm^{-1}$ in the gain term being extremely close to zero at this edge. This causes indeterminate and artificially large values in the calibrated spectrum as a result of dividing by near-zero values. This indicates that usable data recovered by LIFE does not extend all the way to 1400 $cm^{-1}$ and instead terminates around 1398.5 $cm^{-1}$.

Applying the calibration to the spectrum of figure 5.7 leads to calibrated spectra having real and imaginary components as shown in figure 5.11

After the application of the calibration, the real component contains all spectral information, while the imaginary component holds all information related to noise in the measurement. This result is incumbent upon the absence of anomalous phase errors [37]. Figure 5.12 shows that the phase errors still occur in the places where the signal is low. In these areas, noise has a large contribution, or is the sole contribution, leading to larger phase values. In practice, anomalous phase errors will be present, and in-lab measurements are required for a full accounting of potential phase errors in the system. It is from the imaginary component that sensitivity analysis is done, as discussed in section 5.3.

The last step is to apply the wavenumber correction that is known to have been introduced by the optical elements and compare the input and output spectra. This is shown in figure 5.13.

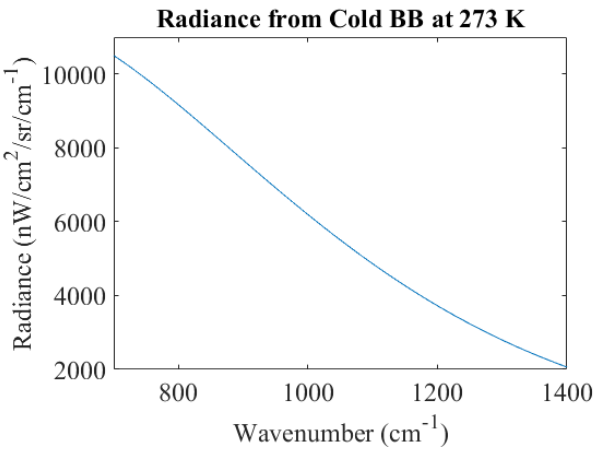


**(a)** Planck function radiance for cold blackbody.

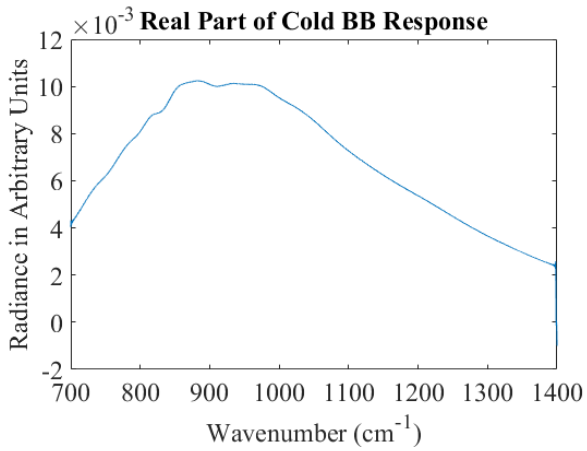


**(b)** Cold BB response real component.

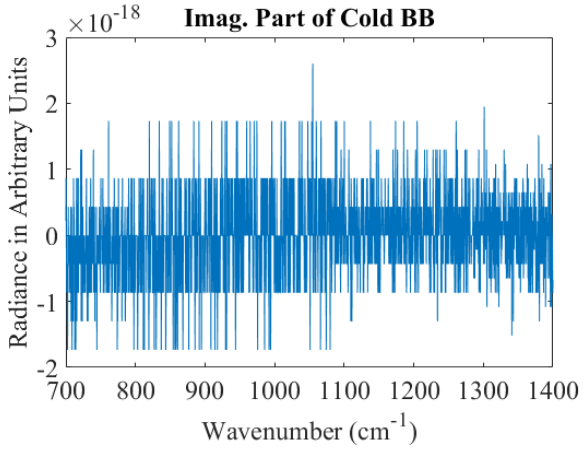


**(c)** Cold BB response imag. component.

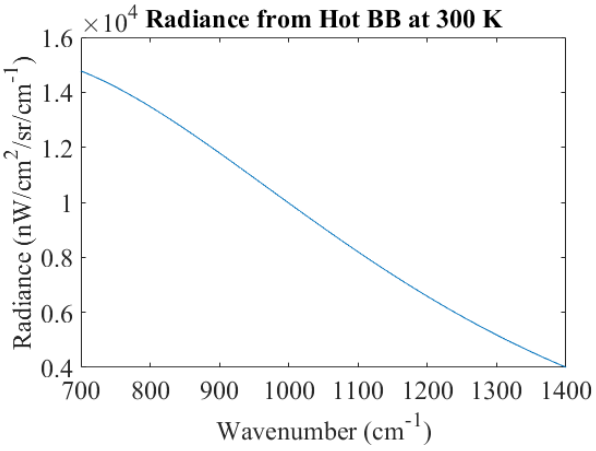


**(d)** Planck function radiance for hot blackbody.

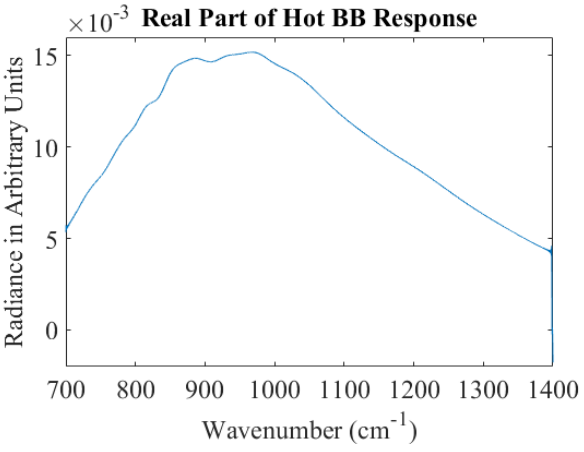


**(e)** Hot BB response real component.

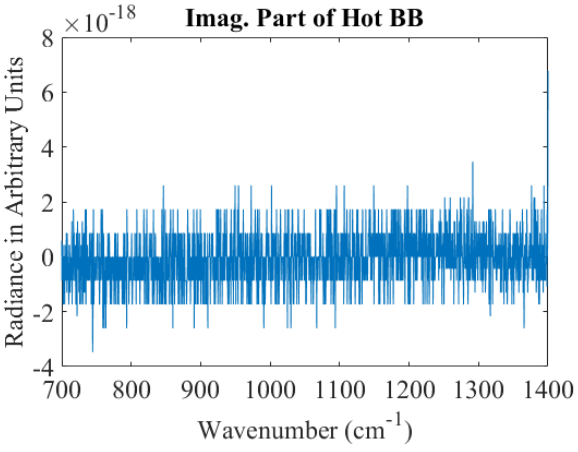


**(f)** Hot BB response imag. component.

**Figure 5.9:** Input and output of the model for blackbody sources.

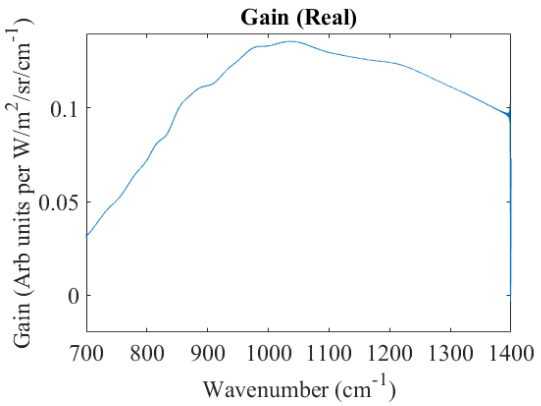


**(a)** Gain in real.

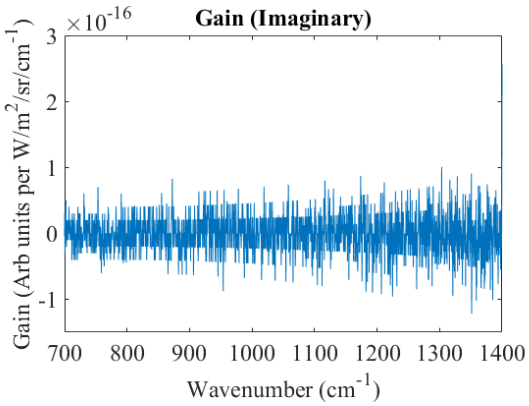


**(b)** Gain in imaginary.

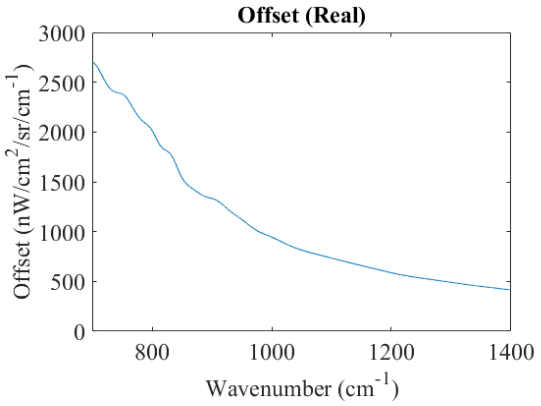


**(c)** Offset in real.

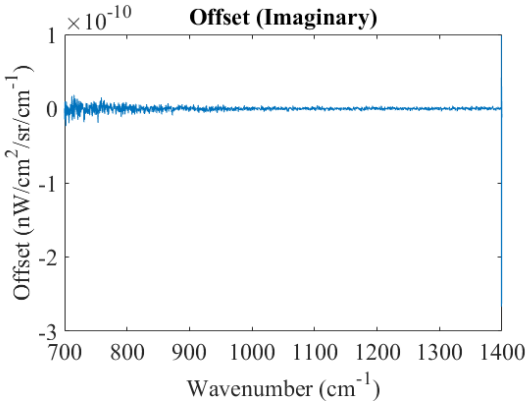


**(d)** Offset in imaginary.

**Figure 5.10:** The gain and offset terms as a function of wavenumber.

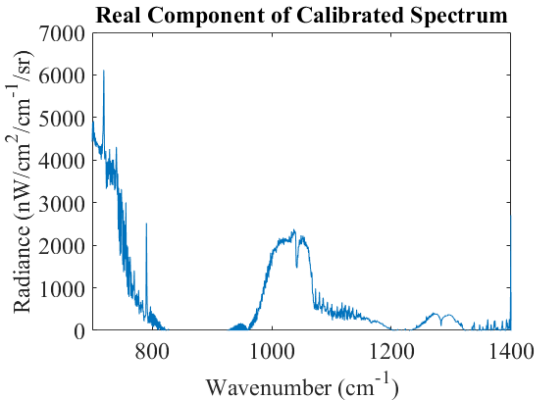


**(a)** Real component of calibrated spectrum.

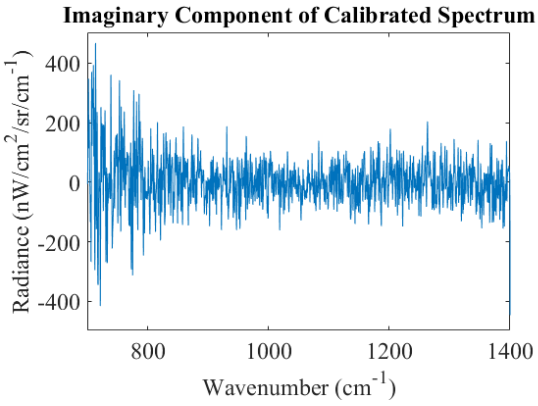


**(b)** Imaginary component of calibrated spectrum.

**Figure 5.11:** Full calibrated spectrum. The real component contains all spectral information and the imaginary component contains all measurement noise.

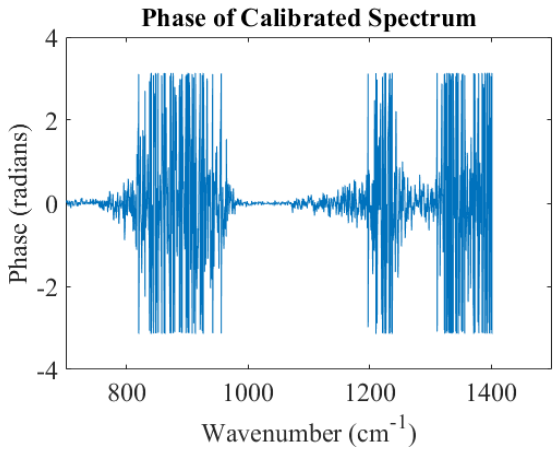


**Figure 5.12:** Phase of the spectrum after application of calibration.

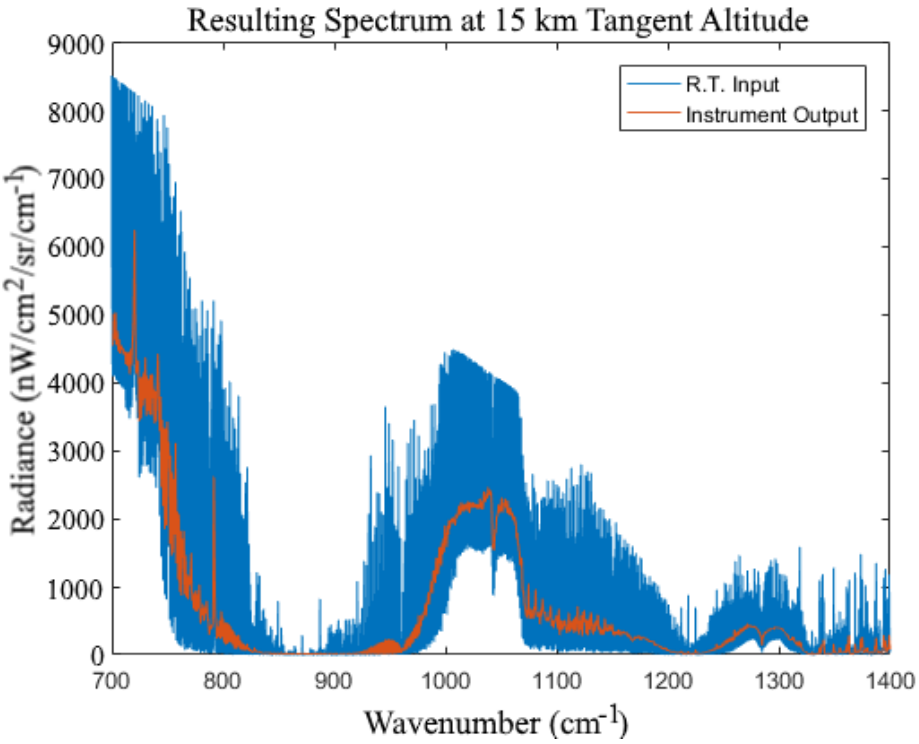


**Figure 5.13:** The radiative transfer model (blue curve) used as an input to the instrument model results in the red curve. The red curve is the full result of the LIFE forward model and represents expected results of LIFE measurements.

Viewing these results over the full range shows that there is good feature agreement between the input and output. Zooming in on the spectrum allows a view of how well the actual line positions match up between the two as well.

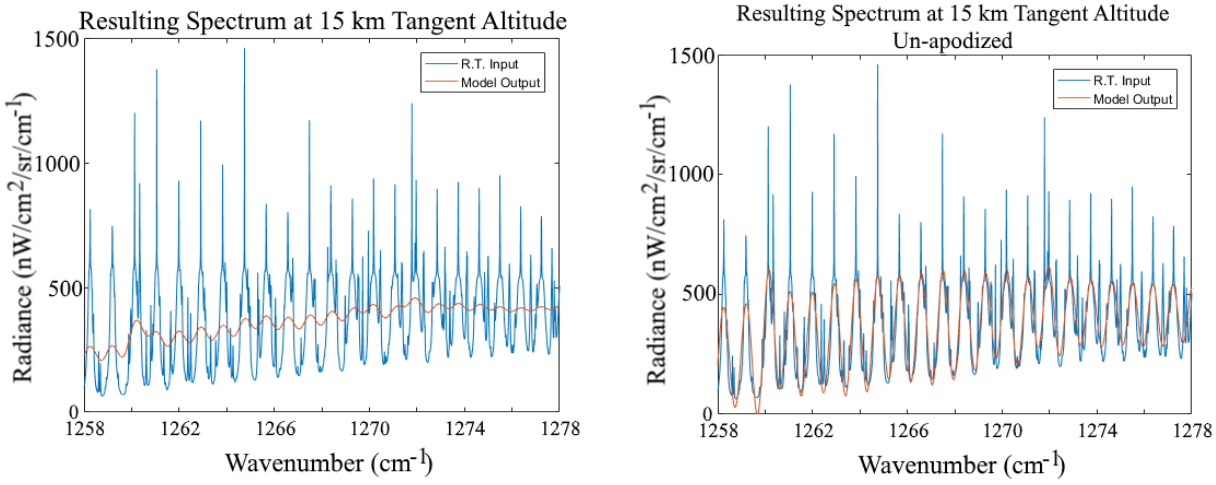


**(a)** Apodization used.

**(b)** No apodization.

**Figure 5.14:** Spectrum of 5.13 zoomed in to show line form.

While figure 5.13 shows broad agreement of spectral features between the two curves, figure 5.14 is somewhat more useful as it shows the relationship of individual lines. These smaller sections of the spectrum are known as microwindows and are typically chosen strategically for retrieval purposes. In figure 5.14, an arbitrary microwindow is selected to show how the expected instrument output correlates to the input for both apodized and unapodized cases.

Examining the visual differences between figure 5.14a and 5.14b, one is tempted to believe that the unapodized case is superior. It must be noted that this is human bias and may lead to complications; recall figure 5.6 which shows the sidelobes of the unapodized case versus the supressed version with apodization. The temptation to use the unapodized case because the spectrum appears to be more correct visually must be resisted; the best way to determine what degree of apodization is appropriate is with rigorous testing using retrieval code.

## 5.3 Sensitivity

Instrument sensitivity is primarily measured by way of the NESR. A simulated NESR is generated by adding randomly varying detector noise as described previously and running

the simulation many times. This type of simulation is called a Monte-Carlo simulation.

After choosing a pixel, the model generates an interferogram based on the scene, with realistic detector noise. The model then performs the calibration and stores the imaginary component as the noise for that simulation. This process is then repeated for a user defined number of times. Once a set number of simulated spectra are created (as specified by the user), the NESR is calculated from the standard deviation of the imaginary components stored from each run. The simulated NESR is expressed as

$$NESR(\sigma) = \sqrt{\frac{\left( n \sum_{i=1}^{n} L_{atm_i}(\sigma)^2 - \left( \sum_{i=1}^{n} L_{atm_i} \right)^2 \right)}{n(n-1)}} \tag{5.2}$$

where $L_{atm_i}$ is the imaginary component of calibrated spectra for each measurement and $n$ is the number of simulated spectra generated. In the following figure, the Monte Carlo simulation is set to run 100 simulations and determine the NESR. The theoretical NESR calculated using instrument parameters and equation 3.17 is also shown.

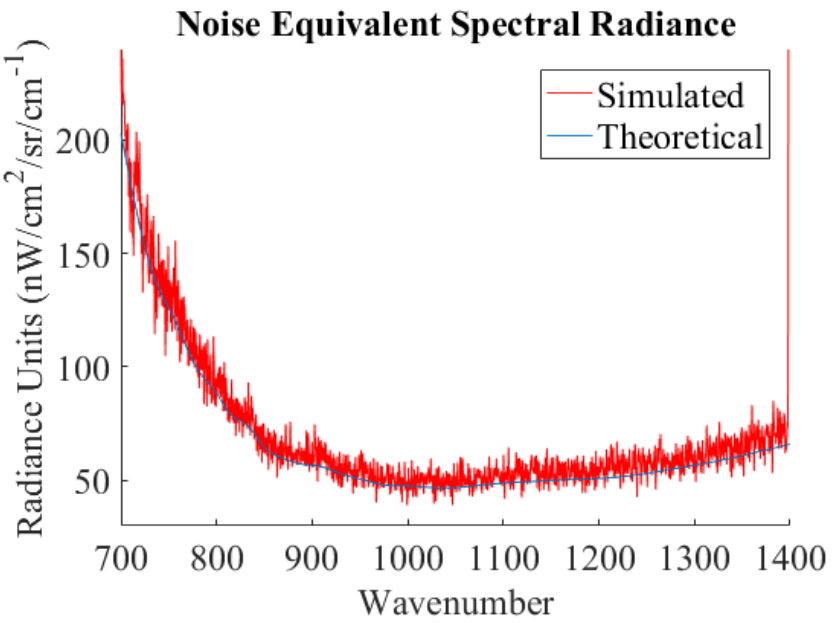


**Figure 5.15:** NESR curves.

There is agreement between the theoretical and simulated NESR values. However, as noted in section 4.2.2, this NESR is higher than the 15 nW/cm$^2$/cm$^{-1}$/sr goal. Theoretically,

averaging 18 scans together reduces the NESR by an appropriate factor. Considering that 18 scans need to be averaged together, a much larger number of noisy interferograms need to be generated. For this next part, 200 interferograms are generated, averaged together in groups of 20, giving 10 distinct scans for NESR determination. Theory states this reduces the observed NESR by a factor of 4.47. Figure 5.16 shows the NESR that occurs as a result of averaging the scans.

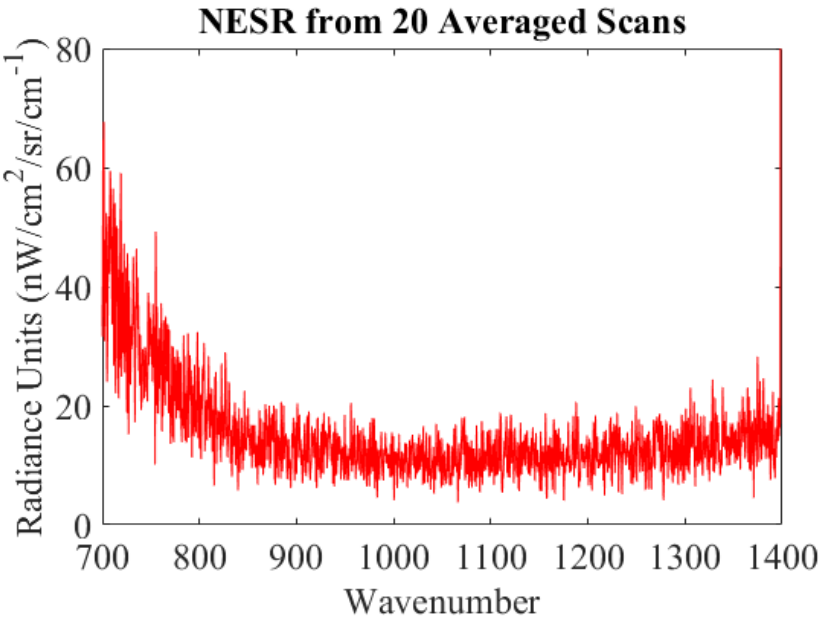


**Figure 5.16:** NESR curve generated by averaging 20 scans together.

The mean of this data set is 15 nW/cm$^2$/cm$^{-1}$/sr, indicating that by averaging together several scans generated by LIFE, the required sensitivity is reached. Recalling that an individual scan takes 2.23 seconds to complete, LIFE must view the same scene for approximately 45 seconds to achieve the science goals. This is feasible from a balloon platform where the instrument will observe the same column of air for several hours.

Another form of sensitivity arises in the non-idealities of the radiometric calibration. As mentioned in section 4.2.2, there is an error in the calibration due to uncertainty in blackbody temperatures. Recalling that the maximum error in blackbody temperature found in lab is 0.5°C [44], the NESR approach is used to determine the sensitivity of measurements to this error. Figure 5.17 shows the NESR curve obtained for this temperature variance.

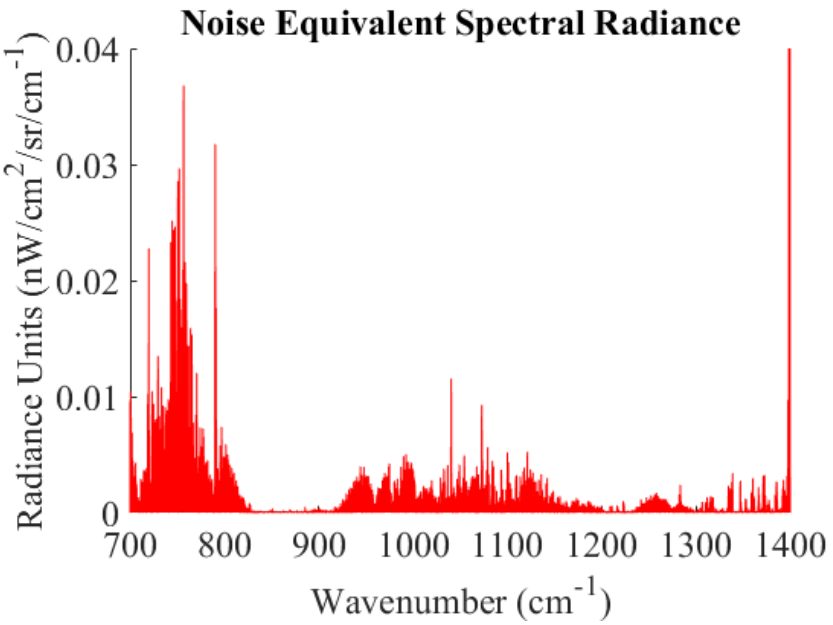


**Figure 5.17:** NESR curve for temperature variance on the order of 0.5°C.

Error generated by this level of uncertainty in blackbody temperatures is minuscule in comparison to the inherent detector error. Noted again are issues at the 1400 $cm^{-1}$ edge, where a division term becomes close to zero and generates unrealistic values. In the areas of interest, this is an indication that the radiometric calibration does not erase important spectral information above levels of 0.04 $nW/cm^2/cm^{-1}/sr$.

# Chapter 6

# Future Work

## 6.1 Overview

In this section, the focus shifts from simulation and theory to the analysis of the types of tests that are required in the future to make LIFE a fully operating system.

The performing of these tests requires the LIFE design decisions of Chapter 4 to be implemented in-lab. This includes taking the detector, interferometer, and designed lens system and creating a lab benchtop design. The proposed set-up, modelled in SolidWorks, is shown in figure 6.1.

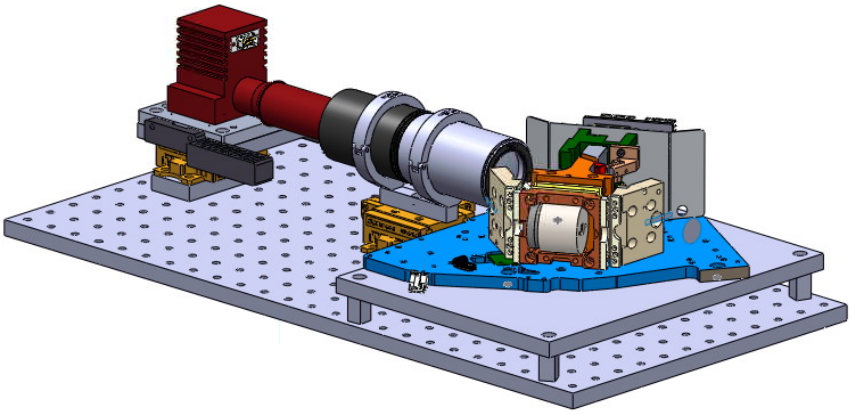

**Figure 6.1:** Solidworks representation of proposed lab set-up.

It is with this set-up that all tests required to ensure LIFE is working as expected are to be done.

At the time of this thesis, LIFE is still in the early stages of design. An instrument that meets scientific objectives has been obtained, as demonstrated by the end-to-end simulations

in Chapter 5, but the characterization of operational parameters and the need for corrections and calibrations are not yet applied. A series of tests and known issues are compiled here, to be performed on the instrument in the future.

## 6.2 Pixel Non-linearity

The radiometric calibration applied as per section 3.1.3 assumes that the response of the detector is linear. However, non-linear effects of photoconductive MCT devices is a well-known issue. Left uncorrected, the calibration leads to radiometric errors in the returned spectra. The extent of non-linearity is based upon the signal levels; low signal levels are more linear than high signal levels. LIFE has large pixels and thus has a large signal level, meaning that non-linearity is an issue that cannot be ignored.

It is possible to correct for non-linear effects with an algorithm, by the determination of correction terms to add to the two-point calibration already in place. The determination of these extra terms requires lab measurements, where a known source is used as an input, and compared to the calibrated output. The differences between the results allows an analysis of additional corrections that can be applied to measurements in general.

## 6.3 Experimental Responsivity and NEP

Discussed in section 3.1.5, the NEP of the system is dependant upon the responsivity of the detectors. The manufacturer of the detector used by LIFE, Infrared Associates, characterized each pixel. ABB provided to the University team these measurements, indicating the NEP and responsivity of each pixel for a specific setting of bias voltage. However, these settings are likely not the same as those used in the operation of LIFE, which means that the NEP and responsivity curve for each pixel needs to be determined experimentally in lab with the proper settings.

A set-up where the NEP and responsivity are determined using a blackbody in the absence of the interferometer is required. This characterization will allow an understanding of how the detector operates and how applied bias and offset parameters affect the observed

response. With this characterization, appropriate settings can be used, and the proper NEP and responsivity values can be added to the model.

## 6.4 Experimental NESR

Determining the NESR experimentally follows the exact same process as the simulation. For each measurement, the imaginary component of calibrated spectra contains the noise. The standard deviation of this component at each wavenumber over hundreds of measurements gives the NESR. This is both measured in lab and monitored during flight.

## 6.5 Instrument Self-emission

Instrument self-emission occurs due to instrument components emitting radiation in the thermal regime. Observation in the thermal regime must therefore deal with the radiation emitted by the parts of the instrument, which add to the spectral signal, and have the potential to mar any measurements. Self-emission can be managed or minimized by choosing optical components with low thermal emissivity, by cooling all components to a low enough temperature that emission is negligible, or by designing a cold stop assembly. LIFE uses the latter technique; however, the residual effects of self-emission must be characterized and understood with in-lab measurements.

### 6.5.1 DC components

The interferometer portion of LIFE is to be operated at room temperature (298 $\pm$ 2 K), whereas the detector is cooled to 77 K with a sterling cooler. Thus, the signal from the interferometer portion of the system has the potential to be large. The cold stop eliminates a large portion of excess signal, and the optical components used are mostly transparent in the target range. Any unmodulated background adds only to the DC component of the signal and is removed by the two-point calibration. While these components should cause no issue, they must still be investigated.

### 6.5.2 Modulated Multiple Reflections

Multiple reflections in the optical system can result in the creation of parasitic images at the detector. Two primary sources of multiple reflections are to be considered for LIFE. The first is reflections from the windows and lenses used in the system, and the second is the result of multiple reflections occurring at the beamsplitter surfaces. The relative phase, location and amplitude of these reflections is important, as they are modulated signals.

LIFE utilizes no fore-optics, and the only surface between the scene and the interferometer is a ZnSe window, with a reflection coefficient <2%. Aft-optics utilize Ge and ZnSe lenses and windows, each with transmission coefficients >0.98. The exit optics are also antireflection coated with coefficients again <2%.

The primary potential source of multiple reflections is the beamsplitter, which has a reflection coefficient of $\sim 0.62$ and a transmission coefficient of $\sim 0.34$. The high reflectance will cause secondary reflections that have the potential of being large. Being present in both arms, these reflections will also be modulated by the interferometer. The beamsplitter tilt determines how the primary reflections are distributed; with the orientation of the interferometer and detector, this means that a reflection of a signal from one tangent altitude could land on a pixel meant to view a different area. If has the potential to catastrophically contaminate the obtained information.

ABB has once again provided patented details about the beamsplitter configuration, under confidential disclosure. This information needs to be used to develop a theoretical model of multiple reflection propagation through the LIFE system. The potential for pixel cross-talk in a given configuration will drive preliminary mechanical design decisions.

## 6.6 Modulation Efficiency

Modulation efficiency is expected to be >0.8 based on ABB specifications, but recall that averaging over the solid angle is expected to reduce this value slightly. A more accurate modulation efficiency term is to be determined experimentally, as the true theoretical form adds time and complexity to the model for comparatively little gain in accuracy.

Using lab measurements of two blackbodies, one hot and one cold, a two-point correction is to be applied to the system. The interferogram created by measuring a blackbody is broken into its modulated and unmodulated components. With both blackbodies, this gives a total of four signals for use in the equation

$$M = \frac{\max(I_{BBHAC}) - \max(I_{BBCAC})}{\text{mean}(I_{BBH}) - \text{mean}(I_{BBC})} \tag{6.1}$$

where the modulated parts of the hot and cold blackbody interferograms are $I_{BBHAC}$ and $I_{BBCAC}$ respectively, and the unmodulated parts of the signal are $I_{BBH}$ and $I_{BBC}$ for hot and cold blackbodies, respectively.

Each pixel will have a separate modulation efficiency that will vary as a function of wavenumber, which must be determined by this set of tests for best results.

## 6.7 Experimental Instrument Line Shape

The theoretical and simulated ILS are discussed in earlier sections but fall prey to assumptions and code optimizations. An examination of the true ILS of LIFE needs to be carried out in lab using well isolated calibration lines.

The proposed test is to use an $N_2O$ gas-cell apparatus and equipment at the University to maintain a constant temperature. With an understanding of the shape of the lines input to the interferometer and the resulting spectrum, a more rigorous and accurate accounting of the system effects on line shape is obtained.

## 6.8 Experimental Line Position

The gas-cell setup also allows a full characterization of the line shifts introduced by the off-axis effects described in section 4.5.3. For each pixel, the known line positions are compared to the positions of the returned spectrum, and an offset determined. This offset can then be applied to correct the line positions of arbitrary spectra.

## 6.9 Uniform Time Sampling

Uniform time sampling is one of the most important issues to correct for in Fourier transform spectrometers. The need for this correction arises from the requirement for extremely accurate position measurements. Recall that an interferogram is made from $N$ measurements, equally spaced at a value $\Delta x$, in the range $[-L, L]$. This is fine in theory, but in practical terms measurements are taken at evenly spaced *time* intervals, $\delta t$. This means that there is no guarantee that measurements taken by the detector have positions separated by $\Delta x$.

If there is a periodic position error such as this that is left uncorrected, the resulting spectrum after taking a Fourier transform is that each line creates "ghosts" to the left and right of the peaks [45]. For this reason, a metrology and synchronisation system needs to be developed that allows the correct determination of data points. Recall from section 4.3 that the requisite signals are generated by the FTS system obtained from ABB, leaving a method of capturing and analyzing the signals and applying UTS methods to the University team.

## 6.10 Conclusion

The goal of the LIFE project was to design a prototype IFTS instrument with high spatial and temporal resolution for a balloon flight. A model was developed allowing the simulation of an IFTS and an analysis of overall instrument performance. An instrument capable of meeting the science goals is designed and an in-lab version is to be created and characterized.

The application of these characterizations and tests to the lab instrument will allow the creation of a flight capable device. The physical realization of the theoretical device designed and analyzed in this thesis is intended to be complete and flown on a balloon platform in 2019. In conjunction with the model developed herein, data recovered from the 2019 flight will inform further refining of the design for the eventual creation of a satellite version of LIFE.

The LIFE project thus completes the primary objective of developing a prototype and foundation upon which further IFTS research and development at the University of Saskatchewan can expand.

# References


[1] Clive D. Rodgers. *Inverse Methods for Atmospheric Sounding Theory and Practice*. World Scientific Publishing, 2000.

[2] P. Jaquinot. New developments in interference spectroscopy. *Reports on Progress in Physics*, 23:267–312, 1960.

[3] Akihiko Kaze, Hiroshi Suto, Masakatsu Nakajima, and Takashi Hamazaki. Thermal and near infrared sensor for carbon observation fourier-transform spectrometer on the greenhouse gases observing satellite for greenhouse gases monitoring. *Applied Optics*, 48:6716–6733, 2009.

[4] Peter Bernath. The atmospheric chemistry experiment (ace): An overview. In *IEEE International Geoscience and Remote Sensing Symposium*. 2002.

[5] H. Fischer, M. Birk, C. Blom, B. Carli, M. Carlotti, T. von Clarmann, L. Dlbouille, A. Dudhia, D. Ehhalt, M. Endemann, J. M. Flaud, R. Gessner, A. Kleinart, R. Koopman, J. Langren, M. Lopez-Puertas, P. Mosner, H. Nett, H. Oelhaf, G. Perron, J. Remedios, M. Ridolfi, G. Stiller, and R. Zander. Mipas: an instrument for atmospheric and climate research. *Atmospheric Chemistry and Physics*, 8:2151–2188, 2008.

[6] F. Friedl-Vallon, G. Maucher, M. Seefeldner, O. Trieschmann, A. Kleinert, A. Lengel, C. Keim, H. Oelhaf, and H. Fischer. Design and characterization of the balloon-borne michelson interferometer for passive atmsopheric sounding (mipas-b2). *Applied Optics*, 43:3335–3355, 2004.

[7] H. Fischer and H. Oelhaf. Remote sensing of vertical profiles of atmospheric trace constituents with mipas limb-emission spectrometers. *Applied Optics*, 35:2787–2796, 1996.

[8] T. von Clarmann, M. Hopfner, S. Kellmann, A. Linden, S. Chauhan, B. Funke, U. Grabowski, N. Glatthor, M. Kiefer, T. Schieferdecker, G.P. Stiller, and S. Versick. Retrieval of temperature, $h_2o$, $o_3$, $hno_3$, $ch_4$, $n_2o$, $clono_2$ and clo from mipas reduced resolution nominal mode limb emission measurements. *Atmospheric Measurement Techniques*, 2:159–175, 2009.

[9] A. Wiegele, A. Kleinert, H. Oelhaf, R. Ruhnke, G. Wetzel, F. Friedl-Vallon, A. Lengel, G. Maucher, H. Nordmeyer, and H. Fischer. Spatio-temporal variations of noy species in the northern latitudes stratosphere measured with the balloon-borne mipas instrument. *Atmopsheric Chemistry and Physics*, 9:1151–1163, 2009.

[10] W.A. Lahoz, A.J. Geer, and Y.J. Orsolini. Northern hemisphere stratospheric summer from mipas observations. *Quarterly Journal of the Royal Meteorological Society*, 133:197–211, 2007.

[11] L. Hoffmann, R. Spang, M. Kaufmann, and M. Riese. Retrieval of cfc-11 and cfc-12 from envisat mipas observations by means of rapid radiative transfer calculations. *Advances in Space Research*, 36:915–921, 2005.

[12] S. Griessbach, L. Hoffmann, R. Spang, and M. Riese. Volcanic ash detection with infrared limb sounding: Mipas observations and radiative transfer simulations. *Atmospheric Measurement Techniques*, 7:1487–1507, 2014.

[13] Mahesh Kumar Sha. *Characterization and Optimization of the new Imaging Fourier Transform Spectrometer GLORIA*. PhD thesis, 2013.

[14] M. Riese, H. Oelhaf, P. Preusse, J. Blank, M. Ern, F. Friedl-Vallon, H. Fischer, T. Guggenmoser, M. Hopfner, P. Hoor, M. Kaufmann, J. Orphal, F. Ploger, R. Spang, O. Suminska-Ebersoldt, J. Ungermann, B. Vogel, and W. Woiwode. Gimballed limb obseerver for radiance imaging og the atmosphere (gloria) scientific objectives. *Atmospheric Measurement Techniques*, 7:1915–1928, 2014.

[15] A. Kleinert, F. Friedl-Vallon, T. Guggenmoser, M. Hopfner, T. Neubert, R. Ribalda, M. K. Sha, J. Ungermann, J. Blank, A. Ebersoldt, E. Kretschmer, T. Latzko, H. Oelhaf, F. Olschewski, and P. Preusse. Level 0 to 1 processing og the imaging fourier transform spectrometer gloria: generation of radiometrically and spectrally calibrated spectra. *Atmospheric Measurement Techniques*, 7:4167–4184, 2014.

[16] F. Olschewski, A. Ebersoldt, F. Friedl-Vallon, B. Gutschwager, J. Hollandt, A. Kleinert, C. Monte, C. Piesch, P. Preusse, C. Rolf, P. Steffens, and R. Koppmann. The in-flight blackbody calibrationsystem for the gloria interferometer on board an airbrone research platform. *Atmospheric Measurement Techniques*, 6:3067–3082, 2013.

[17] F. Friedl-Vallon, T. Gulde, F. Hase, A. Kleinert, T. Kulessa, G. Maucher, T. Neubert, F. Olschewski, C. Piesch, P. Preusse, H. Rongen, C. Sartorius, H. Schneider, A. Schonfeld, V. Tan, N. Bayer, J. Blank, R. Dapp, A Ebersoldt, H. Fischer, F. Graf, T. Guggenmoser, M. Hopfner, M. Kaufmann, E. Kretschmer, T. Latzko, H. Nordmeyer, H. Oelhaf, J. Orphal, M. Riese, G. Schardt, J. Schillings, M. K. Sha, O. Suminska-Ebersoldt, and J. Ungermann. Instrument concept of the imaging fourier transform spectrometer gloria. *Atmospheric Measurement Techniques*, 7:3565–3577, 2014.

[18] C. Monte, B. Gutschwager, A. Adibekyan, M. Kehrt, A. Ebersoldt, F. Olschewski, and J. Hollandt. Radiometric calibration of the in-flight blackbody calibration system of the gloria interferometer. *Atmopsheric Measurement Techniques*, 7:13–27, 2014.

[19] M. Kaufmann, J. Blank, T. Guggenmoser, J. Ungermann, A. Engel, M. Ern, F. Friedl-Vallon, D. Gerber, J. U. Groob, G. Guenther, M. Hopfner, A. Kleinert, E. Kretschmer,

T. Latzko, G. Maucher, T. Nuebert, H. Nordmeyer, H. Oelhaf, F. Olschewski, J. Orphal, P. Preusse, H. Schlager, H. Schneider, D. Schuettemeyer, F. Stroh, O. Suminska-Ebersoldt, B. Vogel, C. M. Volk, W. Woiwode, and M. Rise. Retrieval of three-dimensional small-scale structures in upper-tropospheric/lower-stratospheric composition as measured by gloria. *Atmospheric Measurement Techniques*, 8:81–95, 2015.

[20] C. Piesch, C. Sartorius, F. Friedl-Vallon, T. Gulde, S. Heger, E. Kretschmer, G. Maucher, H. Nordmeyer, J. Barthel, A. Bersoldt, F. Graf, F. Hase, A. Kleinert, T. Neubert, and H. J. Schillings. The mechanical and thermal setup of the gloria spectrometer. *Atmospheric Measurement Techniques*, 8:1773–1787, 2015.

[21] J. Ungermann, J. Blank, M. Dick, A. Ebersoldt, F. Friedl-Vallon, A. Giez, T. Guggenmoser, M. Hopfner, T. Jurkat, M. Kaufmann, A. Kleinert, M. Kramer, T. Latzko, H. Oelhaf, F. Olschewski, P. Preusse, C. Rolf, J. Schillings, O. Suminska-Ebersoldt, V. Tan, N. Thomas, C. Voigt, A. Zahn, M. Zoger, and M. Riese. Level 2 processing for the imaging fourier transform spectrometer gloria: derivation and validation of temperature and trace gas volume mixing ratios from calibrated dynamics mode spectra. *Atmospheric Measurement Techniques*, 8:2473–2489, 2015.

[22] Canadian Space Agency. Flights and fieldwork for the advancement of science and technology (fast 2015) announcement of opportunity. Available at `http://www.asc-csa.gc.ca/eng/ao/2015-fast.asp`(2017/07/13).

[23] A. Gettelman, P. Hoor, L.L. Pan, W.J. Randel, M.I. Hegglin, and T. Birner. The extratropical upper troposphere and lower stratosphere. *Reviews of Geophysics*, 49:RG3003, 2011.

[24] Murray Salby. *Physics of the Atmosphere and Climate*. Cambridge University Press, 2012.

[25] Doug Degenstein, Adam Bourassa, and Kaley Walker. Prototype Development of the Limb Imaging FTS Experiment (LIFE) for a Stratospheric Balloon. Technical report, 2015.

[26] S. Chapman. On ozone and atomic oxygen in the upper atmosphere. *Philosophical Magazine*, 10:369–383, 1930.

[27] J. Kiehl and K. E. Trenberth. Earth's annual global mean energy budget. *American Meteorogical Society*, 78:197–208, 1997.

[28] P. Forster, V. Ramaswarmy, P. Artaxo, T. Berntsen, R. Betts, D.W. Fahey, J. Haywood, J. Lean, D.C. Lowe, G. Myhre, J. Nganga, R. Prinn, G. Raga, M. Schulz, and R. Van Dorland. Changes in atmospheric constituents and in radiative forcing. In S. Solomon, D. Qin, M. Manning, Z. Chen, M. Marquis, K.B. Averyt, M. Tignor, and H.L. Miller, editors, *Climate Change 2007: The Physical Science Basis. Contribution of Working Group I to the Fourth Assessment Report of the Intergovernmental Panel on Climate Change*. Cambridge University Press, Cambridge, United Kingdom and New York, NY, USA, 2007.

[29] Susan Solomon, Karen H. Rosenlof, Robert W. Portmann, John S. Daniel, Sean M. Davis, Todd J. Sanford, and Gian-Kasper Plattner. Contributions of stratospheric water vapor to decadal changes in the rate of global warming. *Science*, 327:1219–1223, 2010.

[30] Sumner P. Davis, Mark C. Abrams, and James W. Brault. *Fourier Transform Spectrometry*. Academic Press, San Diego, California, 2001.

[31] A. A. Michelson and F. G. Pease. Measurement of the diameter of alpha-orionis by the interferometer. *Proceedings of the National Academy of Sciences of the United States of America*, 7:143–146, 1921.

[32] D. R. Hearn. Fourier transform interferometry. Technical report, 1999.

[33] S.C. Shen. Comparison and competition between mct and qw structure material for use in ir detectors. *Microelectronics Journal*, 25:713–739, 1994.

[34] A. D. D. Dwivedi and P. Chakrabarti. Modeling and analysis of photoconductive detectors based on $hg_{1-x}cd_xte$ for free space optical communication. *Optical and Quantum Electronics*, 39:627–641, 2007.

[35] A. Rogalski and J. Piotrowski. Intrinsic infrared detectors. *Progress in Quantum Electronics*, 12:87–289, 1988.

[36] Anne Kleinert and Olaf Trieschmann. Phase determination for a fourier transform infrared spectrometer in emission mode. *Applied Optics*, 46:2307–2319, 2007.

[37] H. E. Revercomb, H. Buijs, H. B. Howell, D. D. LaPorte, W. L. Smith, and L. A. Sromovsky. Radiometric calibration of ir fourier transform spectrometers: solution to a problem with the high-resolution interferometer sounder. *Applied Optics*, 27(15):3210–3218, 1988.

[38] Lawrence Sromovsky. Radiometric errors in complex fourier transform spectrometry. *Applied Optics*, 42:1779–1787, 2003.

[39] Jean-Marc Theriault. Fourier-transform spectrometer configuration optimized for self emission suppression and simplified radiometric calibration, 2001.

[40] Henry L. Buijs. Beamsplitter configuration for optical subtraction of self emission with fourier transform spectrometer in dual input port mode, 2012.

[41] ABB Inc. Life core interface control document. Technical report, 2018.

[42] Eugene Hecht. *Optics*. Addison Wesley Longman, Inc, 4 edition, 2002.

[43] BMV Optical Technologies. Bmv internal job no. 7619. Technical report, 2018.

[44] R Bouchard and F. Aube. Mop-a mopitt airborne calibration source subsystem calibration and test report. Technical report, 1999.

[45] James W. Brault. New approach to high-precision fourier transform spectrometer design. *Applied Optics*, 35(16):2891–2896, 1996.